

**Horizon 2020**

Space Call - Earth Observation: EO-3-2016: Evolution of Copernicus services  
Grant Agreement No. 730008

# ECoLaSS

## Evolution of Copernicus Land Services based on Sentinel data



### D6.2

#### “D31.1b - Methods Compendium: S-1/2/3 Integration Strategies”

Issue/Rev.: 2.0

Date Issued: 29.12.2019

submitted by:



in collaboration with the consortium partners:



submitted to:



European Commission – Research Executive Agency

This project has received funding from the European Union’s Horizon 2020 Research and Innovation Programme, under Grant Agreement No. 730008.

## CONSORTIUM PARTNERS

No.	PARTICIPANT ORGANISATION NAME	SHORT NAME	CITY, COUNTRY
1	GAF AG	GAF	Munich, Germany
2	Systèmes d'Information à Référence Spatiale SAS	SIRS	Villeneuve d'Ascq, France
3	JOANNEUM RESEARCH Forschungsgesellschaft mbH	JR	Graz, Austria
4	Université catholique de Louvain, Earth and Life Institute (ELI)	UCL	Louvain-la-Neuve, Belgium
5	German Aerospace Center (DLR), German Remote Sensing Data Center (DFD), Wessling	DLR	Wessling, Germany

### CONTACT:

GAF AG  
Arnulfstr. 199 – D-80634 München – Germany  
Phone: ++49 (0)89 121528 0 – FAX: ++49 (0)89 121528 79  
E-mail: [copernicus@gaf.de](mailto:copernicus@gaf.de) – Internet: [www.gaf.de](http://www.gaf.de)

### DISCLAIMER:

The contents of this document are the copyright of GAF AG and Partners. It is released by GAF AG on the condition that it will not be copied in whole, in section or otherwise reproduced (whether by photographic, reprographic or any other method) and that the contents thereof shall not be divulged to any other person other than of the addressed (save to the other authorised officers of their organisation having a need to know such contents, for the purpose of which disclosure is made by GAF AG) without prior consent of GAF AG. Nevertheless, single or common copyrights of the contributing partners remain unconditionally unaffected.

### DOCUMENT RELEASE SHEET

	NAME, FUNCTION	DATE	SIGNATURE
Author(s):	Annekatriin Metz-Marconcini (DLR) Igor Klein (DLR) Soner Üreyen (DLR) Benjamin Leutner (DLR) Inès Moreau (UCL) Sophie Villerot (SIRS) Grégory Jacquet (SIRS) Petra Miletich (JR)	29.12.2019	
Review:	Benjamin Leutner (DLR) Baudouin Desclee (SIRS) Katharina Schwab (GAF)	29.12.2019	
Approval:	Eva Sevillano Marco (GAF)	29.12.2019	
Acceptance:	Massimo Ciscato (REA)		
Distribution:	Public		

### DISSEMINATION LEVEL

DISSEMINATION LEVEL		
PU	Public	X
CO	Confidential: only for members of the consortium (including the Commission Services)	

### DOCUMENT STATUS SHEET

ISSUE/REV	DATE	PAGE(S)	DESCRIPTION / CHANGES
1.0	22.03.2018	71	First issue of the Methods Compendium: S-1/2/3 Integration Strategies
2.0	29.12.2019	80	Second issue of the Methods Compendium: S-1/2/3 Integration Strategies. Major additions include a summary report on Proba-V fusion testing and Section 5: Data and methods used for ECoLaSS prototype production.

### APPLICABLE DOCUMENTS

ID	DOCUMENT NAME / ISSUE DATE
AD01	Horizon 2020 Work Programme 2016 – 2017, 5 iii. Leadership in Enabling and Industrial Technologies – Space. Call: EO-3-2016: Evolution of Copernicus services. Issued: 13.10.2015
AD02	Guidance Document: Research Needs Of Copernicus Operational Services. Final Version issued: 30.10.2015
AD03	Proposal: Evolution of Copernicus Land Services based on Sentinel data. Proposal acronym: ECoLaSS, Proposal number: 730008. Submitted: 03.03.2016
AD04	Grant Agreement – ECoLaSS. Grant Agreement number: 730008 – ECoLaSS – H2020-EO-2016/H2020-EO-2016, Issued: 18.10.2016
AD05	D6.1: D31.1a - Methods Compendium: S-1/2/3 Integration Strategies, (Issue 1), Issued: 26.03.2018
AD06	Technical Note: Proposed substitutes for S-3 data. Issued: 04.12.2018.
AD07	D7.2: D32.1b- Methods Compendium: Time Series Preparation, (Issue 2), Issued: 15.05.2019
AD08	D8.2: D33.1b - Methods Compendium: Time Series Analysis for Thematic Classification (Issue 2), Issued: 18.12.2019
AD09	D9.2: D34.1b - Methods Compendium: Time Series Analysis for Change Detection (Issue 2), Issued: 04.12.2019
AD10	D10.2: D35.1b - Methods Compendium: Time Series Consistency for HRL Product (Incremental) Updates (Issue 2), Issued: 09.12.2019
AD11	D11.2: D41.1b – Prototype Report: Time Series Analysis for Change Detection Issued: 24.12.2019
AD12	D12.2: D42.1b – Prototype Report: Consistent HR Layer Timer Series / Incremental Updates, Issued: 03.12.2019
AD13	D13.2: D43.1b – Prototype Report: Improved Permanent Grassland, Issued: 05.12.2019
AD14	D14.2: D44.1b Prototype Report: Crop Area and Crop Status / Parameters, Issued: 20.12.2019
AD15	D15.2: D45.1b- Prototype Report: New LC/LU Products, Issued: 28.12.2019
AD16	D1.5: D11.3b – Interim Progress Report (Issue 2), Issued: 09.07.2019
AD17	D4.2: D22.1b - EO and other Data Requirements Report (Issue 2), Issued: 21.02.2019

## EXECUTIVE SUMMARY

The Horizon 2020 (H2020) project, “Evolution of Copernicus Land Services based on Sentinel data” (ECoLaSS) addresses the H2020 Work Programme 5 iii. Leadership in Enabling and Industrial technologies - Space, specifically the Topic EO-3-2016: Evolution of Copernicus services. ECoLaSS was conducted from 2017 to 2019 and aimed at developing and prototypically demonstrating selected innovative products and methods for next-generation operational Copernicus Land Monitoring Service (CLMS) products of the pan-European and Global Components. This will contribute to demonstrating operational readiness of the finally selected products, and shall allow the key CLMS stakeholders (i.e. mainly the Entrusted European Entities (EEE) EEA and JRC) to take informed decisions on potential procurement of the next generation of Copernicus Land services from 2020 onwards. To achieve this goal, ECoLaSS makes full use of dense time series of S-2 and S-3 optical data as well as S-1 Synthetic Aperture Radar (SAR) data. Rapidly evolving scientific as well as user requirements were analysed in support of a future pan-European roll-out of new/improved CLMS products, and the transfer to global applications.

This report constitutes a methods compendium of potential S-1/-2/-3 (S-1/-2/-3) integration strategies aiming at developing and testing integration strategies for S-1, S-2 and coarse resolution optical data to allow benefitting from their complementary multi-resolution, multi-temporal and multi-sensor characteristics. Given the delayed readiness of S-3 data [AD06], this report explores the experiences made with PROBA-V as an alternative coarse resolution sensor.

The objective of WP 31 is to investigate the possibilities of combining S-1, S-2 and other coarse resolution optical data (aimed at S3 data, but tested with PROBA-V data) with regards to the envisaged evolution of Copernicus Land Services addressed in ECoLaSS. Within this WP, a feasibility analysis for a better characterisation of the HRLs by means of two types of integration/fusion strategies is pursued: the integration of S-1 and S-2 data as well as the fusion of S-2 and PROBA-V data. With the combination of S-1 and S-2 data, the integration of complementary information is established, resulting from different physical interactions with the land surface, describing primarily different characteristics of the Land Cover/Land Use. With a fusion/integration of time series data from S-2 and PROBA-V corresponding sets of spectral bands are analysed, sensible for the same biophysical properties with partially overlapping spectral bands in the visible and NIR spectral regions of both sensors, but lower spatial resolution. The additional data-takes and denser time series derived from coarse resolution sensors such as S-3 and PROBA-V offer high potential generating a fusion product of both satellite sensors using interpolation methods.

The ECoLaSS project followed a two-phased approach of two times 18 months duration. This deliverable comprises the second issue report. The first issue “D6.11 - D31.1 Methods Compendium: S-1/2/3 Integration Strategies” primarily focused on identifying suitable approaches for the integration of S-1/-2/-3. Therefore, current state-of-the-art methods have been investigated to define fusion approaches integrating data with different spectral and/or spatial resolutions from two or more sensors in order to exploit both their high spectral and temporal resolution properties and to target the challenges of missing data in a time series. Furthermore, candidate approaches for a fusion/integration of S-1/S-2 and S-2/S-3 have been identified and benchmarked. This second issue of the report expands into a high-level summary of the methods and the remote sensing data requirements posed for HRL production and identified in the different ECoLaSS application domains in all other Tier 3 (WP32-WP35) and Tier 4 (WP41-WP45) work packages. Following the reviewer recommendation, benchmarking and practical testing initiated in issue 1 has therefore been moved out of WP31 and was carried out and reported in WPs 32-35 [AD07-AD10]. Nevertheless, this report also contributes some additional phase II tests of a data fusion approach with S-2 and PROBA-V, since the S-2 / S-3 time-series fusion, while promising, was not operationally ready [AD06] and therefore not part of any other prototype testing and production.

## Table of Contents

<b>1</b>	<b>INTRODUCTION .....</b>	<b>1</b>
1.1	PURPOSE AND OBJECTIVES .....	1
1.2	OUTLINE.....	2
<b>2</b>	<b>MULTI-SENSORAL REMOTE SENSING FOR LC/LU ANALYSIS.....</b>	<b>3</b>
2.1	OPTICAL TIME SERIES DATA AND ITS LIMITATIONS.....	3
2.2	SAR TIME SERIES DATA AND ITS LIMITATIONS .....	3
2.3	ADVANTAGES OF THE INTEGRATION OF OPTICAL AND SAR IMAGERY .....	4
2.4	ADVANTAGES OF SPATIAL - TEMPORAL FUSION OF OPTICAL IMAGERY .....	4
<b>3</b>	<b>STATE-OF-THE ART.....</b>	<b>5</b>
3.1	PRE-PROCESSING STEPS ENABLING COMPLEMENTARY INFORMATION INTEGRATION AND FUSION.....	6
3.2	INTEGRATION OF S-1/S-2 COMPLEMENTARY INFORMATION.....	6
3.2.1	SAR data as complementary information to S-2 .....	6
3.2.2	Conclusions.....	12
3.3	INTEGRATION OF S-2/S-3 (FUSION) .....	12
3.3.1	Spectral, spatial, temporal interpolation and/or fusion approaches .....	12
3.3.2	Candidate variables for time-series fusion .....	19
3.4	CANDIDATE INTERPOLATION AND FUSION APPROACHES FOR BENCHMARKING .....	36
3.4.1	Candidate approaches for integration of S-1/S-2 complementary information .....	36
3.4.2	Candidate approaches for spectral, spatial, temporal interpolation and/or fusion approaches .....	36
3.4.3	Candidate approaches for spectral time series metrics/variables .....	37
<b>4</b>	<b>TESTING AND BENCHMARKING OF CANDIDATE METHODS.....</b>	<b>39</b>
4.1	DESCRIPTION OF CANDIDATE METHODS.....	39
4.1.1	Candidate approaches for integration of S-1/S-2 complementary information .....	39
4.1.2	Candidate approaches for spectral, spatial, temporal interpolation and/or fusion approaches .....	40
4.1.3	Candidate approaches for spectral time series metrics/variables .....	41
4.2	TESTING CRITERIA.....	43

4.3	IMPLEMENTATION OF TESTING .....	44
4.3.1	Candidate approaches for integration of S-1/S-2 complementary information .....	44
4.3.2	Candidate approaches for spectral time series metrics/variables .....	47
4.3.3	Candidate approaches for spectral, spatial, temporal interpolation and/or fusion approaches .....	58
<b>5</b>	<b>DATA REQUIREMENTS AND METHODS USED BY ECOLASS APPLICATION DOMAIN .....</b>	<b>60</b>
5.1	WP41 TIME-SERIES DERIVED INDICATORS & VARIABLES .....	60
5.1.1	Generic Land Cover Metrics .....	61
5.1.2	Potential Change Indicators.....	61
5.2	WP42 INCREMENTAL UPDATES OF HR LAYERS.....	61
5.2.1	Imperviousness.....	62
5.2.2	Forest.....	63
5.3	WP 43 IMPROVED PERMANENT GRASSLAND IDENTIFICATION .....	64
5.4	WP 45 NEW LC/LU PRODUCTS [SIRS].....	67
<b>6</b>	<b>CONCLUSIONS AND OUTLOOK.....</b>	<b>71</b>
<b>7</b>	<b>REFERENCES .....</b>	<b>73</b>

## List of Figures

Figure 4-1: S-2 Mean true-colour RGB for 2017 for area West of Toulouse.....	45
Figure 4-2: S-1 VV gamma naught descending mean for Area West of Toulouse over the entire year 2017. .....	45
Figure 4-3: S-2 Optical only false colour composite of bands R: NIR MEAN, G: RED MEAN and B: GREEN MEAN for Mean of 2017 for area West of Toulouse.....	46
Figure 4-4: Optical only S-2 false colour composite of R: NDBI MEAN, G: NDVI MEAN and B: MNDWI MEAN for 2017 for area West of Toulouse. ....	46
Figure 4-5: S1/S2 fusion colour composite of bands R: S-1 VV MEAN, G: S-2 MNDWI MEAN and B: S-2 NDBI MEAN for Mean of 2017 for area West of Toulouse.....	47
Figure 4-6: S1/S2 fusion false colour composite of bands R: S-1 VV MEAN, G: S-2 NDMIR MEAN and B: S-2 NDBI MEAN for Mean of 2017 for area West of Toulouse.....	47
Figure 4-7: Maximal NDVI values per pixel: the dark green zones indicate the presence of vegetation, while lighter zones characterize urban areas and water bodies.....	48
Figure 4-8: Computed NDVI median over 19 images for the year 2016, on the whole 31UFS tile. Negative values (minimum at -1) are represented in white and positive values (maximum at +1) in dark green....	49
Figure 4-9: Computed minimal NDVI values per pixel: the lowest values highlight the presence of water bodies and urban areas. ....	49
Figure 4-10: Computed standard deviation NDVI values per pixel: the highest values indicate areas where the NDVI varies the most – here, where vegetation is the densest.....	50
Figure 4-11: Maximal NDBI values per pixel: the black (positive values near +1) values delineate the water bodies with high suspended matter that reflects MIR wavelengths stringer than the NIR.....	51
Figure 4-12: Median NDBI values per pixel: the highest values (in dark grey) are found over urban areas as expected.....	51
Figure 4-13: Computed minimal NDBI values per pixel: the highest values (in dark grey) over urban areas are even more highlighted than with the maximal values.....	52
Figure 4-14: Computed standard deviation NDBI values per pixel: areas where the NDBI varies the most are vegetated, as expected due to the seasonality.....	52
Figure 4-15: Computed median values for the red band (3) per pixel: the blackest values indicate the least reflective zones, while the yellowest are the brightest, as seen in this band.....	53
Figure 4-16: Computed median values for the green band (4) per pixel: the blackest values indicate the least reflective zones, while the yellowest are the brightest, as seen in this band.....	53
Figure 4-17: Computed median values for the narrow red edge band (7) per pixel: the blackest values indicate the least reflective zones, while the yellowest are the brightest, as seen in this band.....	54

Figure 4-18: Computed median values for the wide red edge band (8) per pixel: the blackest values indicate the least reflective zones, while the yellowest are the brightest, as seen in this band..... 54

Figure 4-19: Computed median values for the first SWIR band (11) per pixel: the blackest values indicate the least reflective zones, while the yellowest are the brightest, as seen in this band..... 55

Figure 4-20: Illustration of histogram matching based intercalibration of Proba-V/S-2 for 2 adjacent acquisition dates: (left) Proba-V NDVI histogram, (center) S-2 NDVI histogram, and (right) calibrated Proba-V NDVI histogram ..... 58

Figure 4-21: Calibrated images of Proba-V/S-2 (left) Proba-V NDVI image, (center) S-2 NDVI image, and (right) calibrated Proba-V NDVI image ..... 58

## List of Tables

Table 3-1: List of spectral indices and their use for the creation of time series in published studies. .... 21

Table 3-2: List of textural indices and their use in the creation of time series. .... 32

Table 3-3: List of potential candidate indices for the creation of time series..... 38

Table 4-1: Euclidian distance of LC discrimination using NDBI statistical time-series metrics (maximum, median, minimum, standard deviation). Classes are coded as integers. Cropland = 1 etc. .... 55

Table 4-2: Jeffries-Matusita distance of LC discrimination using NDBI statistical signatures. .... 56

Table 4-3: Euclidian distance of LC discrimination using NDVI statistical signatures. .... 56

Table 4-4: Jeffries-Matusita distance of LC discrimination using NDVI statistical signatures..... 56

Table 4-5: Euclidian distance of LC discrimination using NDBI/NDVI statistical signatures..... 56

Table 4-6: Jeffries-Matusita distance of LC discrimination using NDBI/NDVI statistical signatures. .... 57

Table 4-7: Euclidian distance of LC discrimination using bands 3-4-8-7-11 statistical signatures. .... 57

Table 4-8: Jeffries-Matusita distance of LC discrimination using bands 3-4-8-7-11 statistical signatures. 57

Table 5-1: Classification of the types of methods used during prototype production. .... 60

Table 5-2: WP41 prototype summary. Data, Sites and Methods used as described in Table 5-1. .... 60

Table 5-3: WP42 prototype summary. Data, Sites and Methods used as described in Table 5-1. .... 62

Table 5-4: Comparative training accuracies of the imperviousness testing achieved by using either a) S-1 only, b) S-2 only and c) S-1 plus S-2 predictors. .... 63

Table 5-5: Area-weighted accuracies of IMD 2018 achieved by fusion of S-1 plus S-2 ..... 63

Table 5-6: Area-weighted accuracies of IMCC 2015/17-18 achieved by fusion of S-1 plus S-2 ..... 63

Table 5-7: Area-weighted accuracies of IBU 2018 by fusion of S-1 plus S-2 .....	63
Table 5-8: Accuracies of TCM achieved by fusion of S-1 plus S-2 .....	64
Table 5-9: Accuracies of the forest DLT status layer 2018 achieved by fusion of S-1 plus S-2 .....	64
Table 5-10: Accuracies of the TCC 2017-2018 achieved by fusion of S-1 plus S-2 .....	64
Table 5-11: Benchmarking criteria, chances and issues of the different input data scenarios of TCC* .....	64
Table 5-12 Data and methods used for Grassland prototype production. See Table 5-1 for the legend of different classification methods.....	65
Table 5-13 Comparative training accuracies (overall, producer’s and user’s accuracies) of the grassland status layer classification achieved by using either a) S-1 only, b) S-2 only and c) S-1 plus S-2 predictors and LUCAS 2018 plots.....	66
Table 5-14 Summary of the final grassland status layer mapping accuracy for the reference year of LUCAS training data (2018) following the area-weighted plausibility validation. For the full validation refer to [AD13].....	66
Table 5-15 Data and methods used for the New LC/LU prototype production. See Table 5-1 for the legend of different classification methods.....	67
Table 5-16 Summary of the New LC/LU raster status layer mapping accuracy for the reference year of CLC training data (2018) following the area-weighted plausibility validation. For the full validation refer to [AD14].....	68
Table 5-17 Summary of the New LC/LU vector status layer mapping accuracy for the reference year of CLC training data (2018) following the area-weighted plausibility validation. For the full validation refer to [AD14].....	69

## Abbreviations

2D	Two dimension
AOI	Area Of Interest
ANN	Artificial Neural Network
ARVI	Atmospherically Resistant Vegetation Index
ATPRK	Area-to-point Regression Kriging
AVIRIS	Airborne Visible Infrared Imaging Spectrometer
AVNIR-2	Advanced Visible and Near Infrared Radiometer type 2
BAP	Best-available pixel
BASI	Built-up Areas Saliency Index
BDF	Bayesian Data Fusion
BOA	Bottom of Atmosphere
BRDF	bidirectional reflectance distribution functions
BT	Bovary Transform
BUI	Built-Up Index
CART	Classification And Regression Tree
CLC	CORINE Land Cover
CS	Component Substitution
DEM	Digital Elevation Model
DFA	Discriminant Function Analysis
DIC	digital image correlation
DSM	Digital Soil Mapping
DST	Dempster-Shafer Theory
DTW	Dynamic Time Warping
DVI	Difference Vegetation Index
DWH	Data WareHouse
EAP	Extended Attribute Profile
EBBI	Enhanced Built-Up and Bareness Index
ERS	European Remote-Sensing Satellite
ESTARFM	Enhanced Spatial and Temporal Adaptive Reflectance Fusion Model
EVI	Enhanced Vegetation Index <i>OR</i> Environment Vegetation Index
fAPAR	Fraction of Absorbed Photosynthetically Active Radiation
FCover	Fractional Cover
FLAASH	Fast Line-of-Sight Atmospheric Analysis of Spectral Hypercubes
FOTO	FOurier-based Textural Ordination
FT	Fourier Transform
GEMI	Global Environment Monitoring Index
GLCM	Gray-Level Co-occurrence Matrix
GLCH	Gray-Level Co-occurrence Histogram
GLDV	Grey-Level Difference Vector
HDRF	hemispherical directional reflectance factor
HH	Horizontal transmit/Horizontal receive (polarization)
HIS	Intensity Hue Saturation
HLAC	Higher-order local autocorrelation
HLS	Harmonized Landsat-S-2
HRL	High Resolution Layer
HV	Horizontal transmit/Vertical receive (polarization)
IBI	Index-based Built-Up Index
IND	Indicator approach

IHS	Intensity–Hue–Saturation
ITT	Invitation To Tender
LAI	Leaf Area Index
LC	Land Cover
LC/LU	Land Cover/Land Use
LCLUC	Land Cover/Land Use Change
LU	Land Use
MACCS	Multi-sensor Atmospheric Correction and Cloud Screening prototype
MBA	Modulation-Based Approaches
MERIS	Medium Resolution Imaging Spectrometer
MLC	Maximum Likelihood Classifier
MNDWI	Modified Normalized Difference Water Index
MODIS	Moderate Resolution Imaging Spectroradiometer
MRA	Multi-Resolution Approaches
MS	Multi-Spectral
MSAVI	Modified Soil-Adjusted Vegetation Index
MSI	Multi-Spectral Instrument <i>OR</i> Moisture Stress Index
MUCLAC	MUlti-Channel extension HLAC
NBAR	Nadir BRDF-Adjusted Reflectance
NDBI	Normalized Difference Build Up Index
NBI	New Built-up Index
NBR	Normalized Burn Ratio
NBUI	New Built-Up Index
NDBI	Normalized Difference Built-up Indices
NDFI	Normalized Difference Flood Index
NDMI	Normalized Difference Mud Index
NDSI	Normalized Difference Snow Index
NDVI	Normalized Difference Vegetation Index
NDWI	Normalized Difference Water Index
NIR	Near-InfraRed
NN	Neural Networks
NSA	Numerical and Statistical Approaches
OA	Overall accuracy
OLCI	Ocean and Land Color Instrument
OLI	Operational Land Imager
PA	Producer’s Accuracy
PAN	Panchromatic
PanTex	Presence index by ANisotropic Rotation-invariant TEXtural measure
PAR	Photosynthetically Active Radiation
PC	Post-classification comparison
PCA	Principal Component Analysis
PCS	Principal Component Substitution
PROBA-V	Project for On-Board Autonomy–Vegetation
PVI	Perpendicular Vegetation Index
RBC	Rule-based Classification
RE	RapidEye
RGRI	Red Green Ration Index
RS-2	RADARSAT-2
RVI	Ratio Vegetation Index
S-1	Sentinel 1
S-2	Sentinel 2
S-3	Sentinel 3

SAR	Synthetic Aperture Radar
SAVI	Soil-Adjusted Vegetation Index
SC	Supervised Classification
SG	Savitzky–Golay
SLC	Single Look Complex
SLSTR	Sea and Land Surface Temperature Radiometer
SRTM	Shuttle Radar Topographic Mission
STAARCH	Spatial and Temporal Adaptive Algorithm for mapping Reflectance CHange
STARFM	Spatial and Temporal Adaptive Reflectance Fusion Model
SVM	Support Vector Machine
SWIR	Short-Wave InfraRed
TIR	Thermal InfraRed
TDVI	Temperature Vegetation Dryness Index
TOPSAR	Topographic Synthetic Aperture Radar
TSAVI	Transformed Soil-Adjusted Vegetation Index
TS-X	TerraSAR-X
UA	Users's Accuracy
UC	Unsupervised Classification
UI	Urban Index
VH	Vertical transmit/Horizontal receive (polarization)
VIR	Visible InfraRed
VV	Vertical transmit/Vertical receive (polarization)
WP	Work Package
WT	Wavelet Transform

## 1 Introduction

The Horizon 2020 (H2020) project, “Evolution of Copernicus Land Services based on Sentinel data” (ECoLaSS) addresses the H2020 Work Programme 5 iii. Leadership in Enabling and Industrial technologies - Space, specifically the Topic EO-3-2016: Evolution of Copernicus services. ECoLaSS was implemented from 2017 to 2019 and aimed at developing innovative methods, algorithms and prototypes to improve and invent future next-generation operational Copernicus Land services from 2020 onwards, for the pan-European and Global Components. ECoLaSS makes full use of dense Sentinel time series of optical and Synthetic Aperture Radar (SAR) data. Rapidly evolving scientific as well as user requirements are analysed in support of a future pan-European roll-out of new/improved Copernicus Land Monitoring services, and the transfer to global applications.

Through the combination of S-1 and S-2 data, automated classifiers can benefit from complementary information resulting from wavelength dependent physical interactions with the land surface, which in turn describe different characteristics of the Land Cover and Land Use (LC/LU). The combination of SAR and optical data can improve the differentiation of LC/LU classes and biophysical states and therefore increase mapping confidence. While SAR data contributes information on geometric and di-electric properties, such as vegetation structure and water content, optical data is sensitive to vegetation chemistry and biophysical states, such as photosynthetic activity. By considering the temporal dynamics of these single-datum predictors in addition, for example phenological trajectories, further useful predictors can be derived.

Another kind of integration is addressed concerning time series of S-2 and S-3 (or PROBA-V as a substitute replacement). These sensors deliver a partially corresponding set of spectral bands, which are sensitive for the same biophysical properties but at different spatial resolutions. The additional data-takes and denser time series derived from S-3 offer high potential generating a fusion product of both satellite sensors using interpolation methods. However, as described in [AD06], challenges due to missing S-3 readiness within the ECoLaSS project time-frame were addressed by expanding tests on data-fusion algorithms to PROBA-V data instead.

### 1.1 Purpose and objectives

This report expands on the first issue of the methods compendium [AD05] on S-1/-2/-3 integration strategies aiming at developing and testing the integration of multi-resolution, multi-temporal and multi-sensor data. The objective of WP 31 is to investigate the possibilities of combining S-1, S-2 and further coarse resolution optical data (with the eventual aim being transferability to S-3) with regards to the envisaged evolution of Copernicus Land Services addressed in ECoLaSS. Issue 2 of this report contains further relevant updates concerning the methodology and benchmarking of S-1/S-2 and PROBA-V integration and fusion methods. In addition to the benchmarking and methods compendium of issue 1 [AD05], this issue of the report contributes a high-level summary of the ECoLaSS consortium’s findings and conclusions regarding data requirements for high resolution layer (HRL) production with particular focus on the complementarity of S-1 and S-2 data for an operational production of Copernicus HRLs throughout the work packages of task 3 and task 4 [AD04 – AD15].

The objectives of WP31 are

- to identify adequate pre-processing steps enabling complementary information integration and fusion;
- to identify and explore suitable time series indicators from optical data (S-2)
- to identify and explore suitable time series indicators from SAR data (S-1)
- to explore SAR and optical based indicator approaches as parallel inputs in classification /post-classification schemes;

- to assess the potential of improving S-2 time series by fusion with coarse resolution information;
- to define and develop interpolation and fusion tools of S-2 and S-3 data.
- to summarize the findings regarding the complementarity of S-1 and S-2 across the ECoLaSS application domains

## 1.2 Outline

Chapter 1 of this document is the Introduction. Chapter 2 gives background information on remote sensing for land use / land cover analysis. It outlines the limitation of using optical or SAR times series data solely and the advantages of integrating or fusing them for different classification applications. Chapter 3 describes the state of the art of fusion and integration methods for the fusion of S-1 and S-2 as well as S-2 and S-3 and identifies candidate methods for a possible application within ECoLaSS, while chapter 4 describes the testing and benchmarking of these identified candidate methods. Chapter 5 provides the high-level synthesis of the S-1 / S-2 –complementarity. Finally, chapter Section 6 gives conclusions and an outlook.

In order to increase the impact of the work accomplished in Task3 and Task 4 prototype developments, it was agreed upon that, following the summary of the state of the art approaches in data fusion, this second issue of [AD05] should summarize the approaches developed and tested within ECoLaSS to derive improved and novel CLMS products, with particular focus on the data requirements regarding S-1 and S-2 data as well as the potential for classification improvements through their combination. Except for a number of data fusion tests with S-2 and PROBA-V instead of S-2 and S-3, benchmarking and practical testing initiated in issue 1 has therefore been accomplished and reported in [AD07-AD10].

## 2 Multi-sensoral Remote Sensing for LC/LU Analysis

One of the major challenges of past pan-European high-resolution layer (HRL) production (e.g. 2006, 2009 and 2012) based on optical remote sensing data has been data gaps due to high frequency cloud cover and low sun incidence angles, which significantly impacts any approach on operational LC/LU derivation. Consequences thereof were a) product incompleteness (data gaps due to cloud cover in the final products), b) decreased thematic accuracy in specific regions (e.g. image acquisition not suitable with relation to phenology), c) inconsistency between planned reference year (e.g. image data 2012 +/- 1 year) and actual implementation (partly 2012+2 years for gap filling), d) homogeneity of the product (EO data situation different between most regions of EEA-39), and e) delays in the production of the Copernicus HRLs until sufficient cloud-free observations could be acquired. The need to improve this situation was already expressed by EEA, which is implementing the Copernicus Land Services on pan-European and local level. Even though the availability of two S-2 satellites in constellation did significantly improve the data situation, cloud cover remains the single most challenging drawback of optical data acquisition. Heavy cloud cover over specific regions which coincide with important points in time (phenology-wise) require the additional usage of alternative data sources such as SAR and require new strategies how to combine and integrate multi-source data sets in order to improve the completeness and homogeneity of full coverage high resolution information products on LC/LU.

Therefore, the usage of alternative image data and how to combine and integrate SAR and optical data is introduced in the following. S-1 SAR data are used a) as alternative inputs to close data gaps from optical image sources and b) as complementary information to S-2 to increase thematic classification accuracies of specific classes or c) to derive information, which can be used in the post-processing.

### 2.1 Optical time series data and its limitations

Optical remote sensing data is usually acquired as multi-spectral imagery, sampling important wavelengths in the solar reflective spectrum. Compared to SAR, optical sensors offer more comprehensible images to derive information about LC/CU. For this purpose, the spectral reflectance as well as further features such as spectral indices describing i.e. the condition of vegetation can be employed. Optical data is available operationally for over four decades (i.e. Landsat archive) and, hence, allows the analysis of dense time series to address e.g., change detection of LC/LU. However, cloud coverage is one of the main obstacles and constrains the use of optical imagery (Joshi et al., 2016). The occurrence of clouds often significantly reduces the actual density of the optical time series. A further drawback of multi-spectral data (depending on the spectral and spatial resolution) are similarities in the spectral characteristics of different land cover types, such as between bare soil and built-up areas or between different crop types (Joshi et al., 2016).

### 2.2 SAR time series data and its limitations

SAR data provide limited spectral space (one wavelength and multiple polarisations) and a high radiometric accuracy which is why an application of radar time series analysis is very suitable for temporal information extraction (Schmullius et al., 2015). Moreover, radar systems record data independently from atmospheric conditions, such as cloud coverage and provide information about geometric and dielectric properties of the land surface. Depending on the used wavelength, microwaves can also penetrate the land surface or forest cover. This characteristic allows retrieving data on e.g. soil moisture or growing stock volume. With the launch European Remote Sensing 1 (ERS-1) in 1991, SAR imagery became available at a global scale (Schmullius et al., 2015). Until today, there are, however, only a limited number of studies investigating monitoring of the land surface globally using radar time series (Joshi et al., 2016). Available studies, however, indicate the applicability of SAR time series in the context of e.g. land cover classification, grassland monitoring, and biomass estimation (Joshi et al., 2016). Nevertheless, there are also limitations with respect to the use of radar time series. One of them is the

presence of speckle noise in all recorded SAR images, which may lead to errors in classification maps. Another aspect is the occurrence of geometric distortions due to topography, limiting the usage in mountainous areas.

### 2.3 Advantages of the integration of optical and SAR imagery

With the combination of S-1 and S-2 data, the integration of complementary information is established, resulting from different physical interactions with the land surface, describing primarily different characteristics of the LC/LU. The combination of SAR and optical data can improve the differentiation of vegetation classes and therefore increase classification accuracies. This can be achieved by combining S-1-derived information of the plants structure and the seasonal development of these classes (together with the changing situation of water content, both in the plant canopies and the soil) with information, extracted from optical time series (e.g. S-2) along the year, which indicates the change fraction of photosynthetically active vegetation as a main feature.

### 2.4 Advantages of spatial - temporal fusion of optical imagery

Remote sensing optical sensors are subject to a trade-off between spatial, temporal and spectral resolutions and can often excel only in one of these dimensions. The fusion of optical images offers an advanced way to exploit the full potential of those images by blending their complementary data, thus creating hybrid images at high spectral resolution and high spatial resolution, at the densest available temporal resolution. In particular, in areas experiencing persistent cloud cover, imagery created using fusion algorithms may be a suitable solution to properly characterize temporal dynamics through high-resolution time-series.

This is why another kind of integration can be explored concerning time series of fused images between S-2 and coarse spatial high temporal resolution data, such as S-3 or PROBA-V. S-2 and S-3 feature a corresponding set of spectral bands, sensible for the same biophysical properties with nine overlapping spectral bands in the visible and NIR spectral regions of both sensors, but lower spatial resolution (S-3). The additional data-takes and denser time series derived from S-3 offer high potential generating a fusion product of both satellite sensors using interpolation methods.

On the one hand, the S-2 multi-spectral instrument (MSI) provides a low temporal resolution time series of high spatial resolution images such as images produced by Landsat, Ikonos or Quickbird. While, S-2 images exhibit a spatial resolution ranging from ten to sixty meters, a low revisit time of five to six days, and twelve spectral bands, the S-3 ocean and land color instrument (OLCI) provides a dense time series of low spatial resolution images with a high spectral resolution and enough spectral overlap with the latter, such as images produced by S-3, but also by other sensors like PROBA-V, MODIS or MERIS. The low spatial resolution is compensated by a frequent revisit time, from one to three days, and twenty-one spectral bands.

### 3 State-of-the Art

To monitor land cover and its changes, Earth observation (EO) data with a high temporal and spatial resolution are required. However, up to recently these data needs could only be satisfied by employing data from more than one EO satellite (Gao et al., 2015). Nevertheless, the available EO sensors differ extensively in terms of spatial resolution, temporal acquisition repetition cycles, and spectral bands. Therefore, data fusion approaches have been developed to combine the advantages of different sensors and provide higher value of data and/or classification results. In general, fusion approaches integrate data with different spectral and/or spatial resolutions from two or more sensors in order to exploit both their high spectral and high temporal resolution properties. Furthermore, fusion approaches target the challenges of missing data in a time series (Chust et al., 2004; Reiche et al., 2015). This way, different fundamental physical principles can be used as synergetic information on land properties and compensate the limitations of using only single datasets (Joshi et al., 2016). In this context, the Copernicus Sentinel fleet with its vast span of different sensor and sensing technologies provide the unparalleled opportunity to achieve more accurate mapping products by fusing their data. The Sentinels with the coordinated acquisition strategies and design of S-1, S-2, and S-3 bring up new opportunities and challenges for optical multi-spectral and SAR (C-band) land cover classification on local, continental and global scale with high spatial and temporal resolution (Ferrant et al., 2017; Molina & Datcu, 2016).

In general, image fusion approaches in remote sensing can be categorised according to their level of integration, namely: i) pixel level fusion, ii) feature level fusion, and iii) decision fusion (Joshi et al., 2016; Pohl & Van Genderen, 1998). Image fusion on the pixel level is the computationally most intensive approach because it takes place at the lowest processing level by merging measured physical parameters of two EO datasets at pixel level (Pohl & Van Genderen, 1998). This approach requires a very high geometric accuracy at sub-pixel level to avoid artificial errors being introduced to the fused dataset due to misregistration. Therefore, image data need to be resampled to a common pixel spacing as well as map projection and are limited in geographic coverage to the joint area shared by all datasets (Pohl & Van Genderen, 1998).

The feature level fusion uses different features derived from optical and SAR data prior to using them for classification purposes. Approaches for feature level fusion can grow increasingly complex, e.g. through image segmentation and extraction of fused object features and their geometric properties (e.g. Pohl & Van Genderen, 1998). Advanced fusion approaches use feature extraction from individual sources to selectively induce spatial detail and thus enhance the feature space for better discrimination of objects (Pohl & Van Genderen, 2015; Stefanski et al., 2014).

Decision fusion methods combine results obtained through separate classifications of optical and SAR data (Joshi et al., 2016). This approach has the advantage of being less computationally intensive. Indices and statistics for the classification are calculated for each data set separately and the results of classification are combined by logical AND functions (Pohl & Van Genderen, 1998). The extracted indices and applied classification approaches depend strongly on the thematic focus (i.e., imperviousness, forest, grassland, permanent water bodies, and wetlands).

In the following, this State-of-the-Art section describes necessary pre-processing steps to enable complementary information retrieval, integration and fusion (section 3.1). Methods for the fusion of optical and SAR data to improve classification results are described in section 3.2. Section 3.3 focusses on fusion approaches for high spatial/low temporal and high temporal/low spatial resolution data from different optical sensors (e.g., S-2 / S-3) to exploit the advantage of both datasets. Here, spectral, spatial, temporal interpolation and/or fusion approaches (section 3.3.1) as well as spectral and textural time series metrics/variables (section 3.3.2) are described. The identified approaches are mentioned and discussed in detail keeping the main objectives of the ECoLaSS project such as the update of HRL and

LC/LU classification by improvement of the thematic classification in mind. Section 3.4 discusses candidate integration and fusion approaches for benchmarking.

### 3.1 Pre-processing steps enabling complementary information integration and fusion

Before the actual multi-sensor data fusion, it is of utmost importance to perform all necessary image correction and pre-processing steps (especially dealing with sensor specific effects) to provide the best single data geometry and radiometry (Pohl & Van Genderen, 1998). As multi-sensor data can vary in their spatial and temporal resolution, the pre-processing of the data has to be adjusted with respect to the specific needs and field of application, including sensor specific steps such as calibration, speckle reduction (SAR) or atmospheric correction (optical), and geocoding as well as resampling to a common pixel size (Pohl & Van Genderen, 2015).

A major challenge considering the fusion of optical and SAR imagery is to ensure an accurate co-registration, since spatial mismatch quickly leads to artefacts and misclassifications because different predictors do not represent the same object on the ground (Pohl & Van Genderen, 1998). The objective is to guarantee that measurements of the Earth's surface are accurately aligned in all available images (Pohl & Van Genderen, 1998; M. Schmitt & Zhu, 2016). In cases where precise geo-location cannot be achieved, image data must still be co-registered relative to each other, which is possible by empirical retrieval of a spatial transformation function for every target image, relative to a reference image.

### 3.2 Integration of S-1/S-2 complementary information

The complementary information of optical and SAR EO data provide enhanced information on the LC/LU. While optical data are affected by the physical-chemical characteristics of the surface (such as leaf structure, pigmentation or moisture) SAR data represent the geometric and dielectric properties of the surface (Woodhouse, 2006). For the update of specific HRLs or LC/LU products relevant on a global level, SAR data can improve the thematic classification of various classes (e.g. urban areas, forest), as they respond strongly to physical structures of the scattering elements (Joshi et al., 2016). Balzter et al. (2015) already demonstrated the potential of SAR data to support the assessment of CORINE land cover (CLC) using multi-seasonal S-1 images and derived products from the Shuttle Radar Topographic Mission (SRTM) DEM. S-1 and S-2 data deliver complementary information. Hence, land cover classification tasks can benefit from the fusion of both data types leading generally to higher mapping accuracies.

#### 3.2.1 SAR data as complementary information to S-2

Optical time series have the most suitable spectral information for discriminating different vegetation types and have been applied most frequently among the different sensing systems. However, their main disadvantage is their sensitivity towards weather conditions such as cloud cover, which hampers their suitability in operational applications (Blaes et al., 2005). Contrastingly, SAR data are acquired independently from weather and daytime conditions and often allow for an improved discrimination of structurally different vegetation types due to their diverse response to different polarisation signals (Betbeder et al., 2015; Hill et al., 2000; Schuster et al., 2015; Anne M. Smith & Buckley, 2011). Compared to optical data in the solar reflective spectrum, microwaves are less affected by the physical-chemical characteristics of the surface, but by its structure such as geometry and roughness (Woodhouse, 2006). Active energy scattered by vegetation is dependent on the size, density, orientation, and water content of elements relative to the size of radar wavelength. Most studies utilising both optical and SAR data, rely on a mixture of multi-spectral reflectance values, spectral indices, and different band ratios and band differences from multi-polarised SAR backscatter coefficients (Joshi et al., 2016)). Studies differ further in whether only one single time step or multi-temporal information is being used as input dataset and what output temporal resolution is required.

This subsection presents studies and methods dealing with the synergetic use of optical and SAR imagery to enhance accuracies of classification results. The thematic focus of this section is on applications for the classification of the thematic classes of the HRLs, hence, forest and vegetation monitoring, agriculture and grassland, urban areas, as well as water, wetlands/wetness and soil moisture.

### *Forest and natural vegetation*

In the context of forest and natural vegetation monitoring, several studies are dealing with fusion and/or synergetic use of optical and SAR data. Reiche et al. (2015) presented a pixel based tool called MultiFuse, which is based on time series of Landsat NDVI and ALOS PALSAR-L-band backscatter data. It exploits the full information content of both optical and SAR time series data for the detection of abrupt human induced deforestation in tropical regions. At this, pre-processing of optical data comprises cloud cover and cloud shadow masking using the FMask algorithm (Z. Zhu et al., 2015), atmospheric correction, and reprojection. The pre-processing of PALSAR data includes multi-looking, radiometric calibration using standard calibration coefficients, topographic normalisation and geocoding. Based on the pre-processed optical data a NDVI time series is calculated. The SAR data is used to compute a time series of HH, VV images and a HHVV ratio. Next, the SAR images are temporally filtered by an adaptive multi-temporal approach to reduce speckle noise. The actual fusion consists of two main steps. First, the relationship between both Landsat NDVI and PALSAR backscatter time series is analysed by means of a correlation analysis. Next, a regression model is applied to estimate a time series based on the available data. Reiche et al. (2015) conclude that the classification results based on NDVI time series only provide low spatial and temporal accuracy. Contrastingly, the fused dataset indicates significant improvements in deforestation detection compared to single source observations. Furthermore, the authors note that the multi-temporal speckle filtered HHVV ratio dataset shows the strongest correlation with the NDVI time series. This might be due to reduced sensitivity of the ratio index towards environmental covariates such as changing moisture conditions.

Lehmann et al. (2015) analysed the fusion of SAR and optical data in the framework of a large-scale operational forest monitoring system. This study assessed the contribution of complementary information derived from Landsat, L-band PALSAR, and C-band RADARSAT-2 (RS-2) data for forest detection. For this purpose, independent as well as joint SAR/optical classifications have been tested. The authors investigated a “low cost” approach by considering advantages of established and proven monitoring systems. Thereby, they focused on temporal consistency considering time series of remote sensing data instead of single acquisitions. The pre-processing of Landsat data includes re-projection and resampling to a common spatial reference, calibration to top-of-atmosphere reflectance, correction of scene-to-scene differences (using bidirectional reflectance distribution functions (BRDF)), calibration to a common spectral reference (using invariant targets), and correction for differential terrain illumination. Additionally, the pre-processing of PALSAR and RS-2 data includes multi-looking, speckle filtering (Lee filter), geocoding, radiometric calibration and normalisation, as well as correction for terrain-induced illumination differences (Lehmann et al., 2015). As mentioned before, also in this study the co-registration of SAR and optical data are essential. The authors applied a digital image correlation (DIC) approach which is based on gradient cross-correlation. Furthermore, the authors tested 18 different texture measures related to the degree of disorder, similarity and central tendency on pixel level. The combination of Landsat and C-band was found to provide highly enhanced results, whereas the texture information and single-date C-band SAR data delivered only limited improvements. The analysis of the used feature space indicates that adding texture features did not automatically correlate with significant improvements of forest classification results. Nevertheless, texture features improved the results in distinct and more complex areas such as urban regions. In such context, the consideration of texture features depends on the scale of the study area and the spatial resolution.

A study of Vaglio Laurin et al. (2013) presents an approach based on multi-spectral Landsat TM imagery, the Advanced Visible and Near Infrared Radiometer type 2 (AVNIR-2) and PALSAR synergies for forest and land cover mapping in the tropical regions of Africa. The optical data is atmospherically corrected

with hemispherical directional reflectance factor (HDRF) using the Fast Line-of-Sight Atmospheric Analysis of Spectral Hypercubes (FLAASH) algorithm of the ENVI software. In addition, a haze removal is performed. Multi-looking, terrain-correction and geocoding is applied to PALSAR images. The texture variables used in this study include the mean, entropy, correlation, variance, and second moment based on Grey-Level Co-Occurrence Matrix (GLCM). However, the calculation of texture features is limited to bands that are sensitive to vegetation. Hence, bands 4, 5, and 7 of Landsat TM, bands 3 and 4 of AVNIR-2, as well as for both PALSAR polarizations are considered, using 64 grayscale quantization levels, 1 pixel shift and  $3 \times 3$ ,  $5 \times 5$ ,  $7 \times 7$ ,  $9 \times 9$  and  $15 \times 15$  window sizes. For classification purposes two methods, specifically, the Maximum Likelihood (MLC) and Neural Networks (NN) classifiers are used. The results show that the combination of the abovementioned data sources provides the best results for both classification methods (91.1% and 92.7% for Landsat TM as optical input and 95.6% and 97.5% for AVNIR-2 as optical input, respectively). In this study, texture features improve the classification results significantly by 10.1% and 13.2%, respectively (Vaglio Laurin et al., 2013).

A near real time forest disturbance mapping based on S-1, S-2 and Landsat-8 time series data is conducted by Hirschmugl et al. (2017). They used a sequential approach where an initial forest / non-forest classification is derived from optical data and, afterwards, forest disturbance data are derived by means on the Bayes' theorem using SAR and optical data stacks. Disturbance mapping is performed separately on each input dataset and then fused to one forest disturbance dataset based on specific weighting functions. For optical data the authors apply common pre-processing steps using FMask for Landsat-8 and Sen2Cor for S-2 data. The S-1 data are pre-processed with Joanneum Research software RSG including processing to gamma nought based on SRTM and multi-looking to 20m. A modified Frost and a multi-temporal filter with a window size of  $3 \times 3$  pixels are used to reduce speckle noise. In this study, all available images are reduced to temporal statistics including the metrics mean, minimum, maximum backscatter, standard deviation, coefficient of variation, mean of the first three images, and mean of the last three images. Next, the information on forest disturbance is derived using a threshold-based approach with the assumption that forest cover change is characterised by high backscatter variation similar to agricultural areas (Hirschmugl et al., 2017). At this, positive backscatter values are related to vegetation regrowth and negative backscatter values with vegetation loss. The final combination of individual classified results is based on defined probabilities and weighting factors by the user. The results indicate that when using only S-1 for forest disturbance detection 43.56% of the areas are classified correctly. For the optical data the percentage of detected areas amounts to 79.95%. To sum up, the synergistic use of optical and SAR improves the detected percentage of disturbed areas to 83.67%.

### *Agriculture and grassland*

With regards to agriculture and grassland applications, several studies have been performed over the last two decades using optical and SAR data to achieve higher thematic accuracies. In similar studies, classification results derived by either optical data, SAR data (C-, X-, L-band) or the combination of both were compared to each other. The objective of these studies was to create dense time series during the growing season of crops, combining regular SAR time series and optical time series with irregular time intervals using derived statistical metrics. A variety of approaches jointly apply multi-sensor imagery from SAR and optical satellites for the classification of vegetation classes, such as crop types (Blaes et al., 2005; Brisco & Brown, 1995; McNairn et al., 2009), and crops combined with more general land-cover classes (Waske & Benediktsson, 2007; Waske & van der Linden, 2008), or for the estimation of herbaceous biomass (Svoray & Shoshany, 2003). Villa et al. (2015) investigated main crop type identification by SAR and optical time series up to the early growing season (here mid of July), using indicators like the Enhanced Vegetation Index (EVI), Red Green Ratio Index (RGRI) and the Normalized Difference Flood Index (NDFI) in optical data and sigma nought backscatter coefficients from X-Band SAR. Bach et al. (2012) and Dotzler et al. (2013) demonstrated the information potential of TerraSAR-X (TS-X) for certain growing phases of crop types delivering similar results compared to a Leaf Area Index (LAI)

retrieval from RapidEye (RE) data, in order to perform yield modelling for wheat and to assess heterogeneous growing patterns within the fields. Jordi Inglada et al. (2016) presented an approach for early crop type identification especially for the start of growing season when cloud coverage is a major challenge. They assessed the impact of data fusion using SAR image features aiming at temporal gap filling of optical time series. Polarisation ratio, local mean and VV data with textures described by Haralick et al. (1973) were used and assessed as useful features enhancing the accuracy of the results. This kind of crop detection is essential for yield forecasting and irrigation management, especially for crop types with more than one annual cycle. Le Hégarat-Masclé et al. (2000) investigated the use of ERS data and Landsat TM over a test site east of Paris dominated by agriculture with ten different land cover types based on unsupervised classification and Dempster-Shafer evidence theory framework. The study shows that using multi-source data as input to the classification leads to more robust and reliable results. A systematic improvement was found by fusing SAR and optical data sources especially for land cover types with minor surface coverage.

Notarnicola et al. (2017) used S-1 and S-2 data for mountain crop monitoring. S-1 backscatter coefficients in VV and VH polarisation were used to monitor the trend over different crop types that are extracted from the existing land cover classification CORINE 2012 (meadows, pasture, orchard, vineyards and forest as additional class). The generated time series from S-1 data was compared with S-2 NDVI time series. According to the preliminary results of this study, the highest dynamics are associated to meadows, which were strongly managed in terms of fertilisation, irrigation, and mowing. The signature of meadows varies between -16dB and -12dB and from -22dB and -17dB for VV and VH polarisation, respectively. This trend is clearly different from natural grassland as well as from other classes. Furthermore, the study indicates that due to the C-band configuration both polarisations (VV and VH) are strongly dominated by vegetation characteristics and may have a limited sensitivity to soil characteristics. Notarnicola et al. (2017) found a high correlation between the features VH polarisation and S-2 NDVI with a coefficient of determination of 0.81.

Recently, Veloso et al. (2017) published a study focusing on the temporal behaviour of crops (wheat and barley, rapeseed, maize, soybean and sunflower) based on data comparable to S-1 and S-2. For this, S-1 data are pre-processed with SNAP software to derive the calibrated backscatter coefficient. Additionally, a multi-looking is applied to reduce speckle noise resulting in an output image at a spatial resolution of 20m. Furthermore, terrain correction is applied to generate accurately geocoded images by correcting geometric distortions (foreshortening, layover and shadow) using SRTM data (Veloso et al., 2017). The used optical data are atmospherically corrected using the Multi-sensor Atmospheric Correction and Cloud Screening prototype (MACCS) spectro-temporal processor (Hagolle et al., 2008; Hagolle et al., 2010, 2015). With respect to crop monitoring, the study showed that wheat and rapeseed are better distinguished using VH and VV backscatter between March and July and using NDVI between November and December. Regarding summer crops, Veloso et al. (2017) recommend using VH/VV and VV to separate maize, soybean and sunflower during the heading/flowering phase. Their results also indicate that for the identification of the crop types barley and maize, both NDVI and VH/VV profiles provide reliable results.

Navarro et al. (2016) applied crop monitoring for the estimation of crop water requirements. For this purpose, they used SPOT NDVI and time series of dual (VV + VH) polarisation backscattering based on S-1 to compute the basal crop coefficient curve for four crop types (maize, soybean, bean and pasture) and to estimate the length of each phenological growth stage. The main objective of this study was to assess the potential of multi-temporal and multi-source data for crop parameter estimation and crop type identification at high spatial (10m) and temporal (5 days) resolution focusing on irrigated agriculture. The authors observed a significant correlation of determination between NDVI and backscatter time series for all considered crop types, pointing that multi-spectral imagery can be replaced by SAR imagery data to fill gaps caused by cloud coverage. Furthermore, the authors assessed the integration of S-1 VV + VH polarised data into the classification process and compared the obtained accuracies between the

different configurations. For classification purposes, two supervised methods, specifically the support vector machine (SVM) and neural network (NN) are used. Here, the results indicate that NN delivers slightly better accuracies compared to the SVM classifier. However, the land cover classification could not be improved when using SAR and optical data in combination, which could be seen in the results where the highest overall accuracy was achieved by using SPOT images solely.

The combined use and/or comparisons of classifications by optical and SAR intra-annual time series or multi-seasonal data were also performed for grassland mapping (Dusseux et al., 2014; Hill et al., 2005; Schuster et al., 2015). A. M. Smith et al. (1995) analysed ERS-1 SAR data together with Landsat TM, SPOT VIR, and airborne optical imagery to assess the combination of radar and optical data for monitoring rangeland in the Agriculture and Agri-Food Canada Research Substation at Onefour (Alberta) by means of discriminant function analysis (DFA). The combination allowed obtaining an improved categorisation of the vegetation classes with respect to considering each data type separately. Moreover, while optical data proved to be more suitable to characterise the vegetation status, SAR imagery provided key information about the structure and surface topography. Also Price et al. (2002) used a classification system based on the DFA to study the separability of three tallgrass land management practices in eastern Kansas (USA), where usually cool- and warm-season grass species occur, by means of three multi-seasonal Landsat TM and four multi-seasonal ERS-2 SAR images, as well as their combination. The results showed that by using Landsat TM data alone, performances were better than those obtained with ERS-2 imagery and, when combined, the SAR data did not allow increasing the classification accuracy. Hill et al. (2005) showed the potential of improving the categorisation of heterogeneous herbaceous cover in pastures and grasslands by combining independent classifications obtained by means of mono-temporal Landsat TM and Jet Propulsion Laboratory AirSAR data. Experiments were performed for a test site in the Cervantes area (Australia) using an unsupervised version of the Complex Wishart classifier for the C-, L-, and P-band polarimetric SAR data as well as a principal component analysis on the green, red and near-infrared Landsat bands followed by a centroid distance measure clustering. In particular, they were able to map vegetation types based on the different sensitivity of SAR and multi-spectral sensors to specific vegetation characteristics. Erasmi (2013) assessed the capability of combining optical (six RE scenes) and SAR (four RS-2 and six TS-X scenes) data for the classification of semi-natural habitats over the study site Schorfheide Chorin in eastern Germany and compared the results with single sensor classifications. The object-based classification was performed by means of a classification and regression tree (CART) algorithm. Results showed that single-sensor classifications based on multi-temporal RE data outperformed the ones carried out with TS-X and RS-2 data and demonstrated that bi-sensor combinations of optical and SAR data resulted in classification accuracies between 60.83% and 84.53% (with RS-2 polarimetric data providing higher classification accuracies than TS-X). Furthermore, Talab-Ou-Ali et al. (2017) used S-1, S-2 and SPOT data for monitoring coastal vegetation in France. Also Chang and Shoshany (2016) conducted preliminary research for S-1 and S-2 data focusing on shrubland biomass estimation. Their fusion model showed 14% improvement compared to single sensor models ( $R^2$  increases from 0.72 to 0.86). Their proposed fusion technique is mainly controlled by S-2 data and is supplemented by an active S-1 data supporting vegetation structure/density information.

For all vegetation-covered targets, only a limited additional benefit is seen because of the high level of temporal decorrelation (Morishita & Hanssen, 2015; Wei & Sandwell, 2010). In the context of crop area and crop status monitoring, interferometric coherence has the potential to enable the mapping of stable (unvegetated) surface with possibilities of farming practises and crop detection. To date, most common polarimetric decompositions (Freeman & Durden, 1998) can only be computed for fully polarimetric (quad-polarimetric) data. S-1 only contains dual-cross-polarimetric capabilities (HH-HV, or VV-VH) for which there is a need for further developments. Alternative concepts for the use of dual-polarimetric data have been published by A. Schmitt et al. (2015).

## *Urban*

Considering the usage of multi-source data in the framework of land cover and urban applications there is a number of recently published studies. Michelson et al. (2000) successfully applied Landsat TM and ERS SAR data for country-wide land cover classification over Sweden. Balzter et al. (2015) have demonstrated the potential of SAR data, to support the assessment of CORINE LC using multi-seasonal (two coverages) S-1 images and derived products from SRTM DEM. Haas and Ban (2017) used S-1 and S-2 data for ecosystem mapping within urban areas based on image segmentation and classification. The synergy of S-1/S-2 enabled large-scale urban analysis with utilising spatial characteristics and topological relations (e.g. area, contiguity, perimeter-to-area ratio and distance). Another study of Chen et al. (2003) used Intensity–Hue–Saturation (IHS) transformation to integrate the high spectral resolution, provided by hyperspectral data (Airborne Visible Infrared Imaging Spectrometer, AVIRIS), and the surface texture information, derived from radar data (Topographic Synthetic Aperture Radar, TOPSAR), into a single image of an urban area. In this way, several urban land cover types are resolved to a larger degree using the higher spectral and spatial resolutions and the synergistic visual content provided by the fused image. Furthermore, Marconcini et al. (2017) presented an approach employing the temporal statistics of different spectral indices derived from Landsat-8 and of the S-1 backscattering to classify urban areas at a 10m spatial resolution on a global scale.

## *Water and wetlands/wetness*

Yesou et al. (2016) used S-1 in the context of flood and wetland mapping and showed that it ensures monitoring of water bodies, whereas optical S-2 imagery provides complementary information on vegetation, floating or growing on sand banks. Furthermore, Taha and Elbeih (2010) concluded that for water/non water separation HIS fused data clearly indicate highest accuracies. Jenerowicz and Siok (2017) conducted tests on mapping water bodies based on S-1 and S-2 data, comparing the results of individual features and thresholds. The results also imply that complex detection of water bodies e.g. quality monitoring of water reservoirs can be improved. Clement et al. (2017) analysed detailed flood mapping using different polarisations of S-1 data.

Q. Gao et al. (2017) presented an approach for soil moisture mapping over agricultural fields at 100m spatial resolution based on the interpretation of S-1 data recorded in the VV polarisation and combining S-1 with S-2 data for the analysis of vegetation effects. The authors present an approach to map soil moisture using S-1 and S-2 data in a synergistic way. The reduction of spatial resolution from 10m to 100m is conducted to decrease uncertainties due to different types of heterogeneities in agricultural fields such as local changes in roughness as well as heterogeneities in vegetation cover. All available S-1 data are pre-processed with respect to noise removal, radiometric calibration, and terrain correction. S-2 data are used to calculate NDVI, but prior to NDVI derivation a cloud mask is generated using the QA60 band. In this study, two methods are proposed to retrieve soil moisture. The first one comprises a change detection technique based on an inversion approach, which was already successfully applied on ERS data and now adjusted to S-1 data. The second one takes into account the difference of the S-1 backscatter coefficient observed over two consecutive acquisitions. By analysing two consecutive observations only a small temporal change of vegetation is expected for a nearly constant value of roughness and thus the difference of the backscatter signals depend mainly on the change in soil moisture. Both methods also take into account the S-2 NDVI. The results of this study indicate that both methods are suited for soil moisture estimation and the necessity to further research with respect to vegetation discrimination and the consideration of a larger time series of S-1 (Gao et al., 2017).

A further study of Poggio and Gimona (2017) compared MODIS, Landsat, S-2 and S-1 data for Digital Soil Mapping (DSM). The authors applied several configurations and concluded that the synergistic use of optical and radar datasets provided the best estimation models and most accurate results. The findings include that S-1 data is suitable for the analysis of soil properties and texture in particular. Also Baghdadi et al. (2015) worked on soil moisture and LAI retrieval over irrigated grasslands from RS-2 and Landsat-

7/-8 data. The main objective was to study the relevance of features extracted from SAR (backscattering coefficient, polarimetric information) and optical images (NDVI, Fraction of Absorbed Photosynthetically Active Radiation (fAPAR) and Fractional Cover (FCover)) for retrieving soil moisture, leaf area index, biomass, and vegetation water content and height. The authors summarised their outcome as follows: i) HH polarisation is the most relevant information among the SAR layers, ii) dual or full polarisation modes do not improve the estimation of soil moisture and vegetation parameters, and iii) the use of polarimetric parameters (Shannon entropy and Pauli components) does not improve the estimation of soil moisture and vegetation parameters.

### 3.2.2 Conclusions

As described above, studies using the combination of S-1/S-2 data show promising results and underline that accuracies of different thematic classifications based on fused image data frequently exceed those based on single source data (Joshi et al., 2016). However, most studies focussed on using optical/SAR fusion for improving mono-temporal classifications to define more enhanced land cover properties rather than for change detection (Joshi et al., 2016). Besides, it is key to select suitable data fusion techniques for different land cover classifications and change detection (Lu et al., 2014).

The above-mentioned studies and reports underline the positive synergy between SAR and optical data. Especially, the combination of data of the Sentinel fleet show great potential in terms of geometric consistency and enhancement of thematic classification and change detection. For the update of specific HRLs or LC/LU products relevant on a global level, complementary information derived from S-1 can improve thematic classification based on optical data of various classes (e.g. settlements structures or forest differentiation), as they react mainly on vertical or structures with steep slopes based on double bounce backscatter effects.

For crop area and crop status monitoring, SAR based parameters can provide complementary information to optical based parameters due to their different physical interactions with the land surface. Therefore, different characteristics of LC/LU objects can be described and classification can be improved. In order to maintain the experiences from previous Copernicus HR Layer production, the ECoLaSS consortium assessed in phase II of the project, where applicable, whether and how parameters derived from dense SAR time series can supplement the available optical time series data for the production of incremental HRLs.

### 3.3 Integration of S-2/S-3 (fusion)

This subsection focusses on methods for the fusion and integration of S-2 and S-3. Thereby, current state-of-the-art methods for a spectral, spatial as well as temporal interpolation/fusion are being presented (subsection 3.3.1). Furthermore, spectral and textural time series metrics/variables are being identified which are suitable to describe seasonal dynamics of LC/LU and thus are potentially useful in a S-2/S-3 fusion/integration approach (subsection 3.3.2)

#### 3.3.1 Spectral, spatial, temporal interpolation and/or fusion approaches

This subsection investigates and describes various spectral, spatial and temporal interpolation and fusion approaches for the integration of S-2 and S-3 time series. It assesses in particular the potential of improving S-2 time series by fusion with S-3 information to avoid land cover mapping distortions caused by cloud cover. Firstly, an overview of the optical data fusion at the pixel-level is presented. Secondly, advanced and appropriate methods for the S-2 and S-3 data fusion are explained in detail.

### 3.3.1.1 Overview of the optical data fusion at the pixel-level

The pixel-level fusion, mainly focusing on optical data, is the combination of raw data from multiple sources into single resolution data, which are expected to be more informative and synthetic than either of the input data. The purpose is to improve spatial resolution, enhance structural and textural details or retain the spectral fidelity of the original multi-spectral (MS) data simultaneously (Zhang, 2010). There are many ways to address pixel-level image fusion due to its diverse input in terms of multi-modal images and its variability in terms of targeted outcome (Pohl & Van Genderen, 2015). Depending on users' need, a large variety number of pixel-level algorithms have been developed and widely applied for the data fusion of remotely sensed images.

In particular, much attention has been paid on the aspect of increasing the spatial resolution of MS images by introducing spatial detail derived from a higher spatial resolution panchromatic band (PAN), while preserving the high spectral resolution properties of MS images. This fusion method is commonly called 'pansharpening'. A major reason for its popularity is the accessibility of single platform acquisitions, which avoids the introduction of errors due to temporal changes on the ground as well as geometric problems arising from multiple platform orbits. Thus, pansharpening has become one of the most popular approaches in remote sensing image fusion (Pohl & Van Genderen, 2015; Zhang, 2010).

Although there are many categorizations suggested for remote sensing data fusion approaches, pixel-level pansharpening fusion methods have been categorized by Pohl and Van Genderen (2015) in five groups: (i) component substitution (CS); (ii) numerical and statistical approaches (NSA); (iii) modulation-based approaches (MBA), (iv) multi-resolution approaches (MRA), and (v) hybrid techniques. (i) The CS techniques convert a number of bands of the original image into another data space (e.g. another colour space) where one of the resulting channels is replaced by a new image (e.g. higher spatial resolution image). The reverse transform creates the actual fused image containing information from both input data. Within this category, the intensity hue saturation, principal component substitution (PCS), and the Gram-Schmidt techniques are most frequently exploited. CS methods suffer from spectral distortion due to the significant incompatibility of PAN (or any high spatial resolution image) and substituted component. (ii) The NSA perform multiplicative operations, create subtractive and ratios images. Widely used Boverly transform (BT) resides in spectral modelling intended to reach a normalization of the input bands via addition, subtraction and ratio. The principal component analysis (PCA) is also a very popular algorithm. It implies the replacement of the first PC by a high-resolution (e. g. a PAN or a low spatial MS) image. (iii) The MBA uses a ratio between the PAN and its low-pass filtered image with a further modulation of a lower spatial MS image. (iv) Whereas the previous methods are based on various linear combinations and substitutions of the original bands, the MRA are nonlinear. The MRA-based approaches decompose images into multiple channels depending on their local frequency content, employing wavelets, curvelets, contourlets and similar transforms. They find their application in deriving spatial detail to be imported into finer scales or multi-spectral images. The wavelet methods may suffer from color distortions.

Most of these data fusing approaches are devoted to the case of spatial or spectral enhancement of remotely sensed images only in the case of simultaneous images. However, they may not be suitable for capturing quantitative changes in surface reflectance, e.g. caused by phenology (Gao et al., 2006) or crop growth. In addition to the traditional spatio-spectral data fusion methods (typically pansharpening), pixel-level fusion can also aim at increasing the temporal resolution of a sensor of low temporal resolution but high spatial resolution images through fusion with the data with lower spatial resolution but higher temporal resolution (Dominique Fasbender et al., 2009; F. Gao et al., 2006; Sedano et al., 2014; Xue et al., 2017). For multi-temporal data, the purpose of pixel-level fusion is to highlight the informative changes between different times, using either the same or different sensors.

Some methods interesting for the fusion of S-2 and S-3 images are explained in more detail here below. Spatial and spectral enhancement methods are firstly explained. Then, by the temporal component of

the fusion between sensors of high and low temporal resolution is reviewed through several applications. Finally, some cases of fusion at the product level are presented.

### 3.3.1.2 Spectral and Spatial Fusion

#### *Pansharpening and spatial enhancement in a Bayesian data fusion framework*

As previously explained, fusion methods for spatial enhancement, or pansharpening methods, are a set of techniques aiming at improving the spatial resolution of remotely sensed multi-spectral images. Pansharpening is frequently applied to a single optical sensor data containing both PAN and MS data, in order to benefit from both sources of information, but sometimes also applied to multi-source data provided by two independent optical sensors differing in spatial, spectral and temporal resolution. Ideally, the outcome of pansharpening is an artificial image identical to the image that the MS sensor would yield provided it had the spatial resolution of the panchromatic.

In Fasbender et al. (2007), Fasbender et al. (2008a) and Fasbender et al. (2008), a novel approach to the pansharpening and spatial enhancement problems is suggested within a Bayesian framework, using IKONOS, SPOT 5, SPOT-VEGETATION and ASTER images. A Bayesian data fusion (BDF) framework has been proposed by Bogaert and Fasbender (2007). Initially developed in a spatial prediction context, it also provides a consistent framework for fusing an arbitrary large number of information sources that are related to the same variable of interest. This BDF method relies on statistical relationships between the various spectral bands and the panchromatic band without suffering from restricting modeling hypotheses.

Furthermore, BDF allows the user to weight the spectral and panchromatic information with respect to either visual or quantitative criteria, which leads to adaptable results according to users' needs and study areas (Fasbender et al., 2008). This ability for balancing spectral and spatial information is one of BDF's most appealing features. For example, photointerpreters may wish to favor image sharpness with a weighting parameter close to one, while automated procedures may require a better color consistency and, thus, a lower weight for panchromatic information. Results showed that BDF yielded the highest spectral consistency, and small details were adequately added to the pansharpened images with little artifact as compared to those created using wavelet-based methods. No particular colour distortions are observed and quantitative quality criteria (i.e. correlation coefficients) attest that the BDF framework provides significant results in the case of pansharpening application.

The BDF approach is also tested for the enhancement of the spatial resolution of coarse images using higher resolution images coming from same or different sensors (Fasbender et al., 2007; Fasbender et al., 2008), showing interesting results. Contrary to the pansharpening application, several higher resolution spectral bands were available. The method can be used to derive high resolution reflectance values based on medium resolution observations by taking advantage of a multivariate approach including covariate information (i.e., spectral information is processed as a whole and not band by band). The high values of the correlation coefficients between original and fused coarse resolution spectral bands indicate that no particular colour distortions are noticed, whereas small details and linear patterns were added.

The BDF has performances similar or higher to the wavelets approach. The main advantage of Bayesian approaches is to set the problem in a proper probabilistic framework. In addition, as it does not have any intrinsic limitations on the type of data to be processed or the number of bands to be merged, it could be used for optical/SAR or hyperspectral image fusion.

### *Multi-spectral and -spatial data fusion between S-2 MSI and other sensors*

In Korosov et al. (2017), a fusion between S-2 and S-3 is simulated by choosing the analogue Aqua-MODIS sensor to the S-3 OLCI instrument. The S-3 data present a good set of colour wavelengths, but a rather coarse (300m) spatial resolution, while the MSI data on S-2 have much higher spatial resolution (10-60m) but a more sparse number of spectral channels in the visible spectrum. The data are fused at pixel-level to get products with values of remote sensing reflectance wavelengths of OLCI and with MSI spatial resolution of 60m using an artificial neural network (ANN).

Many of applications indicated that the ANN-based fusion methods had more advantages than traditional statistical methods, especially when input multiple sensor data were incomplete or noisy. It is often served as an efficient decision level fusion tool for its self-learning characters, especially in LC/LU classification. In addition, the multiple inputs-outputs framework make it to be a possible approach to fuse high dimension data, such as long-term time-series data or hyper-spectral data. Comparison of reflectance values from MODIS and fused data shows high level of agreement and suggests that the developed algorithm can be successfully applied for fusion of data from S-2 and S-3 (Korosov et al., 2017).

Further recent studies are dedicated to the fusion of S-2 with Landsat imagery, the most widely accessible medium-to-high spatial resolution multi-spectral satellite data. Since S-2 and Landsat data have similar wavelengths, this combination provides an excellent opportunity for synergistic use of these two types of satellite sensor data (Wang et al., 2017). Their combination offers a unique opportunity to observe globally at medium spatial and temporal resolution, and thus creates unprecedented opportunities for timely and accurate observation of Earth status and dynamics. This is particularly valuable for areas that are often covered by clouds, thereby, contaminating some Landsat or S-2 observations.

In Wang et al. (2017), a new approach (the area-to-point regression kriging (ATPRK)) is presented for the fusion of Landsat 8 Operational Land Imager (OLI) and S-2 MSI data to coordinate their spatial resolutions for continuous global monitoring. ATPRK treats the coarse band as the primary variable and the fine spatial resolution band (hereafter, fine band) as a covariate. It is an advanced image fusion approach which has the appealing advantage of precisely preserving the spectral properties of the observed coarse images (i.e., perfectly coherent). It was shown to outperform 13 methods in pan-sharpening. The 30 m spatial resolution Landsat 8 bands are downscaled to 10 m using available 10 m S-2 bands. To account for the LC/LU changes that may have occurred between the Landsat 8 and S-2 images, the Landsat 8 PAN band was also incorporated in the fusion process. The experimental results showed that the proposed approach is effective for fusing Landsat 8 with S-2 data, and the use of the PAN band can decrease the errors introduced by LC/LU changes.

The Harmonized Landsat-S-2 (HLS) project is a NASA initiative to produce a consistent, harmonized surface reflectance product from Landsat OLI and S-2 MSI data at 30m spatial resolution. The HLS will be beneficial for global agricultural monitoring applications that require medium spatial resolution and weekly or more frequent observations. In this context, a “harmonized” reflectance product means that necessary radiometric, spectral, geometric, and spatial corrections have been applied to create a seamless time series, such that it is transparent to the user which sensor contributed any particular observation. To create a compatible set of radiometric measurements, the HLS product relies on rigorous pre- and post-launch cross-calibration activities. The processing chain includes the following components: atmospheric correction and cloud/shadow masking based on OLI and adapted to the MSI data, nadir BRDF-adjustment given the differing solar and view angles associated with Landsat-8 and Sentinel-2, spectral-adjustment, regridding, and temporal composite to produce the M30 (10-day NBAR 30m Landsat-8 OLI or S-2 MSI harmonized surface reflectance resampled at 30m over the S-2 tiling system). The spectral-adjustment, or band pass adjustment, relies on a linear fit between equivalent spectral bands from the two sensors which present small differences. This band-to-band linear

regression has been calibrated and evaluated using synthetic data and surface reflectance processed from a large number of hyperspectral EO-1 Hyperion scenes globally distributed.

### 3.3.1.3 Temporal fusion between high and medium spatial resolution time series

S-2 data with improved high spatial resolution and higher revisit frequency will play a fundamental role in monitoring land cover at regular intervals. Nevertheless, technological limitations pose challenges for sensor designs, and trade-offs have to be made to balance spatial details with the spatial extent and revisit frequency (Xue et al., 2017). High spatial resolution images, such as Landsat, and S-2 with revisit cycles of 16 and 5 days respectively, are indeed limited in their applications due to frequent cloud contamination. Cloud-free high resolution imagery may not be available at the required period, which hinders the time series availability and consequently the continuous land surface monitoring. On the contrary, low spatial resolution sensors, such as MODIS, PROBA-V, SPOT-VEGETATION and recently S-3, have a daily revisit period but a relatively low spatial resolution ranging from 250 m to 1000 m, limiting its effectiveness in the monitoring of ecosystem dynamics in heterogeneous landscapes.

In an attempt to overcome these limitations, the synergistic use of high spatial resolution images such as Landsat or S-2 time series with the high temporal frequency of coarse resolution sensors (MODIS, S-3), while taking explicitly into account the spatial resolution discrepancies between images, is investigated. For instance, monitoring agriculture via remote sensing or detecting rapid surface changes are typical applications where the combination of fine spatial resolution and a frequent temporal revisit time is important.

Pansharpening methods previously described are devoted to the case of spatial and spectral enhancement of remotely sensed images only in the case of simultaneous data acquisition. This section presents some examples of temporal fusion models, in addition to spectral and spatial merge.

#### *Radiometric calibration*

Radiometric calibration is an imperative pre-requisite before any data fusion attempt. Without a common radiometric basis, proper fusion is not possible, mainly due to:

- Different spectral responses from both sensors;
- Different atmospheric conditions (aerosol presence, atmospheric composition), potentially generated by different times of capture for both images;
- Different physical set-up for the satellites, such as sun angles, satellite inclinations, both leading to different illuminations, etc.

There are two types of calibrations: relative and absolute.

The absolute calibration is the most accurate, but also the most demanding in terms of required auxiliary information. It requires not only sensor parameters, but also all available atmospheric parameters at the given time of data acquisition (composition, refraction coefficient, scattering estimation, partially based on aerosol presence and types).

In comparison, the methodology of the relative calibration is much simpler. One of the images is set as a reference, and the other sees its properties being adjusted until a match with the reference's ones is found.

Several techniques can be used to achieve this relative calibration. The most effective and simple is the histogram matching, where a time series or a single image is modified by matching its histogram to the reference histogram. It can be used to match images from different sensors with slightly different

spectral responses or to match different images from the same sensor whose response changes over time.

A cumulative histogram is calculated for each dataset (the reference and the one to calibrate) and the relation between the value both distributions is deduced. For small amount of discrete states, it is possible to realize a mapping of each of the different values.

### *Kalman filtering*

A data assimilation method to produce complete temporal sequences of synthetic medium-resolution images combining moderate- and medium-resolution imagery is presented in Sedano et al. (2014). Within the framework of a Kalman filter recursive algorithm (Kalman, 1960) also known as linear quadratic estimation, the method integrates models, observations and their respective uncertainties, with partly or fully missing variables, in the calculation of the synthetic images at time steps for which medium-resolution imagery is not available. It therefore allows continuous monitoring of land surfaces at higher spatial resolution than moderate-resolution sensors and higher temporal frequency than existing medium-resolution sensors. To demonstrate the approach, time series of 30-m spatial resolution NDVI images at 16-day time steps were generated using Landsat NDVI images and MODIS NDVI products at four sites with different ecosystems and LC/LU dynamics. The results show that the time series of synthetic NDVI images captured seasonal land surface dynamics and maintained the spatial structure of the landscape at higher spatial resolution. The method provided a robust performance for input data of variable qualities and environmental conditions, highlighting the relevance of including uncertainties in the integration of multi-sensor remote sensing data.

This method was applied on PROBA-V time series. Kempeneers et al. (2016) present a data assimilation method to increase the temporal resolution of the nadir-viewing 100-m product with the off-nadir 300-m images, having identical spectral specifications, in order to produce a continuous 100-m time series. Indeed, the swath of the nadir-viewing sensor is only half of the swath of a single off-nadir viewing sensor. Due to its limited field of view, a global coverage can only be obtained every five days, which is a serious drawback for a number of applications especially in cloud-affected areas. The method implements the Kalman filter recursive algorithm to generate the assimilated imagery at the fine spatial detail (100 m). The assimilated product is a cloud-free time series at the temporal resolution of the 300-m data, while preserving the spatial detail of the fine resolution data. Quantitative results show the potential of the method for continuous monitoring of land surfaces compared to a simple data assimilation and the Savitzky–Golay (SG) filter.

One of the strengths of the Kalman filter is its robustness to a relatively large number of gaps in temporal time series. Especially in the context of data acquisition with optical sensors in conditions with frequent cloud cover, this is an important asset. The added value of the improved spatial resolution from 300 to 100 m has also been illustrated for monitoring agriculture via remote sensing in this area. It was shown that the synthetic profile at 100 m based on the Kalman filter was better able to capture the phenological patterns of the crops with respect to the original PROBA-V product at both 100 and 300 m.

Recently, the Kalman filter method was used for the implementation of the dynamic land cover product at 100 m resolution provided in the Copernicus Global Land Service (Buchhorn et al., 2017). In order to overcome the low data density and therefore data gaps in the PROBA-V 100 m MC5 time series product, PROBA-V 300 m data which has a daily revisit time is fused in via a Kalman filtering for the input of the classification.

### *STARFM and ESTARFM*

PROBA-V 100-m and 300-m S-1 products were also fused in Zheng et al. (2016) in order to map the biomass and yield of winter wheat, this time using the Spatial and Temporal Adaptive Reflectance Fusion

Model (STARFM) (Gao et al., 2006) and later also the Enhanced Spatial and Temporal Adaptive Reflectance Fusion Model (ESTARFM) (Zhu et al., 2010) algorithms.

F. Gao et al. (2006) used the STARFM to obtain images high in both spatial and temporal resolutions, predicting daily surface reflectance data at the Landsat ETM+ spatial resolution and the MODIS temporal resolution. It is one of the first fusion algorithms that has been widely used for synthesizing Landsat and MODIS imageries. The Landsat images can be sparse in time, letting the MODIS data capture temporal changes. The STARFM accurately predicts surface reflectance at an effective resolution close to that of the ETM+. However, the performance depends on the characteristic patch size of the landscape and degrades somewhat when used on extremely heterogeneous fine-grained landscapes (Gao et al., 2006). To overcome STARFM's inaccurate predictions of the surface reflectance over heterogeneous landscapes, the ESTARFM was proposed and has proven to be extremely effective (Zhu et al., 2010).

A synthetic daily PROBA-V 100 m land surface reflectance was generated (Zheng et al., 2016). The results indicated that this fusion had excellent abilities because the blended reflectance was closely correlated with the observed reflectance. It shows the strong potential of using PROBA-V 300 m data to enhance the temporal resolution of PROBA-V 100 m data.

STARFM and ESTARFM are shown to be useful in capturing reflectance changes due to changes in vegetation phenology, which is a key element of seasonal patterns of water and carbon exchanges between land surfaces and the atmosphere. However, they may have problems in mapping disturbance events when land-cover changes are transient and not recorded in at least one of the baseline high-resolution (e.g., Landsat) images. In order to detect the spatial and transient changes, the Spatial and Temporal Adaptive Algorithm for mapping Reflectance Change (STAARCH) was introduced by Hilker et al. (2009) to serve change detection of reflectance values used for Landsat and MODIS. Based on Tasseled Cap transformations of both Landsat and MODIS reflectance data, the algorithm detects vegetation changes and employs each optimal Landsat-MODIS image pair in the fusion process.

### *Bayesian data fusion*

A BDF framework was applied in Fasbender et al. (2009) for the update of scarce high resolution images of a first sensor with time series of coarser images from a second sensor. This BDF framework aims at reconciling various secondary information sources into a unique prediction. Although initially proposed in a spatial prediction context, a generalization of this BDF approach was presented here for space-time predictions. Two methods differing with respect to the amount of information sources at finer resolution were considered for the prediction of the target image. Details are provided by the high resolution image whereas the global fluctuations and seasonal trends are provided by the coarser image. The information relevance of the finer image with respect to the fused one is expected to drop along with the change of seasons. Although they only applied the method to a synthetic case study, generalizations of this BDF method are possible in order to tackle real case applications with images having different spectral bands.

In Fasbender et al. (2009), linear regression is used to reflect the temporal dynamics, which, however, may not hold in a variety of situations. Moreover, there may be no regression-like trends in some cases. Xue et al. (2017) developed a formal and flexible Bayesian framework for the fusion of Landsat and MODIS images to obtain images high in both spatial and temporal resolutions. It provides a formal framework for the spatio-temporal fusion of remotely sensed images with a rigorous statistical basis that enables to efficiently handle uncertainties, it imposes no requirements on the number of input high resolution images, and it is suitable for heterogeneous landscapes. It makes use of the advantage of multivariate arguments in statistics to handle temporal dynamics in a more flexible way rather than just by linear regression. Experimental results demonstrate that the proposed method outperforms STARFM and ESTARFM, especially for heterogeneous landscapes. It produces surface reflectance highly correlated with those of the reference Landsat images.

#### 3.3.1.4 Product-level fusion

To illustrate the fusion at the product-level, three cases of post-classification fusion are presented here.

To update built-up areas of the 2012 European HRL Imperviousness, a large set of images including IRS LISS-3, RE, SPOT-5 and IRS AWiFS time series are available through the ESA Data WareHouse (DWH). These latter are heterogeneous and particularly complex to process all in one as they have very different spectral/spatial resolution and they have been acquired at different time, in different conditions. Lefebvre et al. (2013) propose a robust approach able to combine all DWH products. They perform a separate image classification based on these data and then combine of each classification probabilities using a data fusion technique. The classification step is based on a neural network algorithm and the fusion step is performed with the Dempster-Shafer Theory (DST). This technique relies on evidence theory, it combines multiple classifiers dealing with the imprecision and uncertainty. Results bring out the efficiency of the method to process large projects such as GIO HR Layer and to benefit from the large diversity and availability of the ESA DWH products.

A fusion of Landsat data and MODIS active fire detections product is performed by Boschetti et al. (2015) to map systematically burned areas at 30 m resolution. Spectral changes in time series of Landsat 30m data and temporally and spatially near-coincident daily 1 km MODIS active fire detections are used as separate sources of evidence for the occurrence of fire. A multistage mapping approach is used with an initial per-pixel change detection based on spectral rule-based pre-classification of Landsat 30m time series to identify candidate burned areas. The candidate burned area objects are then either retained or discarded by comparison with contemporaneous MODIS active fire detections, and an object-oriented fusion of the candidate with the MODIS product is performed.

It is a common case that several and partially conflicting land cover products are available at the same time over a same area, where each product suffers from specific limitations and lack of accuracy. In order to take advantage of the best features of each product while at the same time attenuating their respective weaknesses, Gengler and Bogaert (2018) propose a methodology that allows the user to combine these products together based on a general framework involving maximum entropy/minimum divergence principles, BDF and Bayesian updating. First, information brought by each land cover product is coded in terms of inequality constraints so that a first estimation of their quality can be computed based on a maximum entropy/minimum divergence principle. Information from these various land cover products can then be fused afterwards in a Bayesian framework, leading to a single map with an associated measure of uncertainty. Finally, it is shown how the additional information brought by control data can help improving this fused map through a Bayesian updating procedure.

#### 3.3.2 Candidate variables for time-series fusion

The detection of changes in land use and the monitoring of seasonal dynamics can be hampered by various physical effects that affect the signal of the sensor.

Several issues can be mentioned, with varying impacts on the time series building. At the level of the sensor itself, saturation and non-linear response can occur during the capture of the digital count. This digital count for each pixel is also known to be permanently affected by the drift of the radiometric calibration – a familiar problem caused by the slow alteration of the sensor spectral capacities, subjected the short-wave radiation, that carries more energy and are prone to damage the material over time.

At the level of the surface, topographical effects, as detailed in the report D10.1b on WP 32, combined with surface reflectance effects and atmospheric distortion, cause false change detection. Those effects reveal themselves in the shape of shadows over relief that fluctuate from one image to the other, of sun glint over water bodies and wetlands, due to the brief matching of the sun zenith angle and the one of the satellite, or of the presence of aerosols in the lowest layers of the atmosphere that causes light

scattering and absorption. Reflectance on the surface can also be modified by the evolving optical properties of the background soil underneath vegetal cover.

All those factors can significantly produce variations in the raw data from one date to the other – even though a RTM has been applied to produce BOA images. Without in-situ data to support such models and provide measured parameters, the output of the model is still subject to small errors and uncertainties. This is why spectral and textural indices, some of them more or less resistant to such variations, can be used as a substitute for raw spectral band images. It should also be mention that multi-sensor approaches, by handling different spectral and spatial properties of various sensors, benefit from the use of such metrics.

### 3.3.2.1 Spectral variables

Many spectral indices have been defined in the past three decades. Some have been and are still widely used, such as the NDVI, while others have only been proposed as alternatives in the recent years and have not found the same uptake. In Table 3-1, the main spectral indices are listed focusing on vegetation and built-up discrimination in order to explore their potential contribution to the evolution of Copernicus Land Services products and at the same time, favouring indices used in time series studies. The following sections discuss in depth a selected set of optical spectral indices, which are suitable to quantify distinct characteristics of the land surface and which hence are prime candidates for time-series generation to monitor temporal trends.

**Table 3-1: List of spectral indices and their use for the creation of time series in published studies.**

CATEGORY	INDICES	USED IN TSA
VEGETATION INDEX	NDVI (Normalized Difference Vegetation Index)	✓
VEGETATION INDEX	DVI (Difference Vegetation Index)	✓
VEGETATION INDEX	RVI (Ratio Vegetation Index)	✓
VEGETATION INDEX	IRECI (Inverted Red Edge Chlorophyll Index)	✓
SPECTRAL INDEX	BI (Brightness Index)	-
ARTIFICIAL AREAS INDEX	NDBI (Normalized Difference Built-Up Index)	✓
ARTIFICIAL AREAS INDEX	UI (Urban Index)	-
ARTIFICIAL AREAS INDEX	BUI (Built-Up Index)	✓
ARTIFICIAL AREAS INDEX	IBI (Index-based Built-Up Index)	✓
ARTIFICIAL AREAS INDEX	NBI (New Built-Up Index)	✓
ARTIFICIAL AREAS INDEX	EBBI (Enhanced Built-Up and Bareness Index)	-
ARTIFICIAL AREAS INDEX	NBUI (New Built-Up Index)	✓
HYDRIC STRESS INDEX	NDWI (Normalized Difference Water Index)	✓
HYDRIC STRESS INDEX	MNDWI (Modified Normalized Difference Water Index)	✓
HYDRIC STRESS INDEX	MSI (Moisture Stress Index)	✓
SOIL INFLUENCE INDEX	PVI (Perpendicular Vegetation Index)	-
SOIL INFLUENCE INDEX	SAVI (Soil-Adjusted Vegetation Index)	✓
SOIL INFLUENCE INDEX	TSAVI (Transformed Soil-Adjusted Vegetation Index)	✓
SOIL INFLUENCE INDEX	MSAVI (Modified Soil-Adjusted Vegetation Index)	✓
VEGETATION INDEX	NDMIR (Normalized Difference Middle Infrared Index)	✓
VEGETATION INDEX	NDRB (Normalized Difference Red Blue)	✓
VEGETATION INDEX	NDGB (Normalized Difference Green Blue)	✓
BIOPHYSICAL INDEX	LAI (Leaf Area Index)	✓
SOIL AND ATMOSPHERE	EVI (Enhanced Vegetation Index)	✓
ATMOSPHERE EFFECTS	ARVI (Atmospherically Resistant Vegetation Index)	✓
ATMOSPHERE EFFECTS	GEMI (Global Environment Monitoring Index)	✓
VEGETATION INDEX	TDVI (Transformed Difference Vegetation Index or TDVI)	✓
BIOPHYSICAL INDEX	FCover	✓
BIOPHYSICAL INDEX	fAPAR	✓

*Normalized Difference Vegetation Index or NDVI*

Healthy plants are mainly green, thus absorbing sun radiation in the visible spectrum region called photosynthetically active radiation (PAR), which contains the perfect amount of energy to induce a photosynthesis reaction. Infrared light is not used as an energy source for photosynthesis and is largely reflected by the structural leaf tissue. This is why plant reflects most of the IR wavelengths, while appearing dark in those bands - which is known as the 'red edge' effect.

The NDVI (Rouse Jr. et al., 1974; Tucker, 1979) is used as an indicator to monitor vegetation health, and can be used as a proxy for photosynthetic activity and primary production from vegetation biomass. It is calculated as the difference in the reflectance between those two spectral regions, normalized by the sum of the reflectance measurements:

$$NDVI = \frac{\rho_{NIR} - \rho_{Red}}{\rho_{NIR} + \rho_{Red}}$$

It is then expected for the NDVI to vary between -1 and 1, where:

- dense vegetation canopy exhibits values between 0.9 and 0.6;
- shrubs, grasslands or senescing crops gives smaller values, between 0.5 and 0.2;
- soils, such as barren rocks, sand or snow, are characterized by small positive values, usually between 0.1 and 0.2;
- deep water and clouds yield negative values.

Since the clouds exhibit NDVI values below zero, the NDVI can provide helpful information for cloud screening. This index is one of the oldest and most used means to map vegetation (or non-vegetation) presence on the ground.

The first limitation of the NDVI lays in the fact that by mathematical construction, it carries less information than both spectral channels used to compute its value. In particular, this design, with its compression of the high ratio values, is linked to the well-known and problematic saturation of the NDVI for dense canopies, which always leads to an underestimation of the green biomass for strong foliage density (Wang et al., 2005). Several other factors have been pointed as responsible in part for this loss of information, such as the width of the red band. The non-linearity of such a ratio also results in a non-linear relation with other vegetation indices, directly linked to the amount of vegetation present in the area of interest (AOI), among which, the fAPAR or the LAI are found.

The NDVI is also known to be sensitive to atmospheric effects, in particular to the presence of aerosols and water vapour, producing a degradation of contrast between the two spectral channels, but also to the conditions of observation, for example the absorption and the scattering occurring along the atmospheric path. The difference between the spectral response of two sensors yields different values of the NDVI over the same AOI, at the exact same date, making it harder to compare time series. However, the creation of composite images of NDVI is able to improve the resulting time series, with the minimization of anisotropic effects.

Several factors on the ground can degrade the interpretability of the NDVI. The inclination of the leaves modifies the BRDF and thus the ratio – the plainer the leaves, the stronger the signal of the NDVI, while their shadows artificially decrease its value. The soil underneath the foliage, depending on its brightness, its colour and its degree of moisture, or even the distribution of greenness on it (i.e. the same amount of vegetation covering the ground, but disposed in a different fashion) can have a significant impact on the NDVI values.

The NDVI is widely used to detect the presence of vegetation and its state; however, the derivation of biophysical parameters can be hampered by the outlined inter-dependences.

### *Difference Vegetation Index or DVI*

The DVI (Richardson & Wiegand, 1977) was proposed before the NDVI and, as its name indicates, it is only the difference characterizing the red edge, without normalization. It is also known as the Environment Vegetation Index (EVI). It can be calculated with:

$$DVI = \rho_{NIR} - \rho_{Red}$$

Even though the DVI is not a normalized quantity, once directional effects are corrected (using in particular bidirectional anisotropy standard shapes and reflectance correction) and for water vapour absorption, the DVI is more robust than NDVI to atmospheric effects and noise in general (Bacour et al., 2006).

However, the DVI still exhibits similar limitations to the NDVI ones, due to its close mathematical construction. In fact, the DVI remains sensitive to several key parameters, in particular, the presence of aerosol in the atmosphere, and the resulting scattering of the radiation. The geometry of the

observation, mainly presenting a solar zenithal angle higher than 60° can lead to disparaging results – this is specifically an issue for old sensors, which are subject to orbital drift effects.

Overall, it should be noted that like the NDVI, the DVI cannot be used as a tool to quantitatively estimate the state of vegetation when the vegetation is canopy is too dense.

### *Ratio Vegetation Index or RVI*

Also called Simple Ratio (SR), the ratio vegetation index (Jordan, 1969) is defined by:

$$RVI = \frac{\rho_{NIR}}{\rho_{Red}} \text{ or } RVI = \frac{\rho_{NIR}}{\rho_{Vis}}$$

where the red channel is replaced by the visible channel if it is not available. RVI for bare soils are near 1, its value increases as the amount of green vegetation in an AOI. The ratio is not bound and can increase far beyond 1.

By design, the RVI is less sensitive to topographical and atmospheric effects when the vegetation coverage is dense; it is due to the fact that the equation eliminates irradiance and transmittance values in both channels. Unlike the NDVI and the DVI, a good correlation exists between the plant biomass present in the AOI and the RVI values.

Yet those improvements remain limited. Sensitivity to the spectral contribution of the soil, to the geometry of the observation, in particular the sun illumination angle, cannot be eliminated from the computation of the RVI. When the vegetation is sparse (i.e. covering less than 50% of the observed AOI), the RVI also needs to be atmospherically corrected.

### *Inverted Red Edge Chlorophyll Index or IRECI*

The IRECI was introduced by (Frampton et al., 2013) to evaluate the capability of the S-2 sensor for the estimation of canopy chlorophyll content. It utilizes the maximum and minimum vegetation reflectances in the RED EDGE 3 (proposed NDVI band adjusted to S-2 wavelength specifications) and RED bands and the leaf chlorophyll concentration indicative RED EDGE slope. The incorporation of the Red Edge bands also limits the effects of saturation. Although not the initial aim of the development, the IRECI index showed a strong linear correlation with the biophysical Leaf Area Index (LAI) parameter.

$$\frac{\rho_{Red\ Edge\ 3} - \rho_{Red}}{\rho_{Red\ Edge\ 1} / \rho_{Red\ Edge\ 2}}$$

### *Brightness Index*

The brightness Index (BI) can expressed as (Mathieu et al., 1998):

$$BI = \sqrt{\frac{\rho_{Red} + \rho_{Green} + \rho_{Blue}}{3}}$$

which is a measure of the average reflectance magnitude in the visible bands, used to quantify the soil color effect.

### *Normalized Difference Built-Up Index or NDBI*

The “Normalized Difference Built-Up Index” (Zha et al., 2003) is defined as:

$$NDBI = \frac{\rho_{SWIR} - \rho_{NIR}}{\rho_{SWIR} + \rho_{NIR}}$$

This index highlights urban areas, where the SWIR radiations are more reflected than the NIR ones. It has been originally developed for Landsat TM bands 4 and 5 and it will work with any multi-spectral instrument with a NIR band between 0.76 - 0.9  $\mu\text{m}$  and a SWIR band between 1.55 – 1.75  $\mu\text{m}$ . The NDBI determination does not rely on seasonality consideration and should not be impacted by the date of the image; however, it remains best to put an emphasis on image acquired at times when the vegetation cover is at its peak, like for any vegetation indices. The use of a different spectral channel, the SWIR band, in the equation of the NDBI makes it independent yet complementary to the NDVI, and they both can be used together.

The NDBI does not distinguish the different parts constituting the urban tissue, for example, residential land cover will exhibit the same NDBI as highly industrial areas. This is why the NDBI is mainly used to map wide urban land cover, requiring few details. It should also be noted that the NDBI confuses barren lands, such as sandy beaches, agricultural areas subjected to drought, due to the loss of moisture in the soil, with urban zones. This confusion between beaches and urban areas can be circumvented by assessing the closeness to water bodies; however, peripheral urban zones mixed with barren soils will be less simply discriminated using this index.

#### *Urban Index or UI*

The Urban Index (Kawamura et al., 1996) is defined as:

$$UI = \left( \frac{\rho_{SWIR\_2} - \rho_{NIR}}{\rho_{SWIR\_2} + \rho_{NIR}} + 1 \right) * 100$$

where  $\rho_{SWIR\_2}$  is the SWIR band with wavelengths ranging from 2.08  $\mu\text{m}$  and 2.35  $\mu\text{m}$ , matching the band 7 of Landsat TM. The UI exploits an observed inverse relation between the brightness of built-up lands in the NIR and SWIR bands.

While on one hand, the UI cannot distinguish between barren lands and built-up areas; this can be improved by combining it with an automatic segmentation method.

#### *Built-Up Index or BUI*

The Built-Up Index, in order to separate the barren lands from the urban sprawl (Kaimaris & Patias, 2016), is defined by:

$$BUI = \frac{2 * ((\rho_{Red} * \rho_{SWIR\_2}) - (\rho_{SWIR\_1} * \rho_{SWIR\_1}))}{(\rho_{Red} + \rho_{SWIR\_1}) * (\rho_{SWIR\_1} + \rho_{SWIR\_2})}$$

where SWIR\_1 matches the band 5 of Landsat TM, which ranges from 1.55  $\mu\text{m}$  to 1.75  $\mu\text{m}$ , SWIR\_2 tallies with the band 7, from 2.09  $\mu\text{m}$  to 2.35  $\mu\text{m}$ .

In their article, Kaimaris and Patias showed that the built-up index identifies areas without constructions with a better accuracy than NBI, UI, NDBI, IBI and EBBI, due to the fact that the CART does not take into account the contribution of the spectral band in the near infrared, which leads to a reduced overall accuracy to identify constructions. However, the test has only been realised at the scale of a city.

**Index-based Built-Up Index or IBI**

The Index-based Built-Up Index (Xu, 2008) is the first urban index based on other indices results, rather than the raw data of the images spectral bands. It is defined as:

$$IBI = \frac{\left( NDBI - (SAVI + MNDWI)/2 \right)}{\left( NDBI + (SAVI + MNDWI)/2 \right)} = \frac{2 * \rho_{SWIR}}{(\rho_{SWIR} + \rho_{NIR})} - \left[ \frac{\rho_{NIR}}{(\rho_{NIR} + \rho_{Red})} + \frac{\rho_{Green}}{(\rho_{Green} + \rho_{SWIR})} \right]$$

$$\frac{2 * \rho_{SWIR}}{(\rho_{SWIR} + \rho_{NIR})} + \left[ \frac{\rho_{NIR}}{(\rho_{NIR} + \rho_{Red})} + \frac{\rho_{Green}}{(\rho_{Green} + \rho_{SWIR})} \right]$$

then later refined (Ray, 1994) as:

$$IBI = \begin{cases} \frac{(NDBI - (SAVI + MNDWI)/2)}{(NDBI + (SAVI + MNDWI)/2)}, & \text{if the plant cover is } < 30\% \\ \frac{(NDBI - (NDVI + MNDWI)/2)}{(NDBI + (NDVI + MNDWI)/2)}, & \text{if the plant cover is } > 30\% \end{cases}$$

The three indices represent the three main components of urban environments: vegetation, water and built-up land. The values range from -1 to 1, where null or negative values are generated by background noise, such as water and vegetation.

The IBI is constructed to suppress background noises and to clearly separate the diverse land cover or land use classes, in particular to detect asphalt and concrete surfaces. Yet compared to simple indices such as the NDVI, the IBI requires either a complex computation composed of four spectral bands or the computation of four different indices.

**New Built-Up Index or NBI**

The Built-Up Index (Jieli et al., 2010) is defined by:

$$NBI = \frac{2 * (\rho_{Red} * \rho_{SWIR\_1mu})}{\rho_{NIR}}$$

It should be noted that the NBI is only able to highlight built-up areas, not to separate water bodies or forest from mixed agriculture. Moreover, this index is not a dimensionless quantity, and therefore is dependent on the sensor – time series of maps generated with it, but issued from different satellites cannot be compared between each other.

**Enhanced Built-Up and Bareness Index or EBBI**

The Enhanced Built-Up and Bareness Index (As-Syakur et al., 2012) is defined by:

$$EBBI = \frac{\rho_{SWIR\_1\mu} - \rho_{NIR}}{10 \sqrt{\rho_{SWIR\_1\mu} - \rho_{TIR}}}$$

It relies on 3 channels, in order to highlight contrast reflection range and absorption in built-up and bare land areas. The Thermal InfraRed (TIR) wavelengths are used to map high and low levels of albedo in urban areas. The high emissivity in urban areas is caused by the type of material found in those, while the emissivity of bare soil is determined by the degree of moisture and the presence of mineral constituents.

The positive values are associated with built-up and barren land pixels, while the presence of vegetation generates negative values, roughly varying between -1 and 1. The TIR channel is also sensitive to the higher temperature radiation emitted by the urban areas.

The EBBI has been specially constructed to distinguish between barren soils and built-up lands. Based on the work of As-Syakur et al. (2012), it shows an increased accuracy to determine the percentage of surface covered by built-up structures, but its relative accuracy may be lower than other indices, specifically designed to target only one type of land covers, which is to be expected in highly heterogeneous landscapes. This index also has the advantage to eliminate artefacts produced by the shadows or the water bodies' presence.

#### *New Built-Up Index or NBUI*

The New Built-Up Index (Sinha et al., 2016) is defined by the combination of 3 other indices:

$$NBUI = EBBI - (SAVI + MNDWI)$$

$$NBUI = \frac{\rho_{SWIR\_1\mu} - \rho_{NIR}}{10 \sqrt{\rho_{SWIR\_1\mu} - \rho_{TIR}}} - \left( + \frac{\rho_{Green} - \rho_{SWIR}}{\rho_{Green} + \rho_{SWIR}} \right)$$

The use of EBBI highlights the contrast reflection between built-up and barren lands, while the second part uses SAVI to signal the presence of vegetation, instead of NDVI, which remains less effective in an area with low plant cover. The final part, the MNDWI, is used to map the presence of water. This leads to positive values for built-up and barren lands, while water and vegetation yield negative values. This index has shown a better accuracy to map urban areas than NDBI or UI, taken alone, as demonstrated in the works of Sinha et al. (2016).

#### *Normalized Difference Water Index or NDWI*

The “Normalized Difference Water Index” (Gao, 1996) is defined as the ratio

$$NDWI = \frac{\rho_{NIR} - \rho_{SWIR}}{\rho_{NIR} + \rho_{SWIR}}$$

where  $\rho$  is the radiance in reflectance unit. Both wavelengths are localized in the part of the spectrum reflected by vegetation canopies. The NIR channel is linked to a negligible absorption of light by the water content present in the vegetal, while the SWIR channel present a weak liquid absorption. The NDWI is therefore sensitive to slight changes in the liquid water absorbed by vegetation canopies, giving an indication on the vegetation water stress.

The NDWI is the opposite of the NDBI in theory, but other set of bands in the SWIR and NIR are often used. The NDWI is therefore also independent yet complementary to the NDVI. Compared to the latter, the NDWI is less sensitive to the atmospheric effects, in particular to the presence of water vapour in the atmospheric column. While the NDVI is linked to vegetation greenness and the presence of chlorophyll in

the plants, it is not directly to the quantity of water in them, contrary to NDWI. The soil background has a non-negligible effect on the values of this index when the vegetal cover at the surface is only partial. Drought and water stress are not the only factors responsible for land cover changes, pest and diseases can alter the vegetal cover; the NDWI should be used with other vegetation indices.

#### *Modified Normalized Difference Water Index or MNDWI*

Another derived index is the “Modified Normalized Difference Water Index” (MNDWI) (Xu, 2006) which focuses on extracting water presence from background dominated by built-up land:

$$MNDWI = \frac{\rho_{Green} - \rho_{SWIR}}{\rho_{Green} + \rho_{SWIR}}$$

where  $\rho_{Green}$  is the reflectance of a green band between 0.5 - 0.6  $\mu\text{m}$  and  $\rho_{SWIR}$  a band between 1.55 – 1.75  $\mu\text{m}$ . The water bodies are expected to be more finely delineated by this index, using a proper thresholding value – thanks to an improved discrimination between open surface water and the noise emerging from the built-up areas, the moisture present in the vegetation and soil.

#### *Moisture Stress Index or MSI*

In order to track the amount of water in the vegetation, and in particular the leaves, it is possible to switch the red band for a band in the mid-infrared. Based on the model of the RVI, a new index (Hunt & Rock, 1989) can be defined as:

$$MSI = \frac{\rho_{MIR}}{\rho_{NIR}}$$

This index is used to monitor canopy stress, to predict productivity of crop fields and to study biophysical modeling. The interpretation of the MSI is inverted, compared to the other water indices: the high values indicate a greater water stress in the foliage. The variation ranges from 0 to 3, and common values for a healthy green vegetation is comprised between 0 and 2.

#### *Perpendicular Vegetation Index or PVI*

In order to take into account the influence of the soil underneath the vegetation, this index is computed in the feature space between the NIR band and the red one (Richardson & Wiegand, 1977). Each pixel of an image can be placed in a graph called feature space graph using its radiation reflected luminance in the red band and its radiation reflected luminance in the NIR band as coordinates. Using this visualization in the red, NIR 2D space, it is possible to spot isolated groups of pixels that may be related.

The soil line is the line defined by a slash called the soil brighten line, and the PVI is taken equal to the perpendicular distance from this line to the point representing the pixel. Each pixel of equal vegetation density cover is supposed to be found along parallel lines to this soil line, which are called vegetation isolines. The greater the distance to the soil line, the greater the vegetation biomass. The PVI can then be computed from the equation:

$$PVI = \sqrt{(\rho_{soil} - \rho_{veg})_{Red}^2 + (\rho_{soil} - \rho_{veg})_{NIR}^2}$$

where  $\rho_{soil}$  is the soil reflectance and  $\rho_{veg}$  is the vegetation reflectivity.

The main advantage of the PVI lays in its ability to filter out the undesired influence of the soil background in an effective manner; moreover, it exhibits also less sensitivity to the atmospheric effects.

This is why the PVI is often preferred to the NDVI for the inversion of surface vegetation parameter (grass yield, chlorophyll content) or the computation of the LAI.

Nonetheless, the PVI remains sensitive to soil brightness and soil reflectivity, in particular in the presence of sparse vegetation coverage, and therefore needs to be adjusted for each kind of couple (soil type, percentage of vegetation coverage).

#### *Soil-Adjusted Vegetation Index or SAVI*

In order to improve even more the way soil is being considered in the PVI, Huete (1988) proposed to include the nature of the background as a parameter, leading to:

$$SAVI = \frac{(\rho_{NIR} - \rho_{Red})(1 + L)}{\rho_{NIR} + \rho_{Red} + L}$$

where  $L$  is called the soil conditioning index. The values of  $L$  are fixed according to the specific environmental conditions, from 1 to 0. When the vegetation cover is dense, in the case of large canopies mainly,  $L$  has a value near 0.25, while for areas devoid of green vegetation,  $L$  is set to 1. Under most environmental conditions,  $L$  is close to 0.5 and when it is near 0, the value of SAVI nears the one of the NDVI. SAVI values range from -1 to 1: the lower this value, the lower the amount of green vegetation.

One of the most key features of the SAVI lays in its ability to be more robust than the NDVI without requiring atmospheric corrections, and, as a consequence, to be even more accurate with the use of those corrections. On the other hand, this accuracy depends upon the specification of a soil brightness correction factor, which is a function of the kind of land cover present in the image – thus changing for each considered landscape.

#### *Transformed Soil-Adjusted Vegetation Index or TSAVI*

An improvement of the SAVI, called TSAVI, has been constructed (Baret et al., 1989) using the determination of the soil line for the considered sensor, modeled by a slope  $a$  and an intercept of the soil line  $b$ :

$$TSAVI = \frac{a * (\rho_{NIR} - a * \rho_{Red} - b)}{\rho_{NIR} + \rho_{Red} - a * b + 0.08 * (1 + a^2)}$$

where the coefficient value 0.08 has been adjusted to minimize soil effects.

The TSAVI uses the slope  $a$  and the intercept of the soil line  $b$  instead of an arbitrary parameter like the soil conditioning index  $L$ , which is an advantage to better retrieve information, but also a limitation, as it needs a function depending on the kind of land cover present in the image.

#### *Modified Soil-Adjusted Vegetation Index or MSAVI*

Another improvement proposed for the SAVI is the MSAVI, based on other local indices (Qi et al., 1994), rendering the parameter  $L$  dynamically adjusted using the image data:

$$MSAVI = \frac{(\rho_{NIR} - \rho_{Red})(1 + L)}{\rho_{NIR} + \rho_{Red} + L}, \text{ with } L = 1 - 2 * a * NDVI * WDV$$

where  $a$  is the slope of the soil line and  $WDVI = \rho_{NIR} - a * \rho_{Red}$  is the Weighted Difference Vegetation of Clevers, functionally equivalent to the PVI. To correct the soil brightness, the MSAVI loses overall sensitivity to changes in vegetation cover, unlike NDVI, which thus remains a more appropriate

tool to detect changes. It should also be added that the MSAVI is more sensitive to the atmospheric conditions between different AOI and/or taken at different times.

#### ***Normalized Difference Middle Infrared Index or NDMIR***

The Normalized Difference Middle Infrared Index (NDMIR) has been originally proposed by Lu et al. (2004) for Landsat TM data and is a normalised difference of both middle infrared bands:

$$NDMIR = \frac{\rho_{MIR1} - \rho_{MIR2}}{\rho_{MIR1} + \rho_{MIR2}}$$

Thus, it is sensitive to vegetation moisture. However, change in forest volume has been identified in many studies of being revealed best by middle infrared wavelengths and also Lu et al. (2004) showed that the NDMIR significantly correlated with forest stand parameters.

#### ***Normalized Difference Red Blue or NDRB***

The Normalized Difference Red Blue Index (Zhou et al., 2014) has been designed based on the red and blue bands of Landsat-8 OLI data:

$$NDRB = \frac{\rho_{RED} - \rho_{BLUE}}{\rho_{RED} + \rho_{BLUE}}$$

It has been introduced to better discriminate red/grey-roofed built-up from bare land areas (Zhou et al., 2014).

#### ***Normalized Difference Green Blue or NDGB***

The Normalized Difference Green Blue Index (Zhou et al., 2014) has been designed based on the red and blue bands of Landsat-8 OLI data:

$$NDGB = \frac{\rho_{GREEN} - \rho_{BLUE}}{\rho_{GREEN} + \rho_{BLUE}}$$

Similar to the NDRB, the NDGB has been introduced to better extract the blue-roofed built-up areas and part of the red/grey-roofed built-up areas (Zhou et al., 2014). Combined with the NDRB it was used to discriminate built-up areas and bare soil and achieved better results than with the standard NDBI approach.

#### ***Leaf Area Index or LAI***

The “Leaf Area Index” (Turner et al., 1999) is used to characterize plant canopies and determine the size of the interface for the exchange of energy (including mainly radiation) and mass between the canopy and the atmosphere. It is defined as the green leaf area per unit of ground surface for broadleaf trees, and concerning conifers, there have been several proposed definitions:

- Either the total needle surface per unit of ground surface area, divided by two;
- Either the projected needle surface per unit of ground surface area;
- Or the total needle surface per unit of ground surface area.

The leaf area index can range from 0 for barren lands to 10, for dense canopies and is used to estimate leaves cover and to forecast crop yield, but also examine relationships between environmental stress factors and forest insect damages. It remains strongly non-linear with reflectance, scale-dependent and not accessible directly from remote sensing observations, which are sensitive to the ‘effective’ LAI, a

fraction of the ‘true’ LAI. The LAI can theoretically be retrieved with physical models, but some assumptions on the distribution of leaves have to be made, and cannot be applied for all types of vegetation.

One of the ways to determine the LAI in-situ involves the measurements of a foliage sample – which is a destructive method. The true LAI is difficult to acquire from remote sensing images, for numerous reasons, e.g. the effect of branches and stems blocking the light – and the validation of this product using in-situ data can prove to be difficult.

### *Enhanced Vegetation Index or EVI*

The “Enhanced Vegetation Index” (Liu & Huete, 1995) is defined by the following equation:

$$EVI = Gain * \frac{(\rho_{NIR} - \rho_{Red})}{(\rho_{NIR} + C_1 * \rho_{Red} - C_2 * \rho_{Blue} + L)}$$

where the numerical parameters *Gain*,  $C_1$ ,  $C_2$  - both weights related to the aerosol conditions in the blue and red bands - and  $L$  - a canopy background adjustment term - need to be adapted for each sensor and each situation. The main feature of the EVI is to incorporate background corrective term as well as atmospheric resistance concepts, therefore  $\rho$  is the “apparent” reflectance, at the top of the atmosphere, that requires no further calibration – which means in return that  $C_1$  and  $C_2$  depend on the atmospheric conditions, while  $L$  depends on the kind of vegetation present on the image – thus forcing the EVI to require an empirical tuning for each AOI.

### *Atmospherically Resistant Vegetation Index or ARVI*

This index is based on the knowledge that the red band is significantly impacted by the atmospheric effects, more than the NIR band (Kaufman & Tanre, 1992). Thus, the red band value is replaced by a difference between the blue and the red bands value, taking into account the (Rayleigh) molecular scattering and gaseous absorption for ozone corrections. The ARVI is expressed as:

$$ARVI = \frac{\rho_{NIR} - \rho_{RB}}{\rho_{NIR} + \rho_{RB}}, \text{ with } \rho_{RB} = \rho_{Red} - \gamma * (\rho_{Red} - \rho_{Blue})$$

where  $\gamma$  depends on the aerosol type – which can be set to 1 if the aerosol model is unknown, presenting thus no change with the NDVI.

The ARVI is based on a reformulation of the NDVI designed to eliminate the effects of atmospheric aerosols and the ozone absorption, and this improved version of the NDVI, with this atmospheric resistance concept, can be incorporated into other indices, such as SAVI, to form a soil and atmospherically resistant vegetation index or SARVI; however, soil and atmosphere influence are interactive, and the removal of one source of noise increased the presence of the other. The main constraint of the ARVI lays in the fact that it should be computed with an aerosol model, and without one, it remains no better than NDVI. Therefore, one needs in-situ data on the actual atmospheric conditions, varying for each given time of the temporal series and each considered AOI.

### *Global Environment Monitoring Index or GEMI*

In order to minimize the influence of atmosphere on the computation of index, such as the Rayleigh scattering, the GEMI (Pinty & Verstraete, 1992) is a non-linear index, defined as:

$$GEMI = \eta * (1 - 0.25 * \eta) - \frac{\rho_{Red} - 0.25}{1 - \rho_{Red}}, \text{ with } \eta = \frac{2(\rho_{NIR}^2 + \rho_{Red}^2) + 1.5\rho_{NIR} + 0.5\rho_{Red}}{\rho_{NIR} + \rho_{Red} + 0.5}$$

which varies from 0 to 1 over continental areas.

The GEMI, like the NDVI, involves only two spectral channels to be computed, and has been designed to be resistant to atmospheric conditions, leading to an almost linear relationship between the GEMI computed without atmospheric corrections, computed at the top of the atmosphere, and the pre-processed GEMI, obtained at the bottom of the atmosphere. On a given AOI, the GEMI has the disadvantage to be highly sensitive to soil noise, and is unable to deal with variations in soil reflectance – therefore being unsuitable for the creation of time series over arid regions.

#### *Transformed Difference Vegetation Index or TDVI*

The Transformed Difference Vegetation Index (Bannari et al., 2002) has been theorized to be an improvement of the NDVI and the SAVI, by having a linear function of the vegetal canopy, while being resistant to the optical properties of the bare soil:

$$TDVI = \sqrt{0.5 + NDVI} = \sqrt{0.5 + \frac{\rho_{NIR} - \rho_{Red}}{\rho_{NIR} + \rho_{Red}}}$$

The TDVI does not saturate like NDVI and SAVI for high values and exhibit a linear behaviour as function of the amount of vegetation cover. However, like the NDVI or the SAVI, the TDVI requires calibrated images to perform better than both indices, in particular to avoid the impact of atmospheric effects.

#### *Fractional Cover or FCover*

FCover is the estimated fraction of green vegetation that covers the soil, as seen from the nadir (Carlson & Ripley, 1997). It used to quantify the surface occupied by vegetation, giving an indication of the crop growth rate. Several methods can be employed to determine its value for a given image, among which:

- Conventional classification, using supervised or unsupervised algorithms
- Linear modelling, correlating field-measured fractional cover with sensor reflectance bands or vegetation indices
- Physical models, that simulates how the light energy is reflected or absorbed by the different surfaces and can derive an estimation of the FCover, based on the LAI and other structural canopy variables

When the FCover is numerically computed using physical models, its determination requires a precise description and/or group of assumptions on the BRDF: it is mostly done on high-resolution images, over small AOI.

#### *Fraction of Absorbed Photosynthetically Active Radiation or fAPAR*

The fAPAR is the fraction of photosynthetically active radiation absorbed by the green parts of the canopy. It depends on the canopy structure, on the vegetation element optical properties and the illumination conditions. The major methods to generate the fAPAR are mainly simulations, such as linear modeling interpolation or physical models.

The fAPAR excludes the fraction of incident PAR that is reflected by the leaves and absorbed by the soil, as well as the fraction directly absorbed by the soil. It remains difficult to measure directly, and is usually computed by numerical radiative transfer models, like the LAI and the FCover, for given assumptions on the canopy structure.

The fAPAR values prove to be relatively linear related to the reflectance values, but depend on the chosen scale, which can be an issue as the fAPAR is routinely used as a key variable to forecast crop yield (Prince & Goward, 1995) and to monitor forest health. Estimations of the fAPAR are excessively sensitive to the presence of snow in the background.

### Conclusion

Despite presenting some drawbacks, the NDVI is still widely in use, largely because of its computation in well-calibrated enduring time-series, like the NOAA-AVHRR data set or the Landsat one, spanning over several decades, thus easing the analysis of LC/LU evolution. It remains an one of the most important variables in the creation and analysis of time series, not only to classify new time series of images, but also to compare the results to other studies. The same can be said for the NDBI and the BI, and it is proposed here to use the first two indices first jointly to characterize the imperviousness layer. Other interesting indices have also been tested to better characterize the LC/LU and in particular the forest and agriculture. The NDMIR complements the NDVI to better distinguish vegetation over low water content, whose spectral response can be mistaken as urban areas while using the NDVI. The MNDWI is of help to better discriminate the water bodies and wetlands, and is used when the NDWI accuracy is deemed not sufficient. The IRECI, specifically designed to take advantage of the red edge bands available in S-2 data, can be used to evaluate the canopy chlorophyll content, while being linked to the LAI. The NDRB and NDGB are used to enhance the discrimination between urban areas and bare soils or bare rocks.

#### 3.3.2.2 Textural variables

Spectral indices allow the exploration of spectral correlation, but without further analysis, valuable information inherent in the spatial correlation existing between adjacent pixels is neglected. Several techniques, quantifying either the overall spatial repartition of pixel intensity (the so-called spatial-frequency index) or the special correlation between a distinctive group of pixels (designated as textural indices), can be listed, as seen in the Table 3-2. Integrating such texture measures into the temporal domain can help create more robust time-series, because it allows to monitor the joint behavior of neighboring pixels, which may be a more robust measure to separate noise from actual changes in LC. Textural variables may be derived from both optical and SAR data and can hence contribute to the joint use of both.

**Table 3-2: List of textural indices and their use in the creation of time series.**

CATEGORY	INDICES	USED IN TIME SERIES
TEXTURAL INDEX	GLCM/GLCH	√
TEXTURAL INDEX	PanTex	√
SPATIAL-FREQUENCY INDEX	FT	√
SPATIAL-FREQUENCY INDEX	WT	√

### Co-occurrence matrix

The computation of co-occurrence matrices is a widely used method to extract texture features, where an image texture is defined as an arrangement of intensities (a pattern) that can be repetitively found at various scales in an image. This method is able to capture the similarity in the gray tones of those patterns and the spatial relations between them.

A co-occurrence matrix or distribution (Haralick et al., 1973) is a matrix  $C$  defined over an image to be the descriptor of the state of two pixels simultaneously considered, therefore characterized by a distance  $d$  and an orientation  $\theta$  or an offset in each direction, for example  $(\Delta x, \Delta y)$ . For an image  $I$  of  $N$  pixels, of size  $n * m$ , the co-occurrence matrix  $C$  can be written as:

$$C = \begin{bmatrix} p(1,1) & p(1,2) & p(1,3) & \dots & p(1,N) \\ p(2,1) & p(2,2) & p(2,3) & \dots & p(2,N) \\ p(i,1) & p(i,2) & p(i,3) & \dots & p(i,N) \\ \vdots & \vdots & \vdots & \ddots & \vdots \\ p(N,1) & p(N,2) & p(N,3) & \dots & p(N,N) \end{bmatrix}$$

where  $(i, j)$  are pixel values and  $I(x, y)$  is the value of the pixel at  $(x, y)$ . Several texture measures can be derived from this matrix:

- The uniformity or energy:

$$UNI = \sum_{i=0}^{N-1} \sum_{j=0}^{N-1} p^2(i, j)$$

- The contrast:

$$CONT = \sum_{i=0}^{N-1} \sum_{j=0}^{N-1} |i - j|^k * p(i, j)^2$$

- The maximum probability:

$$MAX = \max_{i,j} p(i, j)$$

- The correlation:

$$CORR = \sum_{i=0}^{N-1} \sum_{j=0}^{N-1} \left[ \frac{(i - \mu) * (j - \mu) * p(i, j)}{\sigma^2} \right]$$

- The entropy:

$$ENT = \sum_{i=0}^{N-1} \sum_{j=0}^{N-1} p(i, j) * \log(p(i, j))$$

- The inverse difference moment:

$$INV = \sum_{i=0}^{N-1} \sum_{\substack{j=0 \\ j \neq i}}^{N-1} \frac{p(i, j)^2}{|i - j|^k}$$

- The angular second moment:

$$ASM = \sum_{i=0}^{N-1} \sum_{j=0}^{N-1} p(i, j)^2$$

- The homogeneity:

$$HOM = \sum_{i=0}^{N-1} \sum_{j=0}^{N-1} \left[ \frac{p(i,j)}{1 + |i-j|} \right]$$

- The dissimilarity:

$$DISS = \sum_{i=0}^{N-1} \sum_{j=0}^{N-1} p(i,j) * |i-j|$$

Co-occurrence matrices are also referred to as gray-level co-occurrence matrices (GLCMs), as gray-level co-occurrence histograms (GLCHs), or as spatial dependencies matrices. The computation can be done in the entire image or in a reduced window for a particular analysis. The co-occurrence matrices are well adapted to describe natural textures, e.g., grassland or cultivated fields. Those matrices are widely used in remote sensing analysis in order to distinguish patterns resulting from anisotropy.

Nonetheless, their handling necessitates the set-up of multiple parameters such as the direction offset, the size of the analysis window or even the choice of one or several metrics described by (Haralick et al., 1973). Depending on the size of the analysis window, bigger or smaller patterns will be detected; the accuracy of the classification procedure thus strongly depending on the values of this particular parameter. Moreover, the temporal evolution of a local texture, based on its size, can be difficult to interpret.

### *PanTex*

The procedure for the calculation of a texture-derived built-up presence index, shortened by PanTex (Pesaresi et al., 2008), is based on fuzzy rule-based composition of anisotropic measures derived from co-occurrence matrix applied to the image. Instead of using spectral signature produced by physical-chemical properties, the PanTex exploits stable structural traits producing local contrast, which can be enhanced by rotation-invariant anisotropic textural analysis based on GLCM measures.

The workflow of the processing chain can be summed up in the following steps:

- Pre-processing, which encompasses ortho-rectification and mosaicking
- Calculation of Built-Up Presence Index (computation of co-occurrence measure, like the contrast, for all the considered directions, integration of different directions in the fuzzy built-up area membership)
- Extraction of built-up areas polygon (calculation of the de-fuzzyfication threshold and polygon extraction)
- Layer production (visual interpretation, cross-checking)

There are numerous advantages in the selection of the PanTex index, compared to the general theory of the co-occurrence matrices, in order to study urban areas, among which can be found:

- A reduction of edge effects on non-built-up features;
- A robustness against seasonal changes, from multi-sensor images, or multi-scenes, i.e. images with various illumination, weather, atmospheric conditions;
- A robustness against image compression based on wavelet transformation;
- A robustness for various landscapes present in the scene;
- The use of panchromatic images instead of multi-spectral datasets;
- No need for calibration of the input data;

- No need for training data.

From the list of parameters needed to use the co-occurrence matrices alone, the PanTex leaves the user only one free parameter to set up, the value of the threshold applied to the built-up index continuum function to generate discrete polygons.

### Fourier transforms

The Fourier transform  $\hat{f}$  is the representation of a temporal function  $f$  in the frequency space

$$\hat{f}(k) = \int_{-\infty}^{\infty} f(t) e^{-ikt} dt$$

where  $i$  is the imaginary number and  $k$  is the frequency. The transformation is reversible. For an image  $I(x, y)$  of size  $n * m$ , the Fourier transform can be written as:

$$\hat{I}(k, l) = \frac{1}{NM} \sum_{x=0}^{N-1} \sum_{y=0}^{M-1} I(x, y) e^{-i2\pi\left(\frac{xk}{N} + \frac{yl}{M}\right)}$$

All frequencies are represented, whichever their direction in the image is. A privileged direction for the studies is not needed to determine and isolate a given pattern, contrary to the previously mentioned indices like the GLCMs.

Yet, the Fourier transform is applied on the whole image, and the frequency spectrum cannot spatially localize the characteristics of the texture; this can be eventually resolved by using a sliding window, but it therefore introduces the size of the window as another parameter to set up.

### Wavelet transformation Analysis

The wavelet transform has been theorized by (Morlet et al., 1982a) and (Morlet et al., 1982a, 1982b) to study seismic activities. This approach has been reused in image processing (Mallat, 1989; Meyer, 1990). The continuous wavelet transform of a continuous signal  $f$  is written as:

$$\mathcal{F}(a, b) = \int_{-\infty}^{+\infty} f(t) \frac{1}{\sqrt{a}} \varphi^* \left( \frac{t-b}{a} \right) dt$$

where  $a$  is the scale factor that cannot be null,  $b$  is a real number called the translational value and  $\varphi^*(t)$  is the complex conjugate of  $\varphi$ , which is a continuous function in the time domain as well as in the frequency domain. This function, called a “mother wavelet”, is used to derive “daughter wavelets”, translated and scaled for different  $a$  and  $b$  parameters.

$\mathcal{F}(a, b)$  is the projection of  $f(t)$  on the analysis function  $\varphi^* \left( \frac{t-b}{a} \right)$  which can be chosen among various wavelet types, such as the Morlet wavelet, the Mexican hat wavelet, the Haar wavelet, or the Hermitian wavelet. One can demonstrate that the family of functions defined by  $\varphi_{j,m}(k) = 2^{-i/2} \varphi(2^{-i} * k - m)$  forms an orthonormal basis, which can therefore represent the whole signal without loss. An image  $I$  is represented in those basis functions as

$$I = \sum_m c_{j_0,m} * \varphi_{j,m}(k) + \sum_{j \leq j_0} \sum_m d_{j,m} * \psi_{j,m}$$

where the  $c_{j_0,m}$  is the continuous component at the scale  $j_0$  and  $d_{j,m}$  are the detailed component (or high frequency component).

### 3.4 Candidate interpolation and fusion approaches for benchmarking

In the following, the candidate methods for integration and fusion approaches to combine S-1, S-2 and S-3 data with regards to the envisaged evolution of Copernicus Land Services are presented.

#### 3.4.1 Candidate approaches for integration of S-1/S-2 complementary information

Aim of the integration of S-1/S-2 data is to better describe the different physical interactions with the land surface, defining primarily different characteristics of the LC/LU objects, and thus improving mapping accuracy. Optical multispectral data on the one side describe e.g., the leaf structure, pigmentation and moisture of vegetation, while SAR data on the other side describe their size, density and dielectric properties. Two approaches of the three methods mentioned above, are most relevant for this analysis: the feature fusion based on indices derived from each sensor (pre-classification fusion) and the fusion of thematic classification results (post-classification fusion).

For large areas, sets of indicators and metrics derived from time series of SAR and optical data need to be robust, but should deliver complementary information. Various sets of indicators are being used in the literature, which can also be derived from S-1 or S-2 data. The following indicators from optical and SAR data have been identified of being useful and improving the thematic classification results: Backscatter coefficient and polarisation ratio (VH/VV) for SAR data as well as the multispectral indices NDVI, NDBI, MNDWI, NDMIR, NDRB. Furthermore, temporal statistics on the derived indices based on defined seasons and time intervals (i.e.,  $NDVI_{mean}$ ,  $NDVI_{max}$ ,  $NDVI_{min}$ , etc.) are applied as they are useful especially for determining vegetated classes (Esch et al., 2018). The presented candidate indices and bands are input for further testing the feature and decision level fusion:

- For feature level fusion the bands and indices from S-1 and S-2 are stacked into one dataset, which is then used for the classification of the specific HRL.
- For the decision level fusion, the classifications are performed separately based on either S-1 data or S-2 data. The results of both classifications are then fused based on post-classification decision rules.

#### 3.4.2 Candidate approaches for spectral, spatial, temporal interpolation and/or fusion approaches

The synergistic use of the high spatial resolution of S-2 data with the high temporal frequency of S-3 time series aims to improve significantly the continuous monitoring of ecosystem dynamics in heterogeneous landscapes and cloud-affected areas. The candidate approaches for spectral, spatial and temporal fusion between S-2 and S-3 data have to be able to capture the initial, middle and final states of changes shapes and thus capture phenology, crop growth disturbance and land cover change processes, while taking explicitly into account the spatial and spectral resolution discrepancies between images. The high spatial resolution S-2 data act as phenology “transition points” that bracket the temporal interpolation supported by S-3 time series or other coarse resolution - high revisit frequency alternatives.

The selected methods for this spatio-spectro-temporal fusion are the following ones: the Bayesian data fusion (Fasbender et al., 2009; Xue et al., 2017), the STARFM and ESTARFM (Gao et al., 2006; Zhu et al., 2010) and the Kalman filtering (Kempeneers, 2016). These methods are justified and described in section 4.1.2. As none of these approaches has been applied to both S-2 and S-3 data, or S-2 and PROBA-V data and they have to be adjusted to the specifications of the respective sensors.

### 3.4.3 Candidate approaches for spectral time series metrics/variables

Time series of images provided by sensors such as S-3 or MODIS cover wide areas on a daily basis, while time series acquired by S-2 and other similar sensors such as Landsat cover a few hundreds of square kilometres, but with less than a dozen of exploitable acquisitions during the year. To identify grassland cover at a field scale, for example, this scarce temporal availability of high-resolution images is problematic, as a full season cycle cannot properly be reconstructed based on so few points on the temporal scale.

In this part, candidate approaches that are looked at aim at quantifying the accuracy of the vegetation cycle based on data acquired by S-2 and the fused images. To this end, the most widely used indices are looked at, such as the NDVI, the NDBI, and the NDWI, while their statistical properties are computed in order to select the most relevant ones to study seasonal changes in the vegetal cover and as well as other kinds of evolution in the rest of the AOI not covered in greenery, by contrast. Other metrics can be constructed to focus on a particular land cover class or usually in combination with one or several spectral or textural indices reviewed in part 3.3.2. The types of variable can be listed as:

- **Statistical metrics of spectral values over one or several periods**, such as the average, the maximum, the minimum – especially relevant to follow seasonality and phenology, they can be used as descriptive or predictive tools, in particular to identify certain land cover classes or to monitor the evolution of forest cover;
- **Change metrics**, usually derived from a segment of radiometrically calibrated images, called a temporal trajectory, for example, the magnitude and the duration of the change, or the slope of the modelled trend – they are also used to characterize land cover and to map forest, for deforestation and recovery;
- **Stationary or non-stationary shape variables**, corresponding to the modelling of temporal trajectories as continuous functions of time, that can exhibit stationary (for example, periodic) or non-stationary (e.g. transitions from one cover to another) patterns – deviations from those patterns may characterize the disturbance of the land cover, while expected patterns such as seasonal growth can be used to derive biomass estimates;
- **Trend metrics**, among which one can find simple linear trends, seasonal trends and breakpoints to describe and decorrelate simultaneous landscape processes.

Several indices can be used to form those metrics, the NDVI being one of the most used. The review in Table 3-3 summarizes advantages and disadvantages to use the indices in global time series.

Furby et al. (2008) studied the Landsat time-series over Australia to monitor change in the land cover, and in particular, forests. For each image of the time series, land cover zones of similar spectral properties were constituted, based on manually selected training samples. Using canonical variate analyses and contrasts between forest and non-forest regions, the spectral separability of the samples led to the creation of new indices, combinations of spectral bands, to characterize the ‘woodiness’ of the land cover, and other masks that would help to split the land covers not exactly distinguished by the first index. Thresholds were then set and applied to label forest and non-forest regions with a certain probability, based on the previous images in the time series. The following multi-temporal classification based on neural networks refined the probability and generates a layer of changes from year to year.

**Table 3-3: List of potential candidate indices for the creation of time series.**

CATEGORY	INDEX	ADAPTED FOR GLOBAL TSA	CONDITIONS	REMARKS
SPECTRAL INDEX	NDVI	√	Applied on calibrated images BOA (atmospheric effects corrected)	Composite of images can improve the result
SPECTRAL INDEX	DVI	X	-	Not normalized, different spectral responses from different sensors would yield different DVI over the same AOI
SPECTRAL INDEX	RVI	X	-	Sensitivity to the geometry of the observation
SPECTRAL INDEX	IRECI	X	Used over a specific AOI – not a global scale	-
SPECTRAL INDEX	NDBI	X	-	Not sensitive to the date, works best at the peak vegetation though Not good with details, can depend on the lithological regimes within the AOI (e.g., volcanic vs non-volcanic soils)
SPECTRAL INDEX	NBI	X	-	Depends on the sensor
SPECTRAL INDEX	NDWI	√	Applied on calibrated images BOA (atmospheric effects corrected)	Not sensitive to the date, works best at the peak vegetation though Not good with details
SPECTRAL INDEX	PVI	X	-	Needs to be adapted to the AOI, depends on the soil type
SPECTRAL INDEX	SAVI	X	Used over a specific AOI – not a global scale	Needs to be adapted to the AOI, depends on the soil type
SPECTRAL INDEX	TSAVI	X	Used over a specific AOI – not a global scale	Needs to be adapted to the AOI, depends on the soil type
SPECTRAL INDEX	MSAVI	X	Used over a specific AOI – not a global scale	Needs to be adapted to the AOI, depends on the soil type
BIOPHYSICAL INDEX	LAI	√	Products computed from Landsat raw images, available with the Landsat time series	-
SPECTRAL INDEX	EVI	√	Can be used with TOA images, needs in-situ measurements (?)	Depends on the sensor, on the AOI, on the atmospheric conditions (aerosol presence)
SPECTRAL INDEX	ARVI	√	Can be used with TOA images, needs in-situ measurements (?)	Depends on the atmospheric conditions (aerosol presence)
SPECTRAL INDEX	GEMI	X	-	Unsuitable for creating time series over arid regions, not normalized
SPECTRAL INDEX	NBR (Normalized Burn Ratio)	√	Applied on calibrated images BOA (atmospheric effects corrected)	-
SPECTRAL INDEX	Unknown suitability for time series: UI, BUI, IBI, EBBI, NBUI, MNDWI, MSI, TDVI			
BIOPHYSICAL INDEX	Unknown suitability for time series: fAPAR, FCover			

## 4 Testing and benchmarking of candidate methods

As lined out in the introduction and the interim progress report [AD16], it has been agreed to move the phase II benchmarking to WPs 32-35. Therefore this section discusses the candidate methods identified in chapter 3.4 accomplished in phase I along with their summarized phase I testing and then expands into additional phase II testing of S-2 / PROBA-V time-series fusion, since the S-2 / S-3 time-series fusion, while promising, was not operationally ready [AD06] and therefore not part of any other prototype testing and production.

### 4.1 Description of candidate methods

In the following, the candidate approaches for the integration/fusion of S-1/S-2 as well as S-2/S-3 time series data are explained in detail.

#### 4.1.1 Candidate approaches for integration of S-1/S-2 complementary information

For large areas, sets of indicators and metrics derived from time series of SAR and optical data need to be robust, but should deliver complementary information. Various sets of indicators are being used in the literature, which can also be derived from S-1 or S-2 data. The following indicators from optical and SAR data have been identified of being useful and improving the thematic classification results:

##### *Candidate indices from SAR data:*

Two types of indices are seen to be relevant for a fusion with optical data, namely the backscatter coefficient in the available polarisations (VH, VV), related to plant biomass and morphology and soil conditions (moisture and roughness) (Villa et al., 2015), and polarisation ratios VH/VV (Bach et al., 2012; Dusseux et al., 2014; A. Schmitt et al., 2015).

##### *Candidate indices from optical data:*

According to Esch et al. (2018), six indices are seen to be well-suited for a fusion with SAR data, namely the Normalized Difference Vegetation Index (NDVI), the Normalized Difference Built-up Index (NDBI), the Modified Normalized Difference Water Index (MNDWI), the Normalized Difference Middle Infrared index (NDMIR) and the Normalized Difference Red Blue index (NDRB) and the Normalized Difference Green Blue index (NDGBI).

The NDBI (Zha et al., 2003)) and applied to extract built-up areas in many studies (Xu, 2008); nevertheless, due to the use of the middle infrared band (i.e., band 6 of the Landsat-8 OLI sensor) this index is also sensitive to vegetation with low water content (Xu, 2006) which exhibits values comparable to those of urban areas. Accordingly, the NDMIR and the NDVI are applied to overcome this issue. On the one hand, the NDMIR uses both middle infrared bands, thus being sensitive to vegetation moisture (Lu et al., 2004)). On the other hand, the NDVI was first published by Rouse Jr. et al. (1974) and since then it has been widely employed in a variety of land cover applications. Moreover, the MNDWI is also employed to discriminate water. This index was proposed by (Xu, 2006) who enhanced the performance of the NDWI by replacing the NIR with the MIR band, which leads to a reduction of noise from built-up areas. In addition to the previous, two additional spectral indices introduced by Zhou et al. (2014) have been also included for improving the discrimination between urban areas and bare soil/bare rocks; specifically, these are the NDRB and NDGB indices.

In order to integrate the temporal domain, temporal summary statistics can be calculated on the derived indices based on defined seasons/time intervals (i.e.,  $NDVI_{mean}$ ,  $NDVI_{max}$ ,  $NDVI_{min}$ , etc.), which are frequently found useful especially for mapping vegetated classes (Esch et al., 2018) and which have indeed been utilized in many of the ECoLaSS phase II prototype developments, like the grassland HRL

status layer classification, for example [AD13]. The approach to integrate S-1 and S-2 data used for these prototypes development in ECoLaSS was pixel level fusion by stacking variables derived from both S-1 and S-2 and performing joint modelling.

#### 4.1.2 Candidate approaches for spectral, spatial, temporal interpolation and/or fusion approaches

In the following, the candidate approaches for a spectral, spatial and temporal interpolation/fusion of S-2/S-3 are described in detail. Specifically, those are the Bayesian data fusion (section 4.1.2.1), STARFM and ESTARFM (section 4.1.2.2), as well as the Kalman filtering (section 4.1.2.3).

##### 4.1.2.1 Bayesian data fusion

This BDF framework aims at reconciling various secondary information sources into a unique prediction. The space-time BDF data fusion relies on a general Bayesian Data Fusion approach in the context of spatial data described in Bogaert and Fasbender (2007). The prediction is based on a High-Pass Filtering approach. Details are provided by the high resolution image whereas the global fluctuations and seasonal trends are provided by the coarser image. It relies on the idea that variables of interest cannot be directly observed. Instead, they are linked to the observable variables. Some specific assumptions are chosen in order to tackle the issue of updating high resolution images.

The main advantage of a Bayesian approach is to set the problem of data fusion into a clear probabilistic framework. Another advantage of the BDF framework over other existing multi-sensor data fusion methods is that it proposes a general formulation when accounting for several secondary information sources whatever the nature of this secondary information is. Finally, an appealing feature of the BDF method is that it is freely accessible within the ORFEO Tool Box software.

##### 4.1.2.2 STARFM and ESTARFM

The Spatial and Temporal Adaptive Reflectance Fusion Model (STARFM) (Gao et al., 2006) and the Enhanced Spatial and Temporal Adaptive Reflectance Fusion Model (ESTARFM) (Zhu et al., 2010) algorithms are used to obtain images high in both spatial and temporal resolutions. They can generate synthetic images based on a pair image of coarse-spatial-resolution and high-spatial-resolution (base images) and the coarse-spatial-resolution data on the prediction date through establishing a linear relationship between the base images of coarse-spatial-resolution and high-spatial-resolution.

The STARFM accurately predicts surface reflectance at an effective resolution close to that of high spatial resolution sensor. However, the performance depends on the characteristic patch size of the landscape and degrades somewhat when used on extremely heterogeneous fine-grained landscapes (Gao et al., 2006). To overcome STARFM's inaccurate predictions of the surface reflectance over heterogeneous landscapes, the ESTARFM was proposed and has proven to be extremely effective (Zhu et al., 2010). For this reason, ESTARFM is generally preferred.

Some applications showed that this fusion had excellent abilities as the blended reflectance was closely correlated with the observed reflectance. STARFM and ESTARFM are both shown to be useful in capturing reflectance changes due to changes in vegetation phenology. However, they may have problems in mapping disturbance events when land-cover changes are transient and not recorded in at least one of the baseline high-resolution (e.g., Landsat) images.

##### 4.1.2.3 Kalman filtering

The data assimilation method is presented in Sedano et al. (2014) and Kempeneers et al. (2016). Within the framework of a Kalman filter recursive algorithm (Kalman, 1960) also known as linear quadratic estimation, the method integrates models, observations and their respective uncertainties, with partly or

fully missing variables, in the calculation of the synthetic images at time steps for which medium resolution imagery is not available.

The method provided a robust performance for input data of variable qualities and environmental conditions, highlighting the relevance of including uncertainties in the integration of multi-sensor remote sensing data. One of the strengths of the Kalman filter is its robustness to a relatively large number of gaps in temporal time series. Especially in the context of data acquisition with optical sensors in conditions with frequent cloud cover, this is an important asset. It was also shown that the derived synthetic profile based on the Kalman filter was able to capture the phenological patterns of the crops.

#### 4.1.3 Candidate approaches for spectral time series metrics/variables

The use of spectral or textural indices cannot capture all temporal details of the time series upon which it is built, even less to exploit S-2 and S-3 optical properties at their full potential. It is therefore essential to combine the results of spectral indices with metrics aiming at highlighting the temporal correlations.

For each improved or new product, a candidate method has been selected, based on the following detailed literature review:

- For the forest layer and the crop layer, statistical metrics ought to be tested;
- For the new LC/LU products like CLC+, temporal “reduction” of the time series on a monthly basis looks promising;
- For grassland, the decomposition of seasonality in the vegetation indices into trends has proved to improve the results of classification, in particular for all vegetation type classes;
- For the imperviousness layer, the method is detailed in the WP 34 [AD09], since it entirely relies on change detection.

##### 4.1.3.1 Statistical metrics

Petitjean et al., (2012) proposed a statistical method in time series analysis based on the global comparison between two annual time series, called Dynamic Time Warping (DTW) – where the cost of alignment between two annual quantities (the reflectance of each spectral band, for a given pixel) is measured individually before being merged – by averaging – in order to determine the possible alignment of those multi-temporal sequences (Petitjean et al., 2012).

In their paper, Inglada et al. (2017) designed an almost operational process to determine the land cover type of a time series of images sensed by Formosat-2. To enforce a time coherence between the monthly updates of the product, a “composite” at a fixed date in the month is created by linear interpolation between the available images. All classification processes, with supervised learning, following this treatment are complemented by existing databases, without the input of external in-situ measurements and features extracted from this composite, such as NDVI, NDWI and brightness index.

For the time series of Landsat images over the US aimed to monitor the forest change, from 2006 to 2010, Hansen et al. (2014) used several spectral indices – the NDVI, the brightness temperature – and then derived temporal metrics based on weekly mosaics from them:

- 5-year percentiles per band, for each spectral band;
- All percentiles from the first and last years of the temporal range of the study;
- multi-year percentile differences;
- slope of the linear regression between the band reflectance and the time-sequence observation date;
- And the number of “good” observations.

The training data were extracted in the median NDVI image, which is resistant to the presence of outliers, unlike the mean value.

Regarding the forest layer, it seems relevant to test the statistical metrics used by Hansen et al. (2014) in order to detect the disturbance in the NDVI from year to year. The simple median NDVI over the phenological season, or at a monthly scale, is a good start to measure the relevance of this variable.

At a monthly scale, the temporal option to create a monthly composite at a fixed date based on the interpolation of the previous and following images in the time series. This technique is giving good results for land cover and land use while balancing the volume of data from the time series. It will be explored for the creation of general land cover/land use for products such as CLC+.

Depending on the results of those simple methodologies, it could be interesting to look at the following metrics that one could describe as more refined.

#### 4.1.3.2 Change metrics

In their paper, Franklin et al. (2015) used various metrics to quantify changes in the time series. From the Landsat time series calibrated images, annual best available pixel (BAP) composites were created for each year, from 1990 to 2010, and spectral indices as well as time-series disturbance metrics, assessing the variations of land cover and based on the NBR products, were computed. Those change metrics are:

- the trend type (monotonic trend, single breakpoint or disturbed),
- the NBR root square mean error of the fitted trend regarding to the pixel values,
- the trend magnitude (difference between the first and last values of the fitted trends), the greatest disturbance magnitude, the pre-disturbance magnitude, the post-disturbance magnitude, etc.,
- the greatest disturbance year,
- the greatest disturbance duration, the pre-disturbance duration, the post-disturbance duration,
- the pre-disturbance monotonic trend duration, the post-disturbance monotonic duration, etc.

The use of NBR is justified by the considered AOI, covered with dense boreal forests. This use of time-series metrics as input for the classification of land cover improved overall accuracy by more than 6% compared to the single-date results.

It could be interesting to use the NDVI in place of the NBR if simple statistical metrics mentioned in the previous part were to fail at improving the classification outputs.

However, this method, related to change detection, should be part of the WP 34 – if set up for tests, results will be discussed in the concerned report.

#### 4.1.3.3 Trend metrics: Modeling seasonality

Jia et al. (2014) used the added temporality of the Landsat time series to derive phenological features, based on the NDVI data provided with the raw images. Fusing MODIS and Landsat images with the STARFM algorithm, they obtained a dense time series at the Landsat spatial resolution. The indices extracted were:

- the beginning and ending dates of the growing season;
- the length of the growing season;
- the seasonal amplitude;
- the maximum fitted NDVI value.

The classification based on Maximum Likelihood Classifier (MLC) and Support Vector Machines (SVM) was fed with those indices, improving the land cover identification accuracy by an overall 3%, especially for vegetation type classes. However, they noted that the use of statistical temporal measures related to the NDVI (maximum, minimum, mean, standard deviation values of the time series) did significantly improve the results of classifiers for human-managed vegetation types, compared to the phenological features alone.

## 4.2 Testing criteria

To analyse the usefulness of the described metrics, they can be (1) analysed visually by the operator to qualitatively compare the results, and (2) analysed quantitatively based on a detailed accuracy assessment for the separate HRL classification. A comparative quality assessment of fusion methods can be based on various criteria, none of which is currently considered as standard in the literature. The evaluation of fusion performance can be divided into qualitative and quantitative approaches.

Visual comparison between the merged images given by different fusion methods is the main qualitative approach. The visual inspection will allow observing small added details and artifacts. This methodology can seem subjective, since the interpretation can vary from one observer to the other, due to their qualification. Nevertheless, the “look and feel” method can often more quickly discern chromatic and spatial artefacts in the resulting images, either by examining each spectral band individually or by using colored multi-band composites. Furthermore, comparison between other reference images, e.g. VHR images, can help looking into more detail of the overall chromatic coherence of given entities, such as water bodies, vegetation, bare soils or urban areas. Visual inspection is therefore an indispensable approach to image fusion validation.

There are several spectral quality criteria for quantitative comparisons of fused data. A large family of criteria is based on correlation coefficients. Here, the correlations between the merged and the original images are computed and analyzed as it is clear that the fused band has to be close to the original band. Methods aiming at low color distortion should therefore yield high correlations between the original and fused bands. Correlations have the advantage of comparable value ranges, usually in  $[-1, 1]$ , thus enabling direct comparisons between quality criteria. Correlation coefficients allow to validate temporal fusion approaches by testing fused pixels against pixels previously removed from the time series.

Recently, Alparone et al. (2004) proposed a generalization of the correlation coefficients metric and referred it as Q4 that could also be used in complement. It aims to encapsulate both spectral and radiometric distortion measurements by accounting for local measurements of the following: (i) the correlation coefficient, (ii) the bias and (iii) the change in contrast.

Furthermore, to quantitatively compare those methods however, it seems simpler to look at the results of the classifications based on those metrics. One widely spread measure to estimate the quality of an output of a clustering process is the spectral separability. The spectral separability quantifies the distance between two LC/LU class spectral signatures, for any number of spectral bands that is effectively used in the classification process. It can spot unused spectral bands, and also evaluate the accuracy of a given classification output. This metric can be calibrated by several distances, among which:

- the Euclidian distance;
- the Jeffries-Matusita distance (Swain et al., 1971).

The Euclidian distance is computed as the spectral distance between the mean vectors of each pair and is written as:

$$d(X, Y) = \sqrt{\sum_{i=1}^n (x_i - y_i)^2}$$

Where  $x$  is the first spectral signature vector,  $y$  is the second and  $n$  is the number of bands considered. It is a very simple measure and can be useful to evaluate the output of a Minimum Distance classification.

The Jeffries-Matusita distance calculates the separability of two probability distributions, the spectral classes, and is expressed as:

$$J_{xy} = 2 * (1 - e^{-B})$$

where:

$$B = \frac{1}{8}(x - y)^T \left( \frac{\Sigma_x + \Sigma_y}{2} \right)^{-1} (x - y) + \frac{1}{2} \ln \left( \frac{\left| \frac{\Sigma_x + \Sigma_y}{2} \right|}{|\Sigma_x|^{\frac{1}{2}} * |\Sigma_y|^{\frac{1}{2}}} \right)$$

$\Sigma_x$  and  $\Sigma_y$  being the covariance matrix for, respectively, the mean vectors of each signature  $x$  and  $y$  being compared. The Jeffries-Matusita distance is known to perform better than other distance measures (such as the Euclidian distance or the divergence) but it is costly to fully compute, due to the multiple presence of covariance matrices in its expression - and can become expensive for a high number of classes.

### 4.3 Implementation of Testing

#### 4.3.1 Candidate approaches for integration of S-1/S-2 complementary information

The proposed method for the integration of S-1/S-2 imagery can only be assessed qualitatively by visual inspection within this WP. The proposed method needs labelled data to compare the gain brought by the combination of spectral indices and temporal metrics. Therefore, various classification methods that were explored in much further detail in [AD08] quantitatively analyse the to-date proposed methods concerning the different thematic classification.

This section illustrates the potential complementarity of S-1 and S-2 derived time-series statistics. The following methodology was used: Based on pre-processed S-2 (atmospherically corrected and cloud masked) and S-1 (gamma naught VV) the indices proposed in chapter 4.1.1 are computed and summarised over the full time series data. The resulting statistics are then compared individually as well as in S-1 / S-2 fused RGB displays. Important features, which are best discriminated only when combining S-1 and S-2 derived features, are discussed.

In the following, the indices and temporal metrics derived for the South-East test site for S-1 and S-2 data from 2017 are discussed. Figure 4-1 shows the temporal mean over one year (2017) of S-2 blue (Band 2), green (Band 3) and red (Band 4) reflectance. In direct comparison, Figure 4-2 shows the temporal mean of one year of the S-1 gamma naught backscattering coefficient (VV, descending). Figure 4-3 presents an optical-only RGB composite of the mean NIR, red and green band over the course of 2017. Figure 4-4 shows a false colour composite of the mean NDBI, NDVI and MNDWI. Here, one can see that mineral extraction sites (see the bright red areas in the small top image on the right) have a similar spectral behaviour as the dense urban areas in the centre of Toulouse (which can be seen on the right sight of the big image and appear in a bright red colour). These areas would be most likely misclassified using only optical imagery from S-2.

Figure 4-5 shows a false colour composite of temporal mean of the S-1 backscattering coefficient, the mean MNDWI and mean NDBI and Figure 4-6 shows a false colour composite of temporal mean of the S-1 backscattering coefficient, the mean NDMIR and mean NDBI. In both figures one can see that the before mentioned extraction sites show a different spectral behaviour compared to the dense urban areas and thus, the complementary information derived from S-1 data in addition to optical data are promising in helping to distinguish between urban areas and bare soil. Moreover, in Figure 4-5 one can clearly distinguish between inhabited (in purple colours) and industrial areas (in bright yellow colours). Furthermore, one can better differentiate between forests (in brown colours) and grassland areas (in dark blue colours) in Figure 4-5.

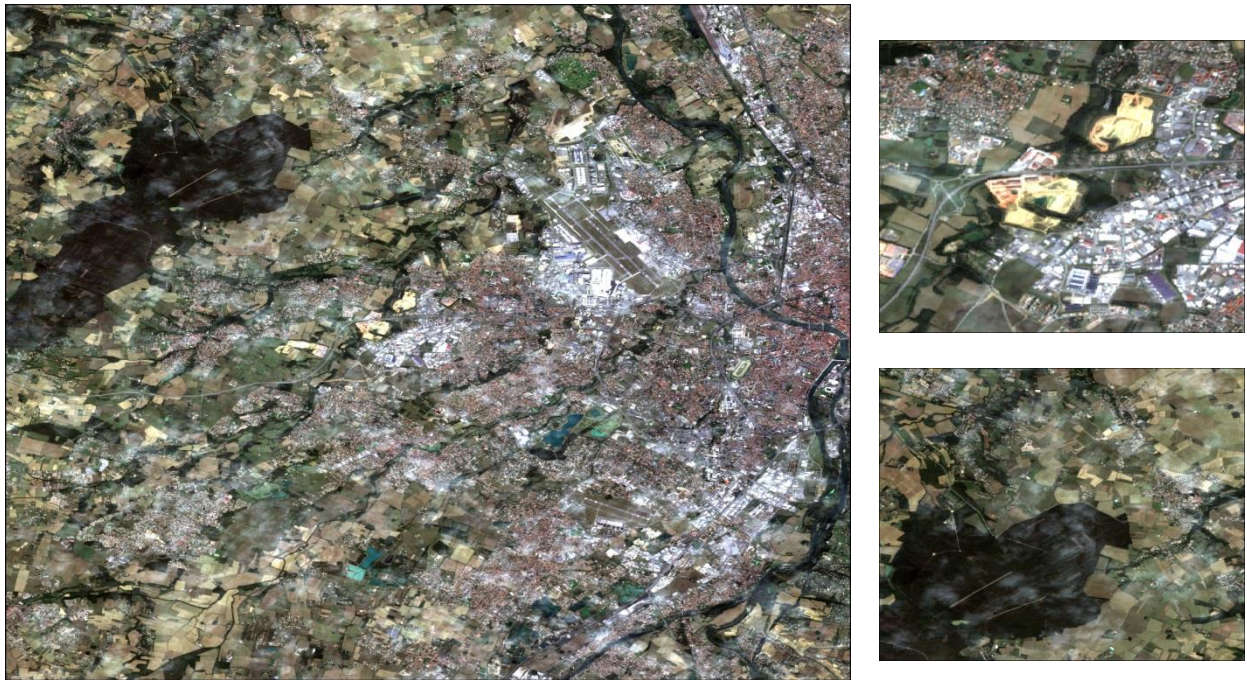


Figure 4-1: S-2 Mean true-colour RGB for 2017 for area West of Toulouse.

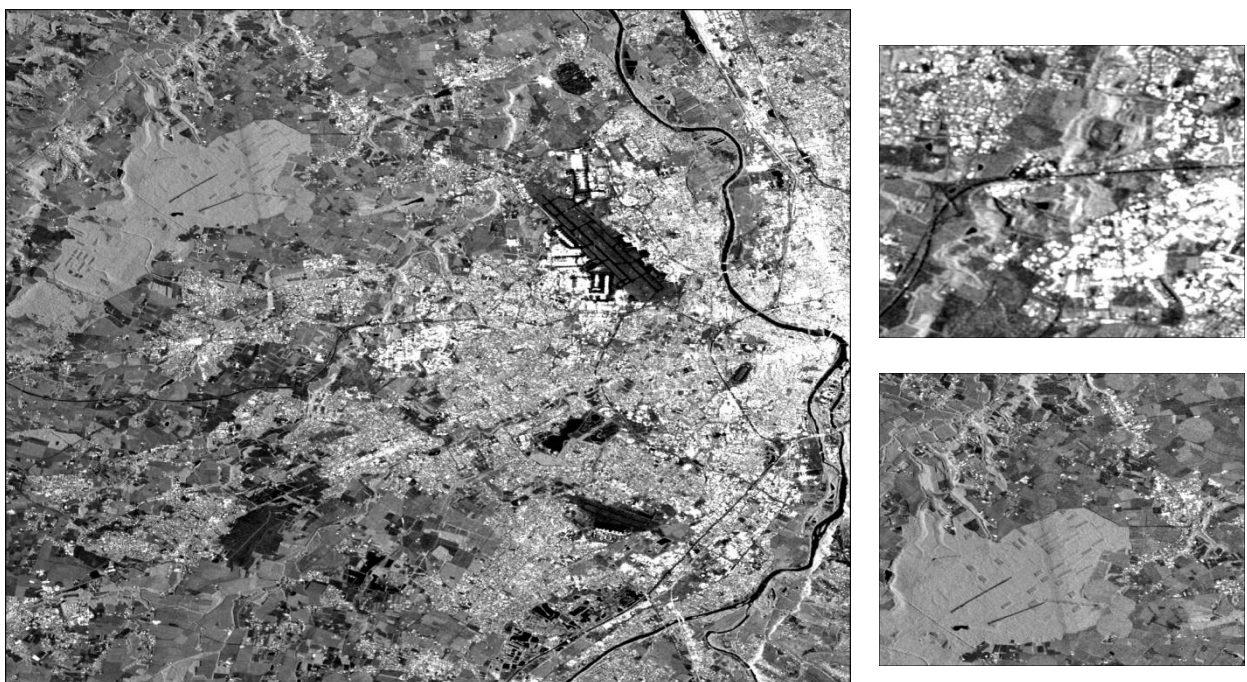


Figure 4-2: S-1 VV gamma naught descending mean for Area West of Toulouse over the entire year 2017.

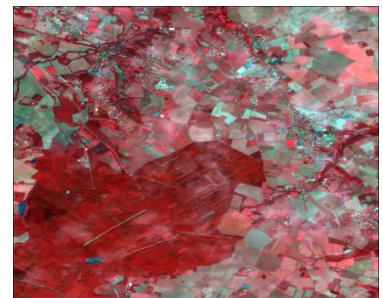
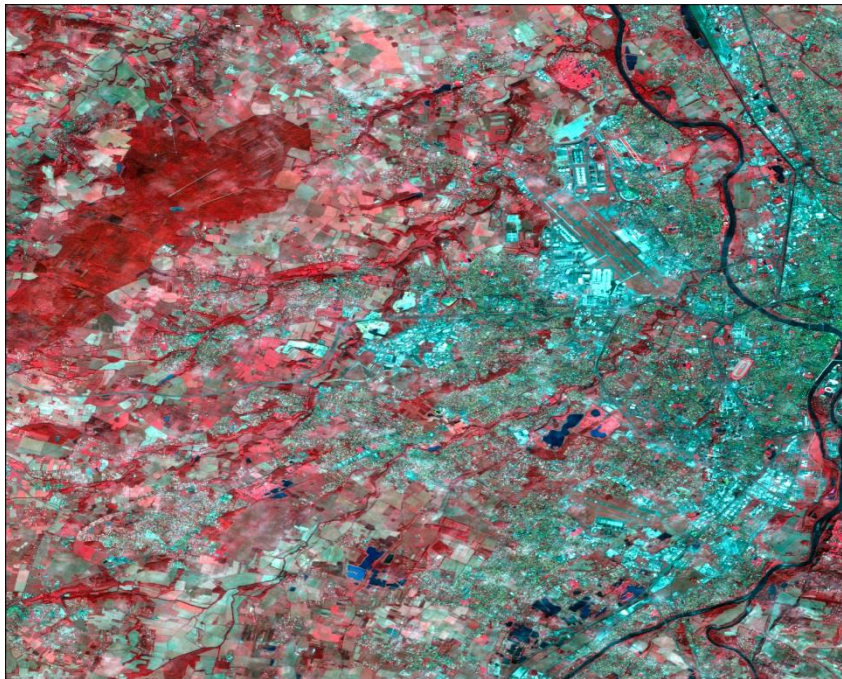


Figure 4-3: S-2 Optical only false colour composite of bands R: NIR MEAN, G: RED MEAN and B: GREEN MEAN for Mean of 2017 for area West of Toulouse.

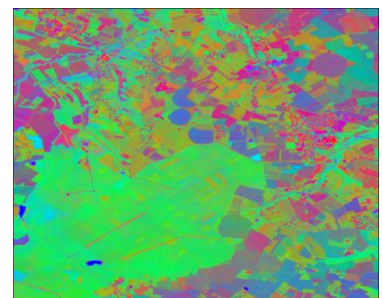
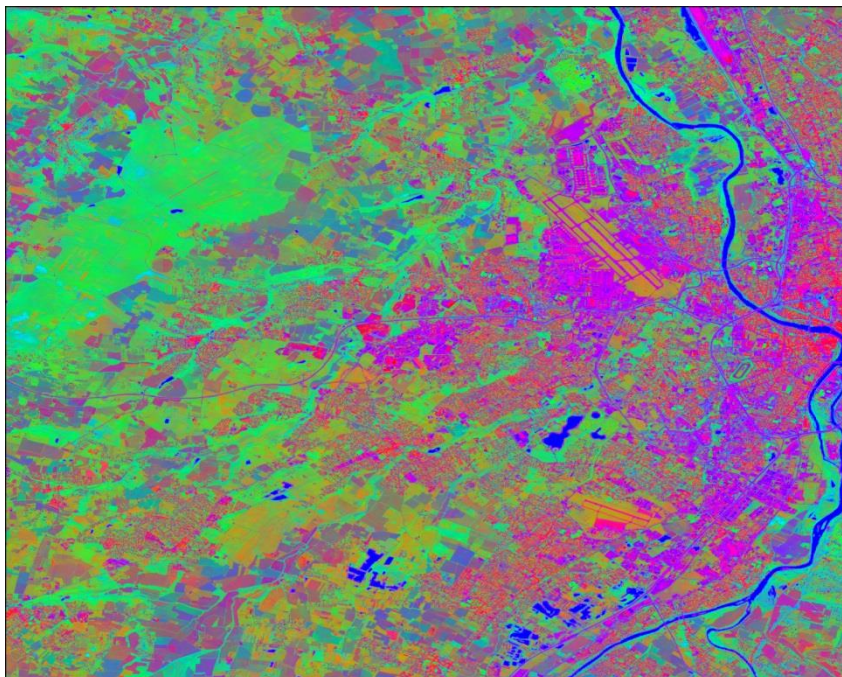


Figure 4-4: Optical only S-2 false colour composite of R: NDBI MEAN, G: NDVI MEAN and B: MNDWI MEAN for 2017 for area West of Toulouse.

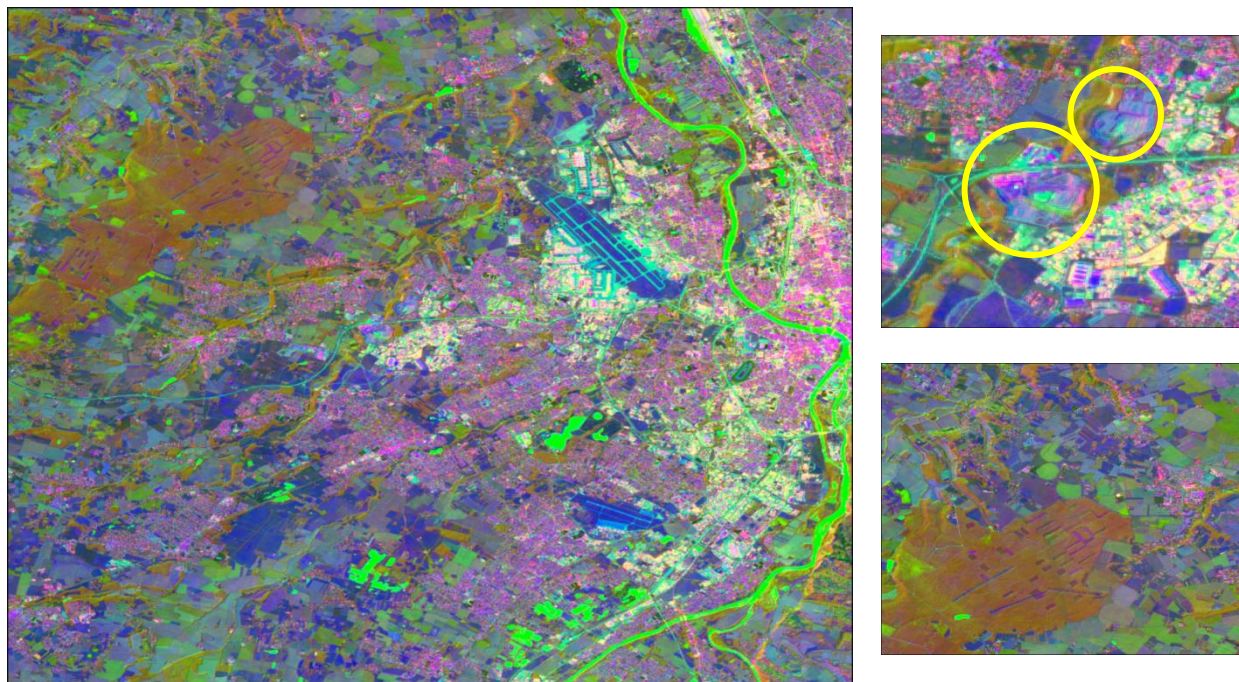


Figure 4-5: S1/S2 fusion colour composite of bands R: S-1 VV MEAN, G: S-2 MNDWI MEAN and B: S-2 NDBI MEAN for Mean of 2017 for area West of Toulouse.

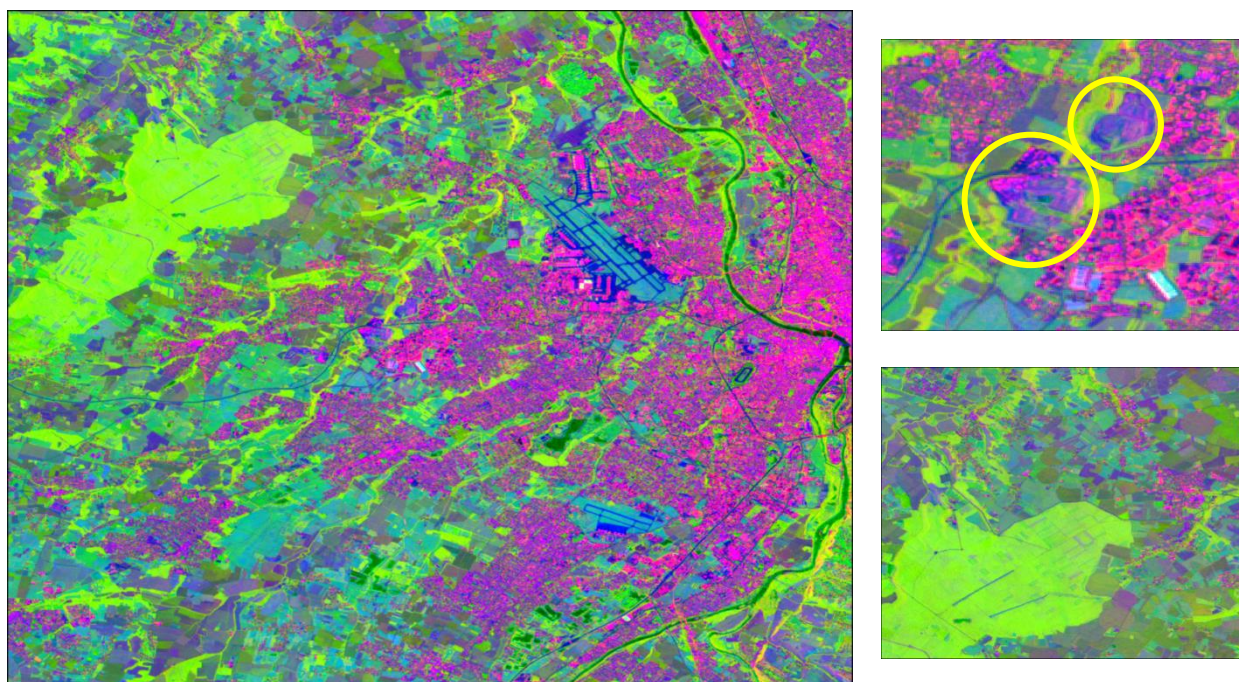


Figure 4-6: S1/S2 fusion false colour composite of bands R: S-1 VV MEAN, G: S-2 NDMIR MEAN and B: S-2 NDBI MEAN for Mean of 2017 for area West of Toulouse.

#### 4.3.2 Candidate approaches for spectral time series metrics/variables

This section takes a quantitative approach to follow up on the previous section. It tests how the separability between major LC classes is influenced by different S-2 predictors. To this end, it uses an existing LC classification as reference data and extracts and quantifies their separability based on the

statistical distance metrics introduced in Section 4.2, namely the Euclidean distance and the Jeffries-Matusita distance.

#### 4.3.2.1 Methodology

First, the 31UFS S-2 granule is selected due to its flat terrain and the full year 2016 is used. Due to a strong cloud cover, the initial count of 63 images is reduced to 19 exploitable images. It should be noted that most of the observations are still exhibiting cloud presence, which reduces the real number of images used in the computation of the temporal metrics. Fused data between S-2 and S-3 should provide much denser time series in the future.

Secondly, spectral indices, NDVI, NDBI and BI, are computed for each remaining image which have been pre-processed images by the JR over the Belgium site.

Thirdly, statistical metrics are derived for the yearly time series, for each spectral index. The yearly extrema (minimum and maximum) are computed per pixel as well as the standard deviation. Due to its sensitivity to outliers, the mean is passed over in favour of the median.

Fourthly, the spectral distances (Euclidian and Jeffries-Matusita) are computed over parts of the images already correctly identified and labelled, which can be used as training data (composed of 108 different polygons), for simple clusters of five classes – cropland (class 1), forest (class 2), grassland (class 3), urban areas (class 4) and water bodies (class 5).

In the following figures, Figure 4-7 to Figure 4-10, metrics related to the NDVI have been computed. The Figure 4-8 depicts the computed median NDVI over the entire time series composed of 18 exploitable images for the year 2016 which is less sensible to outliers than the arithmetic mean. The Figure 4-7 displays the maximal NDVI, while the minimal values of the NDVI can be seen on the Figure 4-9 – the darker the green, the denser the vegetal cover is. Finally the standard deviation, which captures the phenological variations of the NDVI is depicted in the Figure 4-10.

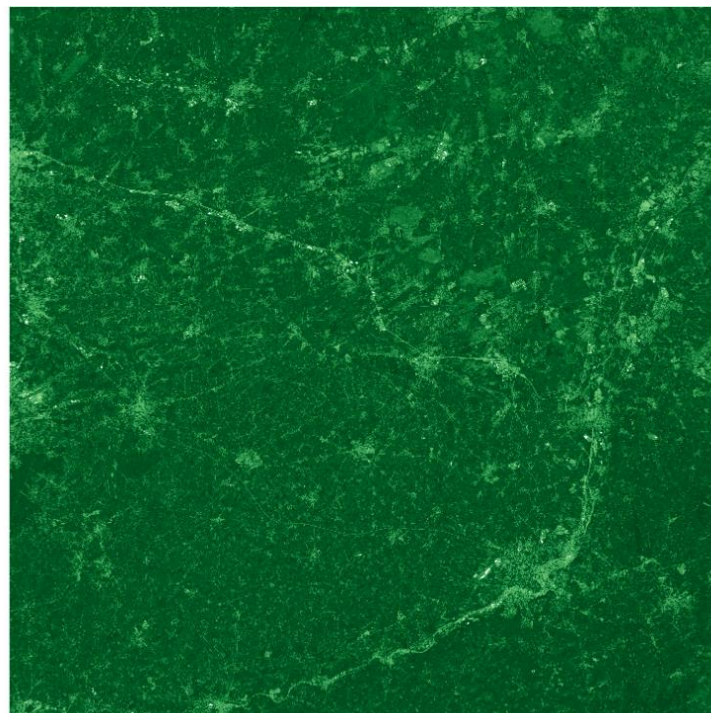


**Figure 4-7: Maximal NDVI values per pixel: the dark green zones indicate the presence of vegetation, while lighter zones characterize urban areas and water bodies.**

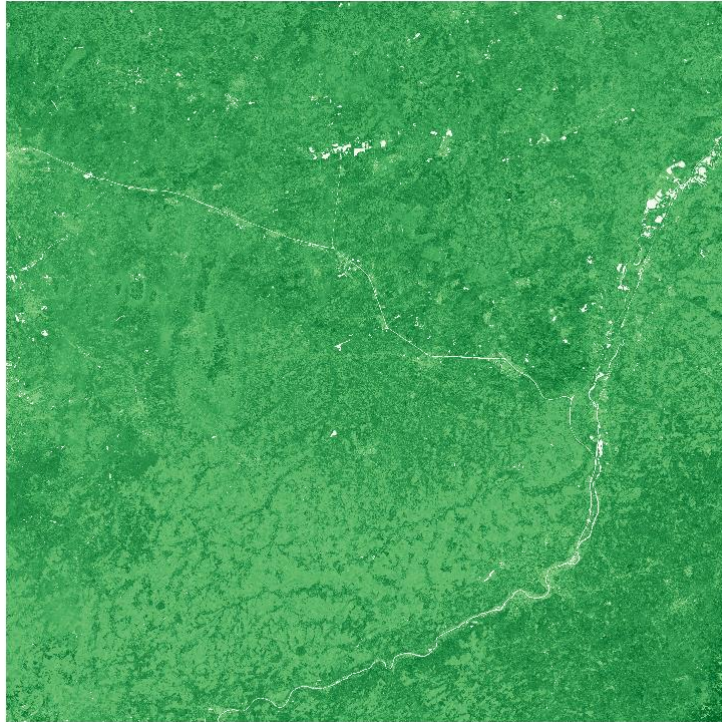


**Figure 4-8: Computed NDVI median over 19 images for the year 2016, on the whole 31UFS tile. Negative values (minimum at -1) are represented in white and positive values (maximum at +1) in dark green.**

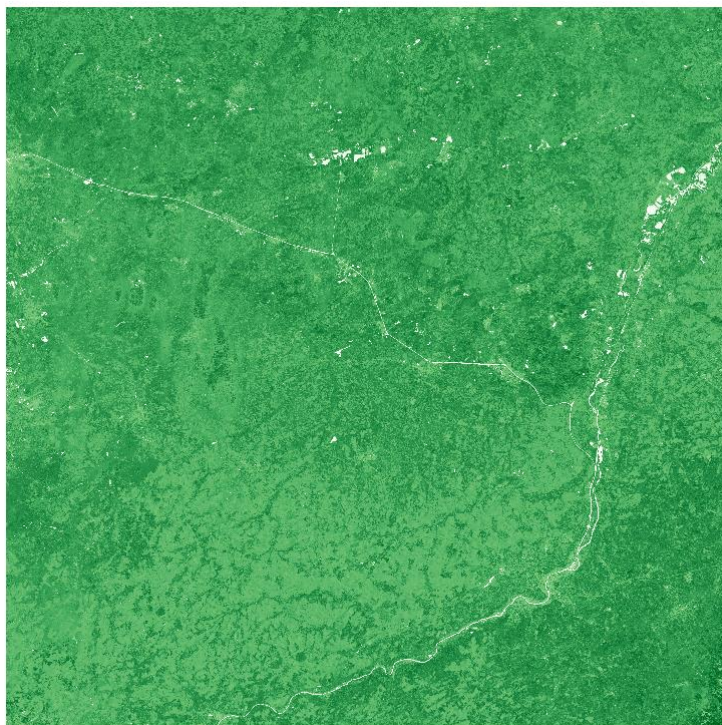


**Figure 4-9: Computed minimal NDVI values per pixel: the lowest values highlight the presence of water bodies and urban areas.**

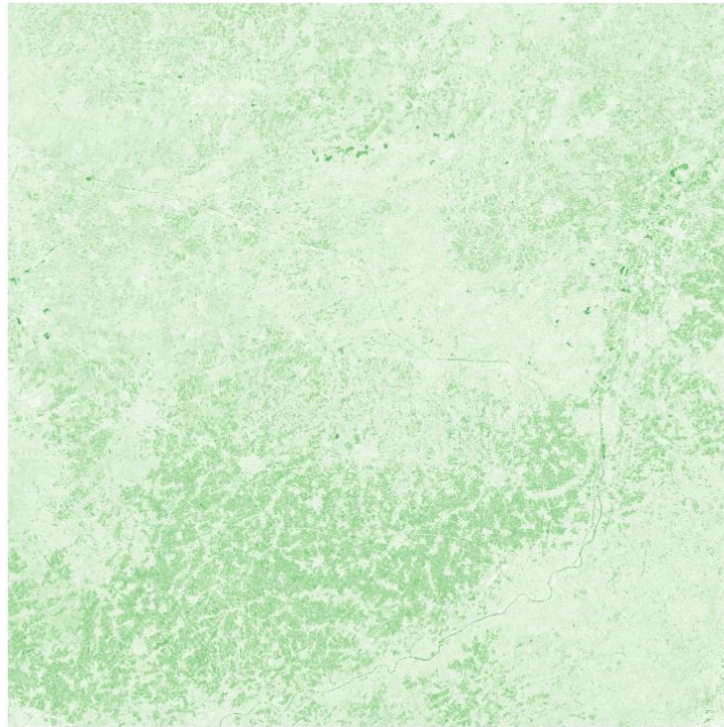


**Figure 4-10: Computed standard deviation NDVI values per pixel: the highest values indicate areas where the NDVI varies the most – here, where vegetation is the densest.**

The next set of images, Figure 4-11 to Figure 4-14, the same metrics have been computed based on the NDBI this time. The maximal values of the NDBI, seen on Figure 4-11, highlight the water bodies, whose NDBI can be very high, which is unusual but can be related to the suspended matter in water or the sunglint effect. The minimal values of the NDBI, on Figure 4-13, and the standard deviation, on Figure 4-14, can be used to spot urban areas, whose NDBI stays constant at a positive value. The median NDBI, on Figure 4-12, highlights its indiscriminated sensitivity to bare soils as well as urban areas.

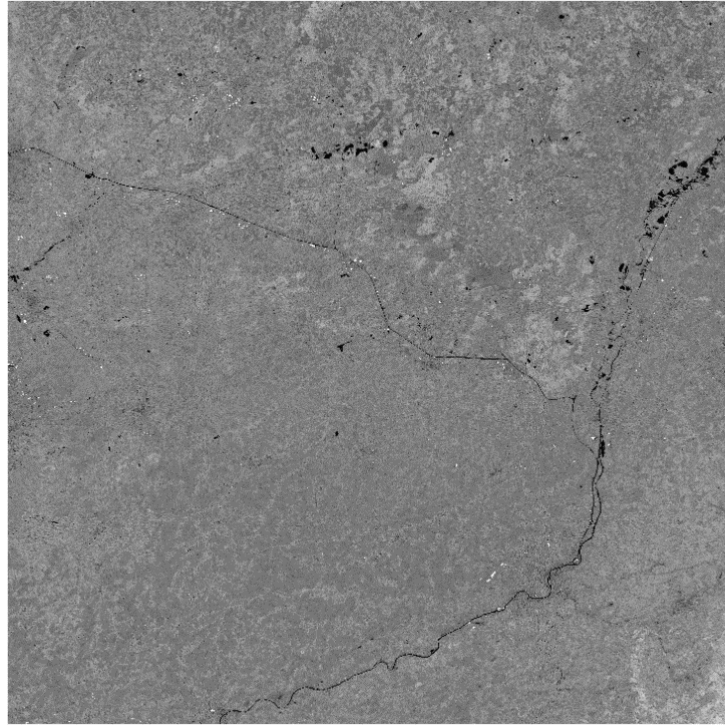


**Figure 4-11: Maximal NDBI values per pixel: the black (positive values near +1) values delineate the water bodies with high suspended matter that reflects MIR wavelengths stringer than the NIR.**

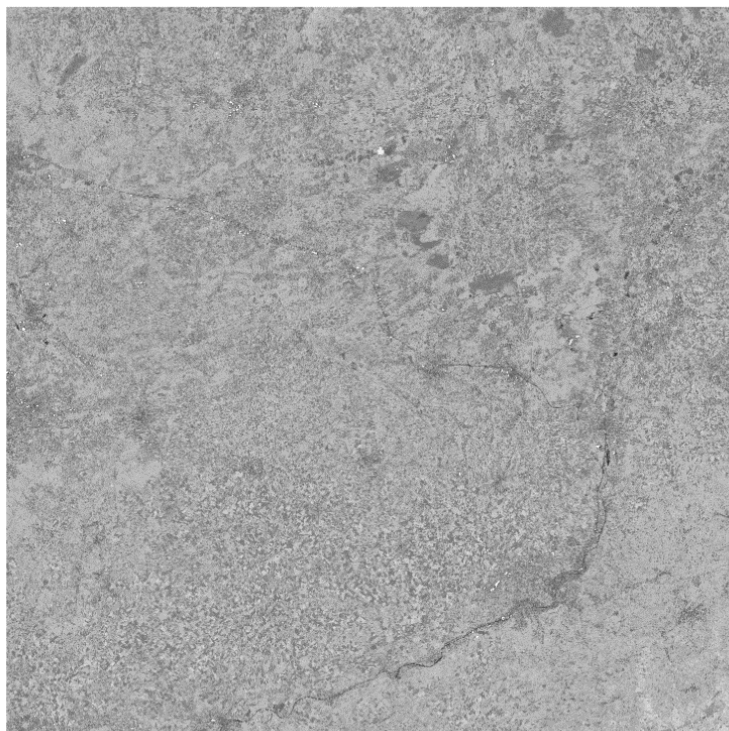


**Figure 4-12: Median NDBI values per pixel: the highest values (in dark grey) are found over urban areas as expected.**

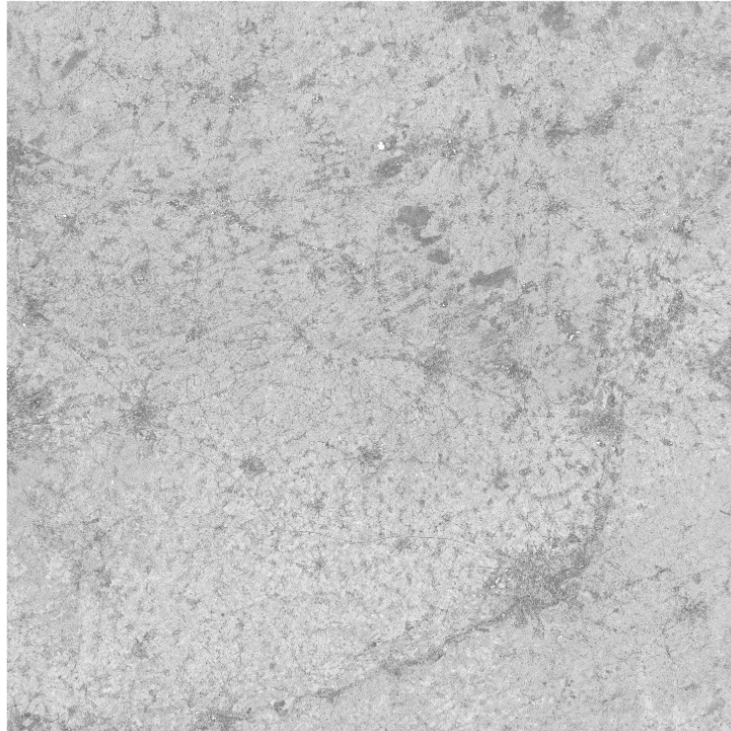


**Figure 4-13: Computed minimal NDBI values per pixel: the highest values (in dark grey) over urban areas are even more highlighted than with the maximal values.**

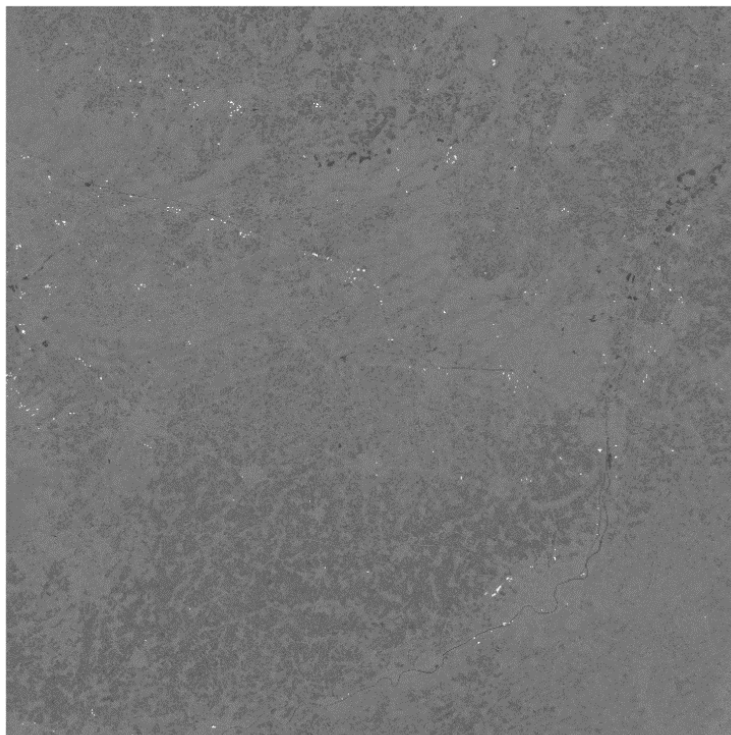


**Figure 4-14: Computed standard deviation NDBI values per pixel: areas where the NDBI varies the most are vegetated, as expected due to the seasonality.**

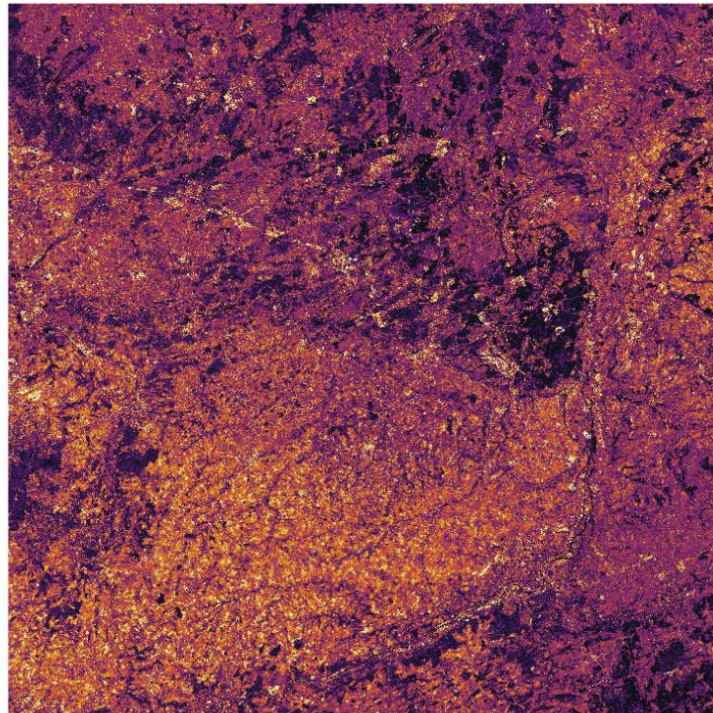


**Figure 4-15: Computed median values for the red band (3) per pixel: the blackest values indicate the least reflective zones, while the yellowest are the brightest, as seen in this band.**

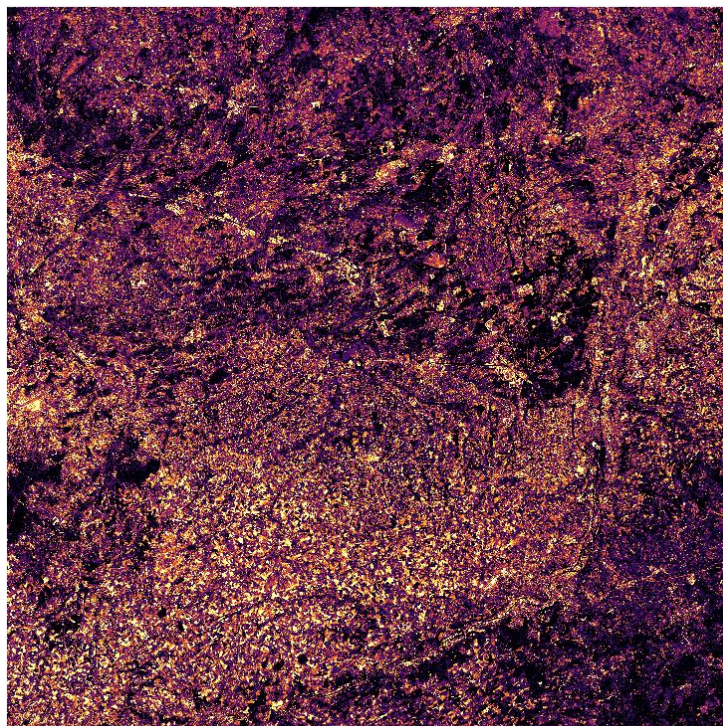


**Figure 4-16: Computed median values for the green band (4) per pixel: the blackest values indicate the least reflective zones, while the yellowest are the brightest, as seen in this band.**

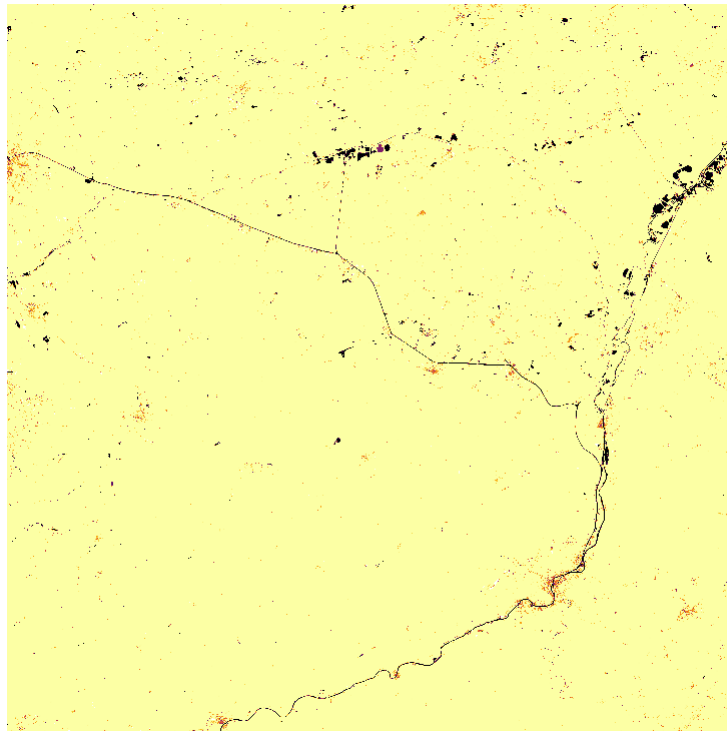


**Figure 4-17: Computed median values for the narrow red edge band (7) per pixel: the blackest values indicate the least reflective zones, while the yellowest are the brightest, as seen in this band.**

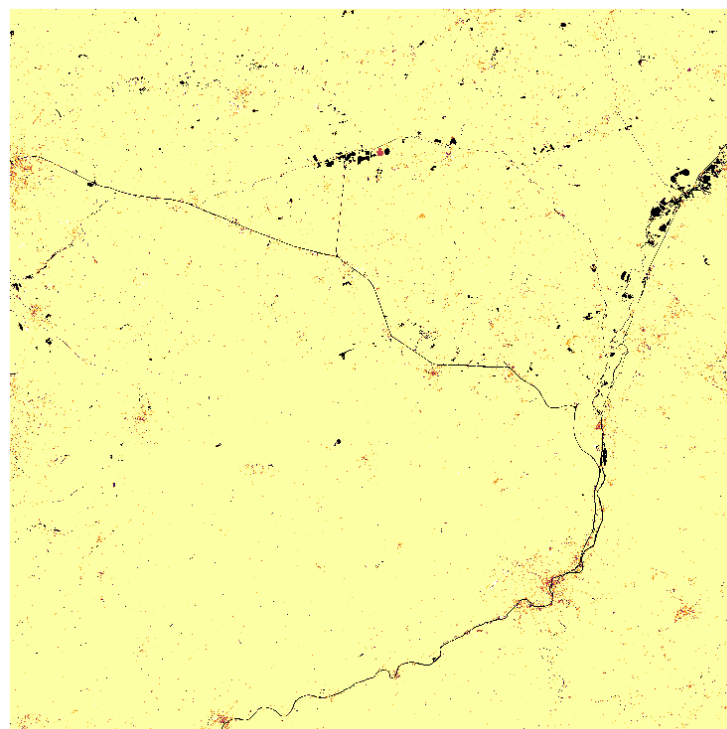


**Figure 4-18: Computed median values for the wide red edge band (8) per pixel: the blackest values indicate the least reflective zones, while the yellowest are the brightest, as seen in this band.**

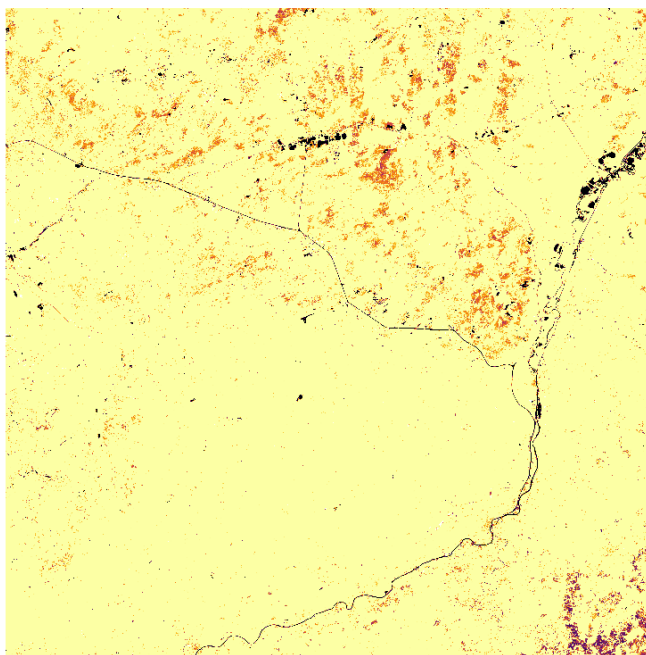


**Figure 4-19: Computed median values for the first SWIR band (11) per pixel: the blackest values indicate the least reflective zones, while the yellowest are the brightest, as seen in this band.**

As a point of reference, the five most significant band mean values are displayed in Figure 4-15 (for the red band 3), in Figure 4-16 (for the green band 4), in Figure 4-17 (for the narrow red edge band 7), in Figure 4-18 (for the wide red edge band 8) and in Figure 4-19 (for the first SWIR band 11). Some features can be easily identified, such as water bodies and some part of urban areas, but the discrimination brought by the spectral indices is clearly stronger.

#### 4.3.2.2 Results and conclusion for the statistical metrics

The Euclidian distance is not confined – unlike the Jeffries-Matusita distance which is limited by the value  $1000 * \sqrt{2}$ . This means for the Jeffries-Matusita a compression of the lowest or highest values; the two distances are thus complementary. Whichever distance is used, the higher the distance value is, the more separated the two considered classes are.

#### *NDBI statistical metrics and their spectral signatures*

Using only the NDBI and its statistical metrics leads to a good discrimination between the water bodies and the other type of land cover, but urban areas and grassland zones are not well separated, as seen in Table 4-1 and Table 4-2. The index cannot be used alone without further spectral or spatial information.

**Table 4-1: Euclidian distance of LC discrimination using NDBI statistical time-series metrics (maximum, median, minimum, standard deviation). Classes are coded as integers. Cropland = 1 etc.**

		1	2	3	4	5
CROPLAND	1	0.00	0.26	0.27	0.40	0.88
FOREST	2		0.00	0.33	0.37	1.08
GRASSLAND	3			0.00	0.15	0.77
URBAN	4				0.00	0.84
WATER	5					0.00

**Table 4-2: Jeffries-Matusita distance of LC discrimination using NDBI statistical signatures.**

		1	2	3	4	5
CROPLAND	1	0	1320.19	1110.06	1351.08	1409.13
FOREST	2		0	1173.81	1141.91	1412.2
GRASSLAND	3			0	886.304	1350.65
URBAN	4				0	1384.25
WATER	5					0

*NDVI statistical metrics and their spectral signatures*

The NDVI signatures outperform the NDBI ones to separate the five classes, as seen in Table 4-3 and Table 4-4. However, as expected, small vegetation classes (cropland and grassland) exhibit the weakest score. This may be resolved by using a different temporality for the statistical metrics, based not on the year, but on the phenological seasonality.

**Table 4-3: Euclidian distance of LC discrimination using NDVI statistical signatures.**

		1	2	3	4	5
CROPLAND	1	0.00	0.31	0.17	0.56	1.43
FOREST	2		0.00	0.26	0.68	1.70
GRASSLAND	3			0.00	0.45	1.45
URBAN	4				0.00	1.15
WATER	5					0.00

**Table 4-4: Jeffries-Matusita distance of LC discrimination using NDVI statistical signatures.**

		1	2	3	4	5
CROPLAND	1	0.00	1318.78	1064.58	1385.77	1413.66
FOREST	2		0.00	1223.86	1323.15	1414.21
GRASSLAND	3			0.00	1152.05	1412.17
URBAN	4				0.00	1403.54
WATER	5					0.00

*Combined NDBI and NDVI statistical metrics and their spectral signature*

The best results are achieved when all spectral information condensed in both indices are used to separate LC/LU classes, as shown in Table 4-5 and Table 4-6. Compared to the NDVI results, it should be noted that the cropland and grassland weak discrimination is greatly improved.

**Table 4-5: Euclidian distance of LC discrimination using NDBI/NDVI statistical signatures.**

		1	2	3	4	5
CROPLAND	1	0	0.41	0.32	0.69	1.68
FOREST	2		0	0.42	0.77	2.01
GRASSLAND	3			0	0.47	1.64
URBAN	4				0	1.42
WATER	5					0

**Table 4-6: Jeffries-Matusita distance of LC discrimination using NDBI/NDVI statistical signatures.**

		1	2	3	4	5
<b>CROPLAND</b>	1	0	1394.49	1257.52	1405.64	1414.19
<b>FOREST</b>	2		0	1317.1	1351.04	1414.21
<b>GRASSLAND</b>	3			0	1297.18	1413.72
<b>URBAN</b>	4				0	1412.5
<b>WATER</b>	5					0

*“Reference data”: the spectral signature of 5 of the most significant bands for S-2*

As a point of comparison, reflectance in five bands (the red band, the green band, one of the red edge narrow bands, the wide red edge band and the first SWIR band) among the most significant (at 10 and 20m resolution) have been used to generate statistical metrics for the year 2016. Using those five independent sources of spectral information leads to what can be considered as the best separability achievable by our selection of indices, as shown in Table 4-7 and Table 4-8.

**Table 4-7: Euclidian distance of LC discrimination using bands 3-4-8-7-11 statistical signatures.**

		1	2	3	4	5
<b>CROPLAND</b>	1	0	4553.08	2540.89	4200.23	8763.16
<b>FOREST</b>	2		0	2345.96	1752.29	4518.30
<b>GRASSLAND</b>	3			0	1980.18	6557.42
<b>URBAN</b>	4				0	4960.12
<b>WATER</b>	5					0

**Table 4-8: Jeffries-Matusita distance of LC discrimination using bands 3-4-8-7-11 statistical signatures.**

		1	2	3	4	5
<b>CROPLAND</b>	1	0	1414.19	1379.59	1413.71	1414.21
<b>FOREST</b>	2		0	1409.72	1408.83	1414.21
<b>GRASSLAND</b>	3			0	1404.24	1414.21
<b>URBAN</b>	4				0	1414.21
<b>WATER</b>	5					0

**Conclusion**

The statistical metrics (extrema, standard deviation and median) derived from the five most significant bands contain the most complete information, therefore lead to the best results regarding the spectral separability of targeted classes, as assessed over the training data. The combination of two classical spectral indices, the NDBI and NDVI and their statistical metrics, gives the next best results compared to the statistical metrics directly derived from a selection of the most meaningful bands. The spectral separability of the five test classes is still achieved, despite a clear reduction of the spectral information.

The use of those combinations of statistical metrics and spectral indices to feed various kind of classification were explored in more detail in WP33 and 34 reports [AD08, AD09]. With this method, a time series of 19 images with ten spectral bands each, totalling 190 bands, can be reduced to a concatenation of four statistical metrics for the NDBI and as many for the NDVI, totalling only eight bands, while still achieving comparable results in term of spectral separability.

### 4.3.3 Candidate approaches for spectral, spatial, temporal interpolation and/or fusion approaches

S-3 daily surface reflectance (S-3 synergy product combining SLSTR and OLCI observations) is required to fill the gaps in S-2 time series. However, since S-3 data were not ready for productive use during the project duration [AD06] the integration of S-2 and S-3 in the project has been partially tested by using PROBA-V data instead.

On the WEST test site, 24 Proba-V bi-monthly synthesis of NDVI at 100m have been tested as a complement to the S-2 time series NDVI. Therefore, only one channel is being calibrated in this test.

Following the method described in section 3.3.1.3, an histogram matching is realized. The Xcalib library was used to linearly calibrate Proba-V on S-2. To achieve this goal, 2 close acquisition dates of Proba-V and S-2 have been chosen manually. Then, the Xcalib tool has been applied to obtain the Proba-V calibration model. Finally, this model is applied to calibrate all other Proba-V images. Histogram matching results can be found in Figure 4-20. Calibrated image results can be found in Figure 4-21.

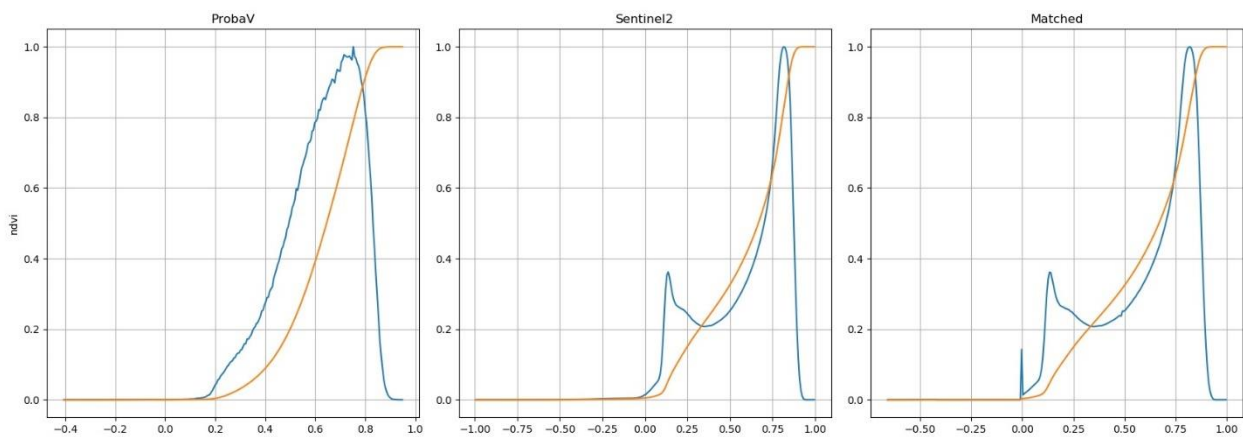


Figure 4-20: Illustration of histogram matching based intercalibration of Proba-V/S-2 for 2 adjacent acquisition dates: (left) Proba-V NDVI histogram, (center) S-2 NDVI histogram, and (right) calibrated Proba-V NDVI histogram

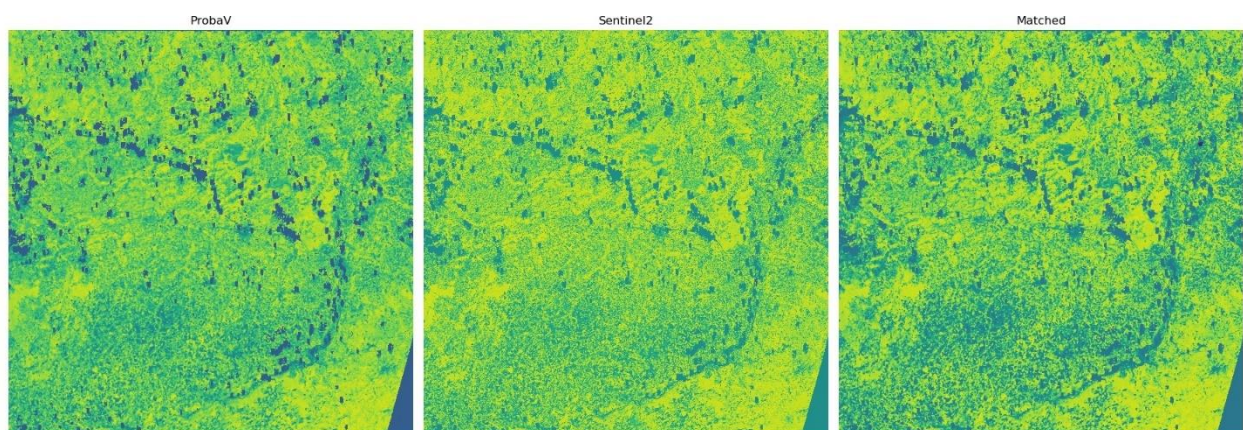


Figure 4-21: Calibrated images of Proba-V/S-2 (left) Proba-V NDVI image, (center) S-2 NDVI image, and (right) calibrated Proba-V NDVI image

Based on visual interpretation, conclusion have been made that even if intercalibration of Proba-V and S-2 data is feasible and accurate, the improvement does not bring enough information to justify the use of

such MR images. Indeed, the probabilities of clear view acquisitions with S-2 is very high (with a revisit time of 2 to 3 days) and even if Proba-V, or other MR sensors, could improve that probabilities (with a daily or less revisit time), the lower resolution will not give sufficient improvement compared to S-2 temporal gap-filling method by interpolation finally selected to generate the prototypes.

For the majority of the prototype, the use of carefully selected S-1 features is far more cost-effective and beneficial to improve the optical classification results and/or fill gaps left by clouds.

## 5 Data requirements and methods used by ECoLaSS application domain

The ECoLaSS project aimed at making full use of dense SAR and optical time-series data for all current and potential future implementations of Copernicus High Resolution Layers. Wherever expected helpful, S1 and S2 data were used in combination. This chapter provides a high-level summary of the experiences made in prototype development and production. In particular, where applicable, it answers the question on how much added value could be achieved by combining S-1 and S-2 data. Each section summarizes also the methods used, as listed in table Table 5-1.

Table 5-1: Classification of the types of methods used during prototype production.

Code	Method	Method Example	Prototype Example
UC	Unsupervised Classification	Clustering proximity groups in feature space	Max Phenological Activity
IND	Indicator	Directly derived indicator from RS data	Crop Emergence Date
SC	Supervised Classification	random forest classification based on ground truth training data	Grassland Status Layer
RBC	Rule-based classification without training data	User-defined thresholds on time-series to identify changes	HRL Time Series Change Indicators
PC	Post classification comparison	Change detection	Tree Cover Change

### 5.1 WP41 Time-series derived indicators & variables

Time-series derived indicators and variables derived by the ECoLaSS project focused on characterizing specific vegetation properties as described in [AD11] “Prototype Report: Time Series Analysis for Change Detection”. See Table 5-2 for the overview over data used and methods applied. They are based on theoretical considerations without further in-situ training data; hence they depend on direct interpretability as opposed to supervised classification approaches which rely on statistical relationships. For this reason each prototype in WP41 on its own made use of either optical or SAR data, but not both at the same time. Crop growth condition and emergence date detection rely strongly on the phenological dynamics of photosynthetic processes, and therefore used optical data, while the potential change indicators aimed at structural changes and therefore relied on SAR data.

Table 5-2: WP41 prototype summary. Data, Sites and Methods used as described in Table 5-1.

Prototype	Input Data				Method	Training data	Demosite
	S-1	S-2	S-1 + S-2	Other			
Generic Landcover Metrics		X			UC + IND	NA	South-West, Central
Emergence Date Detection		X			IND	NA	South-Africa
Crop Growth Condition		X			IND	NA	West
Time Series Indicators – HRL potential change	X				RBC, IND	NA	West, Central

### 5.1.1 Generic Land Cover Metrics

The Proba-V/S-2 time series did not fill all gaps left by clouds – therefore decision was made to use interpolation between S-2 images at fixed dates, generating 2 dates per month in order to create gapless NDVI time series over the demonstration sites, while smoothing potential anomalies such as undetected clouds. This dense time series allows the automation for the computation of phenological activities parameters via a clustering of pixels by a K-means followed by the use of TIMESAT algorithm.

### 5.1.2 Potential Change Indicators

The potential change time-series indicator prototypes (TSI) are based on long-term SAR time-series only. The indicators focus in particular on long-term time-series changes of structural properties. In particular this concerns changes in forest canopies. For this reason S-1 was the ideally suited dataset due to its sensitivity to geometric properties and changes therein as well as the temporally gapless time-series acquisition unaffected of cloud-cover. S-2 was therefore not applicable for this indicator.

## 5.2 WP42 Incremental Updates of HR Layers

For the prototype productions regarding the incremental updates of HR layer domains imperviousness and forests, in almost all cases, both S-1 and S-2 were used in combination (Table 5-3) after initial testing in phase I had highlighted the advantages of this approach. Only in case of the TCD the input-data is restricted to optical only, since it is technically not possible to derive the density from radar data. One overarching finding is that optical data generally achieve higher accuracies in the classifications than it is the case for radar data. However, the presence of a high percentage of cloud cover makes the combination of optical and radar sensors indispensable. In section 5.2.1 details are given for the testing related to the imperviousness prototypes whereas further explanations for the Forest related prototypes are given in section 5.2.2.

Table 5-3: WP42 prototype summary. Data, Sites and Methods used as described in Table 5-1.

Prototype	Input Data				Method	Training data	Demosite
	S-1	S-2	S-1 + S-2	Other			
Improved IMD status layer (10m)			X		SC	HRLs 2015	Central, South-West, South-East
Incremental IMD change (IMC)			X		PC	HRLs 2015	Central, South-West, South-East
Imperviousness Change Classified (IMCC)			X		PC	HRLs 2015	Central, South-West, South-East
Imperviousness Built-Up Layer			X		SC	ESM, OSM	Central, South-West, South-East
Improved DLT status layer (10m)			X		SC	HRLs 2015	North, Central, South-East
Improved TCD status layer (10m)		X			SC	HRLs 2015	North, Central, South-East
Incremental Update Tree Cover Change (TCC)			X		RBC		North, Central, South-East

### 5.2.1 Imperviousness

The automated supervised classification used to derive the Imperviousness layers was performed using supervised machine learning methods, achieved with a selection of reference/training data. The input data selected rely on multispectral information and granulometry by mathematical morphology (Differential Attribute Profiles).

Regarding the HRL IMD production the optical series were not dense enough to highlight the inter-yearly and intra-yearly phenology dynamics in order to highlight non-urban areas and so it was decided to use S-1 time series and features. The combination of S-1/S-2 shows promising results with very good thematic accuracies. The additional SAR data improves the thematic classification of various classes including the urban areas as they react to physical structures of the scattering elements. Nevertheless, the addition of S-1 doesn't lead to large and significant improvements of the results as demonstrated in phase 1 but permits to have better balance thematic accuracies (Table 5-4). Indeed, in one hand, the use of S-1 permits to reduce the commission errors. In the other hand, the omission errors are greater but are still above the specification's thresholds. Moreover, it has been shown that the only use of S-1 data is not sufficient to characterize the urban areas.

**Table 5-4: Comparative training accuracies of the imperviousness testing achieved by using either a) S-1 only, b) S-2 only and c) S-1 plus S-2 predictors.**

Site	PA			UA		
	S-1	S-2	S-1 + S-2	S-1	S-2	S-1 + S-2
2017						
South-West	77.78%	88.89%	85.19%	72.41%	70.59%	74.19%

Based on the outcomes of phase 1, a multi-sensor approach combining S-1 and S-2 data was adopted in phase 2 providing increased accuracies of the results. For the imperviousness prototypes of phase 2 no single-sensor accuracies have thus been assessed but **Table 5-4** shows the accuracy results for the SVM classification of phase 1 for comparison. **Table 5-6** and **Table 5-7** display the final prototype performances based on the selected S-1 and S-2 predictor combination.

**Table 5-5: Area-weighted accuracies of IMD 2018 achieved by fusion of S-1 plus S-2**

Site	OA	PA for sealed / Non-sealed	UA for sealed / Non-sealed
South-West	97.03%	91.74% / 97.59%	80.21% / 99.11%
Central	99.11%	94.76% / 99.56%	95.70% / 99.46%
South-East	99.41%	91.42% / 99.67%	86.37% / 99.81%

**Table 5-6: Area-weighted accuracies of IMCC 2015/17-18 achieved by fusion of S-1 plus S-2**

Site	OA	PA for New Built-up class	UA for New Built-up class
South-West	99.68%	98.24%	97.29%
Central	98.37%	87.55%	100.00%
South-East	99.58%	60.82%	100.00%

**Table 5-7: Area-weighted accuracies of IBU 2018 by fusion of S-1 plus S-2**

Site	OA	PA for Built-up / Non-Built-up	UA for Built-up / Non-Built-up
South-West	99.21%	94.74% / 99.35%	81.82% / 99.84%
Central	98.64%	92.86% / 99.06%	87.84% / 99.48%
South-East	99.45%	92.86% / 99.58%	81.25% / 99.86%

### 5.2.2 Forest

A pixel-based Tree Cover Mask (TCM) forms the basis for all other forest products and thus represents the first step in the thematic workflow. The Random Forest (RF) classifier has been selected as the best rated classification algorithm in terms of processing time and achieved accuracy for creation of the Tree Cover Mask and the improved primary status layer Dominant Leaf Type (DLT). The forest change products are based on a map-to-map change detection method, which is fully detached from the input data used for the TCM generation and therefore completely independent from the input data applied for production. Same as for imperviousness, the outcomes from phase 1 suggested that a combined use of S-1 and S-2 in combination with an extended observation period yields the best results in terms of accuracies. For forest change analysis, however, the difference to S-2 only is relatively low, when taking a good data situation into account (see Table 5-11). However, since a good data situation cannot always be guaranteed especially when implementing the products on a pan-European scale, the combined use of S-1 and S-2 is preferred over the single-sensor approach.

**Table 5-8: Accuracies of TCM achieved by fusion of S-1 plus S-2**

Site	OA	PA for tree cover / no tree cover	UA for tree cover / no tree cover
North 2017	89.94%	87.71% / 91.73%	89.49% / 90.29%
North 2018	94.40%	90.71% / 97.60%	97.03% / 92.38%
Central 2017	93.82%	88.29% / 95.34%	83.89% / 96.74%
Central 2018	98.11%	93.59% / 99.23%	96.76% / 98.43%
South-East 2017	90.53%	70.70% / 96.95%	88.24% / 91.08%
South-East 2018	96.75%	89.28% / 98.83%	95.47% / 97.08%

**Table 5-9: Accuracies of the forest DLT status layer 2018 achieved by fusion of S-1 plus S-2**

Site	OA	PA for no tree cover / broadleaved / coniferous	UA for no tree cover / broadleaved / coniferous
North	92.78%	97.60% / 84.23% / 88.89%	92.38% / 89.64% / 95.35%
Central	97.80%	99.23% / 87.76% / 97.17%	98.43% / 93.61% / 96.87%
South-East	95.83%	98.83% / 83.04% / 90.18%	97.08% / 91.95% / 88.60%

**Table 5-10: Accuracies of the TCC 2017-2018 achieved by fusion of S-1 plus S-2**

Site	OA	PA for forest loss	UA for forest loss
North	94.34%	95.54%	96.77%
Central	96.81%	98.21%	96.48%
South-East	96.78%	100.00%	80.26%

**Table 5-11: Benchmarking criteria, chances and issues of the different input data scenarios of TCC\***

	Accuracy (Kappa)	Processing cost	Storage cost	Chances	Issues
<b>S-1</b>	0.60	+	+	Independent from cloud cover	SAR inherent properties (foreshortening, layover in strong relief, speckle)
<b>S-2</b>	0.74	++	+++	Dependent on cloud cover, but time features mitigate problematic areas	Clouds/cloud shadows, artefacts, nodata gaps
<b>S-1 S-2</b>	0.77	+++	++++	Partially dependent on cloud cover, but SAR and S-2 time features mitigate problematic areas	Clouds/cloud shadows, artefacts, SAR inherent properties (foreshortening, layover in strong relief, speckle)
<b>Kalman</b>	0.86	++	++	Once the system is initialized, historic images are no longer required and new images are processed one-at-a-time. Despite only using optical data, the principle of change confirmation reduces the number of false alarms due to errors of the cloud mask.	Long time series required in the beginning to set up a meaningful time series model and initialize the Kalman filter state. This might fail in areas with extremely low number of clear-sky observations and/or persistent snow cover. At least 3 post-change observations are required to detect and confirm a change – this can lead to cases where changes occurring at the end of the year cannot be confirmed in the same year.

\* Benchmarking takes only the data scenarios into account

### 5.3 WP 43 Improved Permanent Grassland Identification

The objective of WP43 is the deployment and validation of improved classification methods for grassland mapping developed in WP33 using time series of S-1 and S-2 data. Results are derived focusing on (i) the

background of CLMS grassland monitoring needs and requirements, (ii) optimising time series analysis methods based on the results and recommendations of WP 33 “Time Series Analysis for Thematic Classification” (iii) multi-sensor data integration methods, the use of multi-temporal time series metrics, the random forest classification approach and (iv) the validation of the prototype results. To demonstrate the operational applicability of the methods, they were applied on representative demonstration sites for large area mapping. The “Alpine/Central Europe” demonstration site is representative for the Continental and Alpine bio-geographic region, the “West Europe” site for the Atlantic and Continental, and the “South-East Europe” site for the Mediterranean, Continental and Alpine bio-geographic regions.

Permanent grassland identification was accomplished by a supervised classification with the Random Forest algorithm using both S-1 and S-2 predictors in isolation or in combination. It was found that the combination of S-1 and S-2 time-series derived predictors outperformed each single predictor set.

**Table 5-12 Data and methods used for Grassland prototype production. See Table 5-1 for the legend of different classification methods.**

PROTOTYPE	REMOTE SENSING DATA				METHOD	TRAINING & REFERENCE DATA	SITE
	S-1	S-2	S-1 + S-2	Other			
<b>GRASSLAND STATUS</b>	X	X	X		SC	LUCAS 2018 HRL GRA 2015	Central, West, South-East
<b>GRASSLAND CHANGE</b>			X		PC	HRL GRA 2015	Central, West, South-East
<b>GRASSLAND USE INTENSITY</b>		X			RBC		Central, West, South-East

### **Quantitative Comparison of Performance**

The accuracies achieved during model training for the Grassland status layer classification for either a) S-1 only, b) S-2 only and c) S-1 plus S-2 predictors are summarized in **Table 5-13**. These tests on the synergetic use of temporal features derived from optical and SAR data streams shows a notable improvement in model accuracy of the classifications in comparison to either single optical or SAR only approaches. While in all cases S-2 predictors were found to be superior to S-1 predictors, maximum performance was only obtained when combining both S-1 and S-2 by means of pixel-level fusion.

**Table 5-13 Comparative training accuracies (overall, producer’s and user’s accuracies) of the grassland status layer classification achieved by using either a) S-1 only, b) S-2 only and c) S-1 plus S-2 predictors and LUCAS 2018 plots.**

SITE	OA			PA			UA		
	S1	S2	S1 + S2	S1	S2	S1 + S2	S1	S2	S1 + S2
<b>CENTRAL</b>	N/A	N/A	82.32%	N/A	N/A	92.21%	N/A	N/A	71.00%
<b>WEST</b>	77.80%	85.78%	86.74%	65.94%	80.35%	83.41%	71.23%	80.70%	80.93%
<b>SOUTH-EAST</b>	81.79%	83.85%	88.50%	40.30%	45.13%	66.51%	62.79%	70.81%	73.26%

While processing both S-1 and S-2 data for a potential pan-European rollout certainly entails a non-negligible processing overhead, these results demonstrate the added value of doing so. An advantage of the proposed pixel-level fusion approach with a very high number of potential candidate predictors is that these can be tailored to different geographic regions by fully automated feature selection. This was accomplished in [AD13], resulting in optimal but different predictor sets for different regions, while reducing the feature space dimensionality to moderate sizes in the range of 50 to 100 predictors.

Overall, the S-1 SAR features were much more stable which is likely due to their more consistent time-series, which are barely influenced by cloud cover and illumination effects. Therefore, the combined S1/S2 approach has been chosen for the prototype production, where additional post-processing steps are applied to improve the results. The final area weighted validation of the improved grassland HRL status layer prototypes for the year 2018, i.e. corresponding to the LUCAS reference year 2018, is summarized in Table 5-14. For the complete quantitative validation numbers, refer to [AD13].

**Table 5-14 Summary of the final grassland status layer mapping accuracy for the reference year of LUCAS training data (2018) following the area-weighted plausibility validation. For the full validation refer to [AD13].**

SITE	PREDICTORS		ACCURACY		
	S-1	S-2	OA	UA	PA
<b>CENTRAL</b>	X	X	96.63%	90.55%	91.02%
<b>WEST</b>	X	X	98.39%	96.28%	96.25%
<b>SOUTH-EAST</b>	X	X	97.14%	94.03%	82.95%

The prototype production showed a high level of automation allowing a faster production and shorter monitoring intervals (e.g. continuous monitoring with yearly updates). Further the S-2 and S-1 time series are fully exploited instead of using pre-selected, best-suited optical EO data scenes. Therefore, the workflow integrates SAR/optic time series data analysis to benefit from the multi-sensor characteristics with 10m resolution.

**Conclusion:**

As evident from intensive predictor testing, the Grassland HRL production benefits strongly from the combination of S-1 and S-2 time-series predictors. The pursued approach of a supervised random forest classification has proven to produce very high accuracies, even based on the comparatively sparse LUCAS training data. The high number of potential candidate features can be reduced by automated feature selection algorithms, which allows accounting for region specific differences in predictor importance. Looking beyond this demonstration of methods and predictor requirements for HRL grassland mapping, an operational implementation and roll-out of area-wide, yearly grassland mapping using S-1 and S-2 time-series predictors is clearly recommendable.

**5.4 WP 45 New LC/LU Products**

The WP45 is centred around the creation of two new types of LC/LU product, both related to the evolution of CLC toward the next generation CLC+ datasets, as described in [AD14] “Prototype Report: New Land Cover/Land Use (LC/LU) Products” (see Table 5-15). The first type of product, based on the recent specifications of CLC+ Backbone, uses S-2 time series to create a raster classification that is then fused with a skeleton layer based on a segmentation and ancillary data to produce a more detailed vector layer, following sets of rules in the attribution of class to polygon. The segmentation has been derived from the Generic Landcover Metrics layer, using therefore unsupervised classification and spectral indices from the S-2 time series. The second type of product is, for now, more closely related to the CLC+ Core, as drafted in the new CLC+ specifications. The combination of HRLs (from the 2015 datasets as well as phase 1 prototypes) is derived from rule-based prioritisation to try and enforce a spatially and temporally coherence in the final product.

**Table 5-15 Data and methods used for the New LC/LU prototype production. See Table 5-1 for the legend of different classification methods.**

PROTOTYPE	REMOTE SENSING DATA				METHOD	TRAINING & REFERENCE DATA	SITE
	S-1	S-2	S-1 + S-2	Other			
<b>CLC+ RASTER PRODUCT</b>		X			SC	HRL2015, CLC2018	Central, South-West
<b>CLC+ VECTOR PRODUCT</b>		X		X	SC, UC + IND	Open Street Map, EU-Hydro, HRL2015, CLC2018	Central, South-West
<b>HR COMBINED LAYER</b>				X	Other	HRL2015	Central, West, South-West

**Table 5-16 Summary of the New LC/LU raster status layer mapping accuracy for the reference year of CLC training data (2018) following the area-weighted plausibility validation. For the full validation refer to [AD14].**

SITE	PREDICTORS		OA	ACCURACY		
	S-1	S-2		Class	UA	PA
<b>CENTRAL</b>		X	91.08%	Urban	88.51%	88.14%
		X		Croplands	96.45%	88.53%
		X		Grasslands	91.14%	93.32%
		X		Shrubs	35.71%	91.38%
		X		Broadleaved	89.25%	95.51%
		X		Needle-leaved	98.30%	89.95%
		X		Rock	80.95%	85.03%
		X		Snow	90.91%	73.33%
		X		Water	96.67%	88.56%
	<b>SOUTH-WEST</b>			X	91.99%	Urban
		X	Croplands	89.95%		95.30%
		X	Grasslands	94.05%		90.26%
		X	Shrubs	84.09%		87.12%
		X	Broadleaved	95.22%		93.03%
		X	Needle-leaved	91.99%		89.26%
		X	Rock	95.99%		97.27%
		X	Sand	100%		100%
		X	Snow	100%		90.91%
		X	Water	94.12%		100%

Both raster classification shows excellent results (see **Table 5-16**) – however, a selection of the classes has been made to remove the most confusing classes, such as lichens and mosses or sparsely vegetated cover, whose sampling remains difficult with the datasets currently at hand.

**Table 5-17 Summary of the New LC/LU vector status layer mapping accuracy for the reference year of CLC training data (2018) following the area-weighted plausibility validation. For the full validation refer to [AD14].**

SITE	PREDICTORS		OA	ACCURACY		
	S-1	S-2		Class	UA	PA
<b>CENTRAL</b>		X	81.03%	Woody Shrubs	71.21%	62.69%
		X		Periodically Herbaceous	97.79%	88.93%
		X		Non-Vegetated	100%	28.29%
		X		Very High Sealing Degree	100%	66.81%
		X		High sealing Degree	69.13%	100%
		X		Pure Needle-leaved	97.61%	75.76%
		X		Dominantly Needle-leaved	69.41%	81.05%
		X		Pure Broadleaved	95.10%	86.18%
		X		Dominantly Broadleaved	0%	91.99%
		X		Snow & Ice	0%	0%
		X		Water	93.80%	88.20%
		X		Permanently Herbaceous Without Trees	93.74%	79.08%
		X		Permanently Herbaceous With Few Trees	73.93%	98.19%
		X		Permanently Herbaceous With Many Trees	66.67%	75.78%
		X		Intermediate Vegetation Cover	50%	100%
		X		Low Vegetation Cover	0%	0%
	X		Other	0%	0%	
<b>SOUTH-WEST</b>		X	76.24%	Woody Shrubs	80.02%	73.90%
		X		Periodically Herbaceous	96.75%	84.19%
		X		Non-Vegetated	100%	20.12%
		X		Very High Sealing Degree	100%	56.06%
		X		High sealing Degree	41.97%	100%
		X		Pure Needle-leaved	100%	74.52%
		X		Dominantly Needle-leaved	81.71%	65.83%
		X		Pure Broadleaved	96.70%	85.94%
		X		Dominantly Broadleaved	7.29%	100%
		X		Snow & Ice	43.57%	28.57%
		X		Water	98.59%	93.33%
		X		Permanently Herbaceous Without Trees	90.28%	67.97%
		X		Permanently Herbaceous With Few Trees	94.71%	89.98%
		X		Permanently Herbaceous With Many Trees	80.01%	100%
		X		Intermediate Vegetation Cover	0%	0%
		X		Low Vegetation Cover	0%	0%
	X		Other	0%	0%	

The vector products validation is less convincing (see Table 5-17). This can be linked to the quality of the segmentation, whose methodology does not take into account the bioregional disparities nor the complexities of non-vegetated activity classes.

It should be noted that following the CLC+ Invitation To Tender (ITT), only S-2 interpolated times series have been used to generate the soft bones of the vector product, i.e. the segmentation, and those input datasets have then been reuse to produce the classification of the raster product.



## 6 Conclusions and Outlook

The aim of this report was to develop and test integration strategies for S-1, S-2 and S-3 data allowing benefiting from their complementary multi-resolution, multi-temporal and multi-sensor characteristics based on state-of-the-art methods of investigated S-1/-2/-3 integration strategies. Therefore, the objective of WP 31 was to investigate the possibilities of combining S-1, S-2 and S-3 data with regards to the envisaged evolution of Copernicus Land Services addressed in ECoLaSS. This aim was appended following the review recommendations in that the benchmarking of methods should become part of WPs 32-35 [AD07-AD10], whereas this report should summarize the data requirements and methods used during ECoLaSS prototype production in Task 4 WPs 41-25. Given that due to the missing S-3 readiness, all prototypes were based on S-1 and S-2 data, but not S-3 data, the issue of time-series fusion with coarse resolution sensors was not explored in the aforementioned WPs. Therefore, this report adds a substitute test for data-fusion of S-2 with PROBA-V in addition.

The first issue of this report [AD05] mainly focussed on the analysis of State-of-the-Art methods and strategies for the integration of S-1, S-2 and S-3 data and gave first concepts for possible strategies for the integration and/or fusion for the different HRL classifications. These have been updated in this second issue of the report. Further additions were made by introducing S-2 / PROBA-V time-series fusion tests, followed by a high-level summary of all prototype developments made during the ECoLaSS project, paying particular attention to the data integration, the relative suitability and the complementarity of S-1 and S-2 data.

Regarding the integration of S-1/S-2, the information gained from both sensors is used in parallel for the classification as they record complementary characteristics of the land surface. While optical data are affected by the physical-chemical characteristics of the surface (such as leaf structure or pigmentation) SAR data represent the geometric and dielectric properties of the surface (Woodhouse, 2006). Through their multi-spectral bands ranging from visible to near infrared wavelengths, optical data provide information on diverse land covers. SAR data on the other hand are usually acquired in a single frequency for each sensor and interact with the structural characteristics of the surface depending on the wavelength, incidence angle of the sensor, as well as roughness and moisture content. Here, two different methods are proposed for the integration of the S-1/S-2 data: (a) the fusion on pixel level: bands and indices from S-1 and S-2 are stacked into one dataset, which are the target of the classification; and (b) the fusion on decision level: classification of individual land cover classes are performed based on S-1 data or S-2 data individually and the results are fused based on decision rules on post-classification level. Therefore, sets of indicators and metrics derived from time series of SAR and optical data are currently being used in the literature, which can also be derived from S-1 or S-2 data. The following indicators from optical and SAR data have been identified based on the state-of-the-art analysis of being useful and improving the thematic classification results: NDVI, NDBI, MNDWI, NDMIR, NDRB, as well as NDGB derived from S-2 data and the backscatter coefficients in the VV and VH polarisations and polarisation ratios VH/VV derived from S-1 data. Qualitative assessment showed that the complementary information derived from S-1 data in addition to those from the optical data of S-2 are promising in helping to distinguish between urban areas and bare soil. Moreover, also a sub-classification of urban areas seems possible as one can clearly distinguish between inhabited and industrial areas. Also, forests and grassland areas can be visually distinguished better by using the fused data sets.

The major drawback of optical observations is the impossibility for any sensor to permeate opaque clouds, whose presence can greatly vary from one AOI to the other. The fusion of S-2 and S-3 data is expected to bring down the revisit time from five days (for S-2) to one day, helping to densify the time series (Sylla et al., 2014). However, as noticed in current HRL projects, supplemental observations (from other sensors or on an extended span of several years) often have to be required in order to fill the gaps left by clouds. To monitor slow changes, such as the urban growth, temporal metrics derived from

spectral indices, such as extrema, standard deviation and median of the NDBI and NDVI, computed over a year, seem to be qualitatively as satisfactory as full datasets of raw images to characterize the land cover image by image, before proceeding to fusion on decision level. Nonetheless, to follow crop and grassland evolution in the landscape, future research will investigate in further details temporal techniques, such as temporal interpolation, to create composites based on the previous and following cloudless images in the time series, or trend modelling, that fill gaps as well as discriminate outliers, or diminish the effect of random noise.

Throughout the ECoLaSS project a wide variety of methods were tested and employed for prototype production in a wide variety of application domains, ranging from data-centric statistical indicators, expert-defined decision trees and unsupervised clustering to supervised classifications and post-classification comparisons. The predominant method for HRL production was supervised classification based on ground-truth training data. The algorithm of choice in most cases was the non-parametric Random Forest classifier.

The data requirements established through extensive testing in both project phases resulted in a very clear picture. In almost all cases a significant improvement in mapping accuracy could be achieved by exploiting both optical S-2 data and SAR S-1 data in combination. This was the case for imperviousness, forest and grassland mapping. Fully automated strategies for feature selection, allow tailoring the optimal set of predictors from a large pool of potential candidates, hence allowing regionally optimized mapping in different geographic regions.

Nevertheless, also a case for single source predictors could be made for time-series indicators, which are based on theoretical considerations, and therefore depend on the interpretability of the remote sensing data as opposed to supervised classification approaches, which can rely on statistical relationships not readily apparent to the human mind. For this reason each prototype on its own made use of either optical or SAR data, but not both at the same time. Crop growth condition, emergence date detection, and grassland use intensity mapping for example, are based on the phenological dynamics of photosynthetic processes, and therefore relied only on optical data of vegetation state. Contrastingly, potential change time-series indicators aimed at detecting structural changes and outliers relied on SAR data only.

Overall, the ECoLaSS project has demonstrated the enormous potential for information extraction from combining multiple sensors and sensor constellations provided by the Copernicus Sentinel fleet, which exceeds all expectations and is almost guaranteed to boost the evolution of operational Copernicus HRL production in terms of both mapping accuracy and novel HRL products.

## 7 References

- Alparone, L., Baronti, S., Garzelli, A., & Nencini, F. (2004). A global quality measurement of pan-sharpened multispectral imagery. *Ieee Geoscience and Remote Sensing Letters*, 1(4), 313-317. doi:<https://doi.org/10.1109/LGRS.2004.836784>
- As-Syakur, A. R., Adnyana, I. W. S., Arthana, I. W., & Nuarsa, I. W. (2012). Enhanced Built-Up and Bareness Index (EBBI) for Mapping Built-Up and Bare Land in an Urban Area. *Remote Sensing*, 4(10), 2957. doi:<https://doi.org/10.3390/rs4102957>
- Bach, H., Friese, M., Spannraft, K., Migdall, S., Dotzler, S., Hank, T., Frank, T., & Mauser, W. (2012, 22-27 July 2012). *Integrative use of multitemporal RapidEye and TerraSAR-X data for agricultural monitoring*. Paper presented at the 2012 IEEE International Geoscience and Remote Sensing Symposium.
- Bacour, C., Bréon, F.-M., & Maignan, F. (2006). Normalization of the directional effects in NOAA–AVHRR reflectance measurements for an improved monitoring of vegetation cycles. *Remote Sensing of Environment*, 102(3), 402-413. doi:<https://doi.org/10.1016/j.rse.2006.03.006>
- Baghdadi, N., El Hajj, M., Fayad, I., & Zribi, M. (2015). *Coupling SAR C-Band and Optical Data for Soil Moisture and Leaf Area Index Retrieval Over Irrigated Grasslands* (Vol. 9).
- Balzter, H., Cole, B., Thiel, C., & Schmullius, C. (2015). Mapping CORINE Land Cover from S-1A SAR and SRTM Digital Elevation Model Data using Random Forests. *Remote Sensing*, 7(11), 14876. doi:<https://doi.org/10.3390/rs71114876>
- Bannari, A., Asalhi, H., & Teillet, P. M. (2002). *Transformed Difference Vegetation Index (TDVI) for vegetation cover mapping*. New York: IEEE.
- Baret, F., Guyot, G., & Major, D. J. (1989, 10-14 July 1989). *TSAVI: A Vegetation Index Which Minimizes Soil Brightness Effects On LAI And APAR Estimation*. Paper presented at the Geoscience and Remote Sensing Symposium, 1989. IGARSS'89. 12th Canadian Symposium on Remote Sensing., 1989 International.
- Betbeder, J., Rapinel, S., Corgne, S., Pottier, E., & Hubert-Moy, L. (2015). TerraSAR-X dual-pol time-series for mapping of wetland vegetation. *Isprs Journal of Photogrammetry and Remote Sensing*, 107, 90-98. doi:<https://doi.org/10.1016/j.isprs.2015.05.001>
- Blaes, X., Vanhalle, L., & Defourny, P. (2005). *Efficiency of crop identification based on optical and SAR image time series* (Vol. 96).
- Bogaert, P., & Fasbender, D. (2007). Bayesian data fusion in a spatial prediction context: a general formulation. *Stochastic Environmental Research and Risk Assessment*, 21(6), 695-709. doi:<https://doi.org/10.1007/s00477-006-0080-3>
- Boschetti, L., Roy, D. P., Justice, C. O., & Humber, M. L. (2015). MODIS–Landsat fusion for large area 30m burned area mapping. *Remote Sensing of Environment*, 161, 27-42. doi:<https://doi.org/10.1016/j.rse.2015.01.022>
- Brisco, B., & Brown, R. J. (1995). Multidate SAR/TM Synergism for Crop Classification in Western Canada. *Photogrammetric Engineering and Remote Sensing*, 61(8), 1009-1014.
- Buchhorn, M., Bertels, L., Smets, B., Lesiv, M., & Tsendbazar, N. (2017). Copernicus Global Land Operations “Vegetation and Energy” (CGLOPS-1): Algorithm Theoretical Basis Document. (I1.00).
- Carlson, T. N., & Ripley, D. A. (1997). On the relation between NDVI, fractional vegetation cover, and leaf area index. *Remote Sensing of Environment*, 62(3), 241-252. doi:[https://doi.org/10.1016/S0034-4257\(97\)00104-1](https://doi.org/10.1016/S0034-4257(97)00104-1)
- Chang, J., & Shoshany, M. (2016, 10-15 July 2016). *Mediterranean shrublands biomass estimation using S-1 and S-2*. Paper presented at the 2016 IEEE International Geoscience and Remote Sensing Symposium (IGARSS).
- Chen, C. M., Hepner, G. F., & Forster, R. R. (2003). Fusion of hyperspectral and radar data using the IHS transformation to enhance urban surface features. *Isprs Journal of Photogrammetry and Remote Sensing*, 58(1-2), 19-30. doi:[https://doi.org/10.1016/S0924-2716\(03\)00014-5](https://doi.org/10.1016/S0924-2716(03)00014-5)
- Chust, G., Ducrot, D., & Pretus, J. L. L. (2004). Land cover discrimination potential of radar multitemporal series and optical multispectral images in a Mediterranean cultural landscape. *International*

- Journal of Remote Sensing*, 25(17), 3513-3528.  
doi:<https://doi.org/10.1080/0143116032000160480>
- Clement, M. A., Kilsby, C. G., & Moore, P. (2017). Multi-temporal synthetic aperture radar flood mapping using change detection. *Journal of Flood Risk Management*.  
doi:<https://doi.org/10.1111/jfr3.12303>
- Dotzler, S., Bach, H., Spannrafft, K., Migdall, S., Hank, T., Frank, T., & Mauser, W. (2013). *Leaf area index retrieval and yield modeling for winter wheat with TerraSAR-X data compared to using optical data*. Paper presented at the ESA Living Planet Symposium 2013, Edinburgh, UK.
- Dusseux, P., Corpetti, T., Hubert-Moy, L., & Corgne, S. (2014). Combined Use of Multi-Temporal Optical and Radar Satellite Images for Grassland Monitoring. *Remote Sensing*, 6(7), 6163-6182.  
doi:<https://doi.org/10.3390/rs6076163>
- Erasmí, S. (2013). Habitat Mapping from Optical and SAR Satellite Data: Implications of Synergy and Uncertainty for Landscape Analysis. *Photogrammetrie Fernerkundung Geoinformation*(3), 139-148. doi:<https://doi.org/10.1127/1432-8364/2013/0165>
- Esch, T., Üreyen, S., Zeidler, J., Metz-Marconcini, A., Hirner, A., Asamer, H., Tum, M., Böttcher, M., Kuchar, S., Svaton, V., & Marconcini, M. (2018). Exploiting big earth data from space – first experiences with the timescan processing chain. *Big Earth Data*, 1-20.  
doi:<https://doi.org/10.1080/20964471.2018.1433790>
- Fasbender, D., Obsomer, V., Bogaert, P., & Defourny, P. (2009). Updating Scarce High Resolution Images with Time Series of Coarser Images: a Bayesian Data Fusion Solution. In N. Milisavljevic (Ed.), *Sensor and Data Fusion* (pp. 245-262).  
[https://www.intechopen.com/books/sensor\\_and\\_data\\_fusion/updating\\_scarce\\_high\\_resolution\\_images\\_with\\_time\\_series\\_of\\_coarser\\_images\\_a\\_bayesian\\_data\\_fusion\\_so](https://www.intechopen.com/books/sensor_and_data_fusion/updating_scarce_high_resolution_images_with_time_series_of_coarser_images_a_bayesian_data_fusion_so): InTech.
- Fasbender, D., Obsomer, V., Radoux, J., Bogaert, P., & Defourny, P. (2007, 18-20 July 2007). *Bayesian Data Fusion: Spatial and Temporal Applications*. Paper presented at the 2007 International Workshop on the Analysis of Multi-temporal Remote Sensing Images.
- Fasbender, D., Radoux, J., & Bogaert, P. (2008a). Bayesian Data Fusion for Adaptable Image Pansharpening. *Ieee Transactions on Geoscience and Remote Sensing*, 46(6), 1847-1857.  
doi:<https://doi.org/10.1109/TGRS.2008.917131>
- Fasbender, D., Tuia, D., Bogaert, P., & Kanevski, M. (2008). Support-Based Implementation of Bayesian Data Fusion for Spatial Enhancement: Applications to ASTER Thermal Images. *Ieee Geoscience and Remote Sensing Letters*, 5(4), 598-602. doi:<https://doi.org/10.1109/LGRS.2008.2000739>
- Ferrant, S., Selles, A., Le Page, M., Herrault, P.-A., Pelletier, C., Al-Bitar, A., Mermoz, S., Gascoin, S., Bouvet, A., Saqalli, M., Dewandel, B., Caballero, Y., Ahmed, S., Maréchal, J.-C., & Kerr, Y. (2017). Detection of Irrigated Crops from S-1 and S-2 Data to Estimate Seasonal Groundwater Use in South India. *Remote Sensing*, 9(11), 1119. doi:<https://doi.org/10.3390/rs9111119>
- Frampton, W. J., Dash, J., Watmough, G., & Milton, E. J. (2013). Evaluating the capabilities of S-2 for quantitative estimation of biophysical variables in vegetation. *Isprs Journal of Photogrammetry and Remote Sensing*, 82, 83-92. doi:<https://doi.org/10.1016/j.isprsiprs.2013.04.007>
- Franklin, S. E., Ahmed, O. S., Wulder, M. A., White, J. C., Hermosilla, T., & Coops, N. C. (2015). Large Area Mapping of Annual Land Cover Dynamics Using Multitemporal Change Detection and Classification of Landsat Time Series Data. *Canadian Journal of Remote Sensing*, 41(4), 293-314.  
doi:<https://doi.org/10.1080/07038992.2015.1089401>
- Freeman, A., & Durden, S. L. (1998). A three-component scattering model for polarimetric SAR data. *Ieee Transactions on Geoscience and Remote Sensing*, 36(3), 963-973.  
doi:<https://doi.org/10.1109/36.673687>
- Furby, S., Caccetta, P., Wu, X., & Chia, J. (2008). *Continental scale land cover change monitoring in Australia using Landsat imagery*. Paper presented at the International Earth Conference: Studying, Modeling and Sense Making of Planet Earth, Mytilene, Lesvos, Greece.
- Gao, B.-C. (1996). NDWI—A normalized difference water index for remote sensing of vegetation liquid water from space. *Remote Sensing of Environment*, 58(3), 257-266.  
doi:[https://doi.org/10.1016/S0034-4257\(96\)00067-3](https://doi.org/10.1016/S0034-4257(96)00067-3)

- Gao, F., Hilker, T., Zhu, X. L., Anderson, M. C., Masek, J. G., Wang, P. J., & Yang, Y. (2015). Fusing Landsat and MODIS Data for Vegetation Monitoring. *Ieee Geoscience and Remote Sensing Magazine*, 3(3), 47-60. doi:<https://doi.org/10.1109/Mgrs.2015.2434351>
- Gao, F., Masek, J., Schwaller, M., & Hall, F. (2006). On the blending of the Landsat and MODIS surface reflectance: Predicting daily Landsat surface reflectance. *Ieee Transactions on Geoscience and Remote Sensing*, 44(8), 2207-2218. doi:<https://doi.org/10.1109/Tgrs.2006.872081>
- Gao, Q., Zribi, M., Escorihuela, M. J., & Baghdadi, N. (2017). Synergetic Use of S-1 and S-2 Data for Soil Moisture Mapping at 100 m Resolution. *Sensors*, 17(9). doi:<https://doi.org/10.3390/s17091966>
- Gengler, S., & Bogaert, P. (2018). Combining land cover products using a minimum divergence and a Bayesian data fusion approach. *International Journal of Geographical Information Science*, 32(4), 806-826. doi:10.1080/13658816.2017.1413577
- Haas, J., & Ban, Y. (2017). S-1A SAR and S-2A MSI data fusion for urban ecosystem service mapping. *Remote Sensing Applications: Society and Environment*, 8, 41-53. doi:<https://doi.org/10.1016/j.rsase.2017.07.006>
- Hagolle, O., Dedieu, G., Mougenot, B., Debaecker, V., Duchemin, B., & Meygret, A. (2008). Correction of aerosol effects on multi-temporal images acquired with constant viewing angles: Application to Formosat-2 images. *Remote Sensing of Environment*, 112(4), 1689-1701. doi:<https://doi.org/10.1016/j.rse.2007.08.016>
- Hagolle, O., Huc, M., Pascual, D. V., & Dedieu, G. (2010). A multi-temporal method for cloud detection, applied to FORMOSAT-2, VEN mu S, LANDSAT and S-2 images. *Remote Sensing of Environment*, 114(8), 1747-1755. doi:<https://doi.org/10.1016/j.rse.2010.03.002>
- Hagolle, O., Huc, M., Pascual, D. V., & Dedieu, G. (2015). A Multi-Temporal and Multi-Spectral Method to Estimate Aerosol Optical Thickness over Land, for the Atmospheric Correction of FormoSat-2, LandSat, VEN mu S and S-2 Images. *Remote Sensing*, 7(3), 2668-2691. doi:<https://doi.org/10.3390/rs70302668>
- Hansen, M. C., Egorov, A., Potapov, P. V., Stehman, S. V., Tyukavina, A., Turubanova, S. A., Roy, D. P., Goetz, S. J., Loveland, T. R., Ju, J., Kommareddy, A., Kovalsky, V., Forsyth, C., & Bents, T. (2014). Monitoring conterminous United States (CONUS) land cover change with Web-Enabled Landsat Data (WELD). *Remote Sensing of Environment*, 140, 466-484. doi:<https://doi.org/10.1016/j.rse.2013.08.014>
- Haralick, R. M., Shanmugam, K., & Dinstein, I. (1973). Textural Features for Image Classification. *IEEE Transactions on Systems, Man, and Cybernetics*, SMC-3(6), 610-621. doi:<https://doi.org/10.1109/TSMC.1973.4309314>
- Hilker, T., Wulder, M. A., Coops, N. C., Linke, J., McDermid, G., Masek, J. G., Gao, F., & White, J. C. (2009). A new data fusion model for high spatial- and temporal-resolution mapping of forest disturbance based on Landsat and MODIS. *Remote Sensing of Environment*, 113(8), 1613-1627. doi:<https://doi.org/10.1016/j.rse.2009.03.007>
- Hill, M. J., Smith, A. M., & Foster, T. C. (2000). Remote Sensing of Grassland with RADARSAT; Case Studies from Australia and Canada. *Canadian Journal of Remote Sensing*, 26(4), 285-296. doi:<https://doi.org/10.1080/07038992.2000.10874779>
- Hill, M. J., Ticehurst, C. J., Lee, J. S., Grunes, M. R., Donald, G. E., & Henry, D. (2005). Integration of optical and radar classifications for mapping pasture type in western Australia. *Ieee Transactions on Geoscience and Remote Sensing*, 43(7), 1665-1681. doi:<https://doi.org/10.1109/Tgrs.2005.846868>
- Hirschmugl, M., Deutscher, J., Gutjahr, K. H., Sobe, C., & Schardt, M. (2017). Combined use of SAR and optical time series data for near real-time forest disturbance mapping. Paper presented at the 2017 9th International Workshop on the Analysis of Multitemporal Remote Sensing Images (MultiTemp).
- Huete, A. R. (1988). A Soil-Adjusted Vegetation Index (Savi). *Remote Sensing of Environment*, 25(3), 295-309. doi:[https://doi.org/10.1016/0034-4257\(88\)90106-X](https://doi.org/10.1016/0034-4257(88)90106-X)

- Hunt, E. R., & Rock, B. N. (1989). Detection of Changes in Leaf Water-Content Using Near-Infrared and Middle-Infrared Reflectances. *Remote Sensing of Environment*, 30(1), 43-54. doi:[https://doi.org/10.1016/0034-4257\(89\)90046-1](https://doi.org/10.1016/0034-4257(89)90046-1)
- Inglada, J., Vincent, A., Arias, M., & Marais-Sicre, C. (2016). Improved Early Crop Type Identification By Joint Use of High Temporal Resolution SAR And Optical Image Time Series. *Remote Sensing*, 8(5), 362.
- Inglada, J., Vincent, A., Arias, M., Tardy, B., Morin, D., & Rodes, I. (2017). Operational High Resolution Land Cover Map Production at the Country Scale Using Satellite Image Time Series. *Remote Sensing*, 9(1). doi:<https://doi.org/10.3390/rs9010095>
- Jenerowicz, A., & Siok, K. (2017). *Fusion of radar and optical data for mapping and monitoring of water bodies*. Paper presented at the SPIE Remote Sensing.
- Jia, K., Liang, S., Wei, X., Yao, Y., Su, Y., Jiang, B., & Wang, X. (2014). Land Cover Classification of Landsat Data with Phenological Features Extracted from Time Series MODIS NDVI Data. *Remote Sensing*, 6(11), 11518. doi:<https://doi.org/10.3390/rs6111518>
- Jieli, C., Manchun, L., Yongxue, L., Chenglei, S., & Wei, H. (2010, 18-20 June 2010). *Extract residential areas automatically by New Built-up Index*. Paper presented at the 2010 18th International Conference on Geoinformatics.
- Jordan, C. F. (1969). Derivation of Leaf-Area Index from Quality of Light on the Forest Floor. *Ecology*, 50(4), 663-666. doi:<https://doi.org/10.2307/1936256>
- Joshi, N., Baumann, M., Ehammer, A., Fensholt, R., Grogan, K., Hostert, P., Jepsen, M. R., Kuemmerle, T., Meyfroidt, P., Mitchard, E. T. A., Reiche, J., Ryan, C. M., & Waske, B. (2016). A Review of the Application of Optical and Radar Remote Sensing Data Fusion to Land Use Mapping and Monitoring. *Remote Sensing*, 8(1). doi:<https://doi.org/10.3390/rs8010070>
- Kaimaris, D., & Patias, P. (2016). Identification and Area Measurement of the Built-up Area with the Built-up Index (BUI). *International Journal of Advanced Remote Sensing and GIS*(1), 1844-1858%V 1845. doi:<https://doi.org/10.23953/cloud.ijarsg.64>
- Kalman, R. E. (1960). A New Approach to Linear Filtering and Prediction Problems. *Journal of Basic Engineering*, 82(1), 35-45. doi:<https://doi.org/10.1115/1.3662552>
- Kaufman, Y. J., & Tanre, D. (1992). Atmospherically resistant vegetation index (ARVI) for EOS-MODIS. *IEEE Transactions on Geoscience and Remote Sensing*, 30(2), 261-270. doi:<https://doi.org/10.1109/36.134076>
- Kawamura, M., Jayamana, S., & Tsujiko, Y. (1996). Relation between Social and Environmental Conditions in Colombo Sri Lanka and the Urban Index Estimated by Satellite Remote Sensing Data. *International Archives of Photogrammetry Remote Sensing*, XXXI, Part B7, Vienna, 321-326.
- Kempeneers, P., Sedano, F., Piccard, I., & Eerens, H. (2016). Data Assimilation of PROBA-V 100 and 300 m. *IEEE Journal of Selected Topics in Applied Earth Observations and Remote Sensing*, 9(7), 3314-3325. doi:<https://doi.org/10.1109/JSTARS.2016.2527922>
- Korosov, A., Moiseev, A., Shuchman, R., & Podzdyakov, D. (2017). MODIS-AQUA and S-2 data fusion: application to optically shallow waters of lake Michigan. *Transactions of Karelian Research Center of Russian Academy of Sciences*. doi:<https://doi.org/10.17076/lim692>
- Le Hegarat-Masclé, S., Quesney, A., Vidal-Madjar, D., Taconet, O., Normand, M., & Loumagne, C. (2000). Land cover discrimination from multitemporal ERS images and multispectral Landsat images: A study case in an agricultural area in France. *International Journal of Remote Sensing*, 21(3), 435-456. doi:<https://doi.org/10.1080/014311600210678>
- Lefebvre, A., Beaugendre, N., Pennec, A., Sannier, C., & Corpetti, T. (2013). *Using data fusion to update built-up areas of the 2012 European High-Resolution Layer Imperviousness*. Paper presented at the 33rd EARSeL Symposium Conference - Towards Horizon 2020: Earth Observation and Social Perspectives, Matera, Italy.
- Lehmann, E. A., Caccetta, P., Lowell, K., Mitchell, A., Zhou, Z. S., Held, A., Milne, T., & Tapley, I. (2015). SAR and optical remote sensing: Assessment of complementarity and interoperability in the context of a large-scale operational forest monitoring system. *Remote Sensing of Environment*, 156, 335-348. doi:<https://doi.org/10.1016/j.rse.2014.09.034>

- Liu, H., & Huete, A. (1995). A feedback based modification of the NDVI to minimize canopy background and atmospheric noise. *Ieee Transactions on Geoscience and Remote Sensing*, 33(2), 457-465. doi:<https://doi.org/10.1109/36.377946>
- Lu, D. S., Mausel, P., Brondizio, E., & Moran, E. (2004). Relationships between forest stand parameters and Landsat TM spectral responses in the Brazilian Amazon Basin. *Forest Ecology and Management*, 198(1-3), 149-167. doi:<https://doi.org/10.1016/j.foreco.2004.03.048>
- Mallat, S. G. (1989). Multiresolution Approximations and Wavelet Orthonormal Bases of L2(R). *Transactions of the American Mathematical Society*, 315(1), 69-87. doi:<https://doi.org/10.2307/2001373>
- Marconcini, M., Üreyen, S., Esch, T., Metz, A., & Zeidler, J. (2017). *Mapping urban areas globally by jointly exploiting optical and radar imagery - the GUF+ 2015 layer*. Paper presented at the WorldCover 2017, ESA-ESRIN, Frascati (Rome), Italy.
- Mathieu, R., Pouget, M., Cervelle, B., & Escadafal, R. (1998). Relationships between satellite-based radiometric indices simulated using laboratory reflectance data and typic soil color of an arid environment. *Remote Sensing of Environment*, 66(1), 17-28. doi:[https://doi.org/10.1016/S0034-4257\(98\)00030-3](https://doi.org/10.1016/S0034-4257(98)00030-3)
- McNairn, H., Champagne, C., Shang, J., Holmstrom, D., & Reichert, G. (2009). Integration of optical and Synthetic Aperture Radar (SAR) imagery for delivering operational annual crop inventories. *Isprs Journal of Photogrammetry and Remote Sensing*, 64(5), 434-449. doi:<https://doi.org/10.1016/j.isprsjprs.2008.07.006>
- Meyer, Y. (1990). *Wavelets and operators*: Cambridge University Press.
- Michelson, D. B., Liljeberg, B. M., & Pilesjö, P. (2000). Comparison of algorithms for classifying Swedish landcover using Landsat TM and ERS-1 SAR data. *Remote Sensing of Environment*, 71(1), 1-15. doi:[https://doi.org/10.1016/S0034-4257\(99\)00024-3](https://doi.org/10.1016/S0034-4257(99)00024-3)
- Molina, D. E., & Datcu, M. (2016). Data mining tools for Sentinel 1 and Sentinel 2 data exploitation. *Image and Signal Processing for Remote Sensing Xxii*, 10004. doi:<https://doi.org/10.1117/12.2241542>
- Morishita, Y., & Hanssen, R. F. (2015). Temporal Decorrelation in L-, C-, and X-band Satellite Radar Interferometry for Pasture on Drained Peat Soils. *Ieee Transactions on Geoscience and Remote Sensing*, 53(2), 1096-1104. doi:<https://doi.org/10.1109/TGRS.2014.2333814>
- Morlet, J., Arens, G., Fourgeau, E., & Giard, D. (1982a). Wave-Propagation and Sampling Theory .1. Complex Signal and Scattering in Multilayered Media. *Geophysics*, 47(2), 203-221. doi:Doi 10.1190/1.1441328
- Morlet, J., Arens, G., Fourgeau, E., & Giard, D. (1982b). Wave-Propagation and Sampling Theory .2. Sampling Theory and Complex Waves. *Geophysics*, 47(2), 222-236. doi:Doi 10.1190/1.1441329
- Navarro, A., Rolim, J., Miguel, I., Catalao, J., Silva, J., Painho, M., & Vekerdy, Z. (2016). Crop Monitoring Based on SPOT-5 Take-5 and S-1A Data for the Estimation of Crop Water Requirements. *Remote Sensing*, 8(6). doi:<https://doi.org/10.3390/rs8060525>
- Notarnicola, C., Asam, S., Jacob, A., Marin, C., Rossi, M., & Stendardi, L. (2017). *Mountain crop monitoring with multitemporal S-1 and S-2 imagery*. Paper presented at the 2017 9th International Workshop on the Analysis of Multitemporal Remote Sensing Images (MultiTemp).
- Pesaresi, M., Gerhardinger, A., & Kayitakire, F. (2008). A Robust Built-Up Area Presence Index by Anisotropic Rotation-Invariant Textural Measure. *IEEE Journal of Selected Topics in Applied Earth Observations and Remote Sensing*, 1(3), 180-192. doi:<https://doi.org/10.1109/Jstars.2008.2002869>
- Petitjean, F., Inglada, J., & Gancarski, P. (2012). Satellite Image Time Series Analysis Under Time Warping. *Ieee Transactions on Geoscience and Remote Sensing*, 50(8), 3081-3095. doi:<https://doi.org/10.1109/TGRS.2011.2179050>
- Pinty, B., & Verstraete, M. M. (1992). GEMI: a non-linear index to monitor global vegetation from satellites. *Vegetatio*, 101(1), 15-20. doi:<https://doi.org/10.1007/bf00031911>

- Poggio, L., & Gimona, A. (2017). Assimilation of optical and radar remote sensing data in 3D mapping of soil properties over large areas. *Sci Total Environ*, 579, 1094-1110. doi:<https://doi.org/10.1016/j.scitotenv.2016.11.078>
- Pohl, C., & Van Genderen, J. L. (1998). Review article Multisensor image fusion in remote sensing: Concepts, methods and applications. *International Journal of Remote Sensing*, 19(5), 823-854. doi:<https://doi.org/10.1080/014311698215748>
- Pohl, C., & Van Genderen, J. L. (2015). Structuring contemporary remote sensing image fusion. *International Journal of Image and Data Fusion*, 6(1), 3-21. doi:<https://doi.org/10.1080/19479832.2014.998727>
- Price, K. P., Guo, X., & Stiles, J. M. (2002). Comparison of Landsat TM and ERS-2 SAR data for discriminating among grassland types and treatments in eastern Kansas. *Computers and Electronics in Agriculture*, 37(1), 157-171. doi:[https://doi.org/10.1016/S0168-1699\(02\)00110-2](https://doi.org/10.1016/S0168-1699(02)00110-2)
- Prince, S. D., & Goward, S. N. (1995). Global primary production: A remote sensing approach. *Journal of Biogeography*, 22(4-5), 815-835. doi:<https://doi.org/10.2307/2845983>
- Qi, J., Chehbouni, A., Huete, A. R., Kerr, Y. H., & Sorooshian, S. (1994). A modified soil adjusted vegetation index. *Remote Sensing of Environment*, 48(2), 119-126. doi:[https://doi.org/10.1016/0034-4257\(94\)90134-1](https://doi.org/10.1016/0034-4257(94)90134-1)
- Ray, T. W. (1994). A FAQ on Vegetation in Remote Sensing.
- Reiche, J., Verbesselt, J., Hoekman, D., & Herold, M. (2015). Fusing Landsat and SAR time series to detect deforestation in the tropics. *Remote Sensing of Environment*, 156, 276-293. doi:<https://doi.org/10.1016/j.rse.2014.10.001>
- Richardson, A. J., & Wiegand, C. L. (1977). Distinguishing Vegetation from Soil Background Information. *Photogrammetric Engineering and Remote Sensing*, 43(12), 1541-1552.
- Rouse Jr., J. W., Haas, R. H., Schell, J. A., & Deering, D. W. (1974). *Monitoring vegetation systems in the great plains with ERTS*. Paper presented at the 3d Earth Resources Technology Satellite-1 Symposium.
- Schmitt, A., Wendleder, A., & Hinz, S. (2015). The Kennaugh element framework for multi-scale, multi-polarized, multi-temporal and multi-frequency SAR image preparation. *Isprs Journal of Photogrammetry and Remote Sensing*, 102, 122-139. doi:<https://doi.org/10.1016/j.isprsjprs.2015.01.007>
- Schmitt, M., & Zhu, X. X. (2016). Data Fusion and Remote Sensing: An ever-growing relationship. *IEEE Geoscience and Remote Sensing Magazine*, 4(4), 6-23. doi:<https://doi.org/10.1109/MGRS.2016.2561021>
- Schmullius, C., Thiel, C., Pathe, C., & Santoro, M. (2015). Radar Time Series for Land Cover and Forest Mapping. In C. Kuenzer, S. Dech, & W. Wagner (Eds.), *Remote Sensing Time Series: Revealing Land Surface Dynamics* (pp. 323-356). Cham: Springer International Publishing.
- Schuster, C., Schmidt, T., Conrad, C., Kleinschmit, B., & Forster, M. (2015). Grassland habitat mapping by intra-annual time series analysis - Comparison of RapidEye and TerraSAR-X satellite data. *International Journal of Applied Earth Observation and Geoinformation*, 34, 25-34. doi:<https://doi.org/10.1016/j.jag.2014.06.004>
- Sedano, F., Kempeneers, P., & Hurtt, G. (2014). A Kalman Filter-Based Method to Generate Continuous Time Series of Medium-Resolution NDVI Images. *Remote Sensing*, 6(12), 12381-12408. doi:<https://doi.org/10.3390/rs61212381>
- Sinha, P., Kiran Verma, N., & Ayele, E. (2016). *Urban Built-up Area Extraction and Change Detection of Adama Municipal Area using Time-Series Landsat Images*.
- Smith, A. M., & Buckley, J. R. (2011). Investigating RADARSAT-2 as a tool for monitoring grassland in western Canada. *Canadian Journal of Remote Sensing*, 37(1), 93-102. doi:<https://doi.org/10.5589/m11-027>
- Smith, A. M., Major, D. J., McNeil, R. L., Willms, W. D., Brisco, B., & Brown, R. J. (1995). Complementarity of radar and visible-infrared sensors in assessing rangeland condition. *Remote Sensing of Environment*, 52(3), 173-180. doi:[https://doi.org/10.1016/0034-4257\(95\)00033-W](https://doi.org/10.1016/0034-4257(95)00033-W)

- Stefanski, J., Kuemmerle, T., Chaskovskyy, O., Griffiths, P., Havryluk, V., Knorn, J., Korol, N., Sieber, A., & Waske, B. (2014). Mapping Land Management Regimes in Western Ukraine Using Optical and SAR Data. *Remote Sensing*, 6(6), 5279-5305. doi:<https://doi.org/10.3390/rs6065279>
- Svoray, T., & Shoshany, M. (2003). Herbaceous biomass retrieval in habitats of complex composition: A model merging SAR images with unmixed landsat TM data. *Ieee Transactions on Geoscience and Remote Sensing*, 41(7), 1592-1601. doi:<https://doi.org/10.1109/Tgrs.2003.813351>
- Swain, P. H., Robertson, T. V., & Wacker, A. G. (1971). Comparison of the Divergence and B-Distance in Feature Selection. *LARS Information Note 020871*.
- Sylla, D., Minghelli-Roman, A., Blanc, P., Mangin, A., & d'Andon, O. H. F. (2014). Fusion of Multispectral Images by Extension of the Pan-Sharpener ARSIS Method. *IEEE Journal of Selected Topics in Applied Earth Observations and Remote Sensing*, 7(5), 1781-1791. doi:10.1109/JSTARS.2013.2271911
- Taha, L. G. E.-d., & Elbeih, S. F. (2010). Investigation of fusion of SAR and Landsat data for shoreline super resolution mapping: the northeastern Mediterranean Sea coast in Egypt. *Applied Geomatics*, 2(4), 177-186. doi:<https://doi.org/10.1007/s12518-010-0033-x>
- Talab-Ou-Ali, H., Niculescu, S., Sellin, V., & Bougault, C. (2017). *Contribution of the new satellites (S-1, S-2 and SPOT-6) to the coastal vegetation monitoring in the Pays de Brest (France)*. Paper presented at the SPIE Remote Sensing.
- Tucker, C. J. (1979). Red and Photographic Infrared Linear Combinations for Monitoring Vegetation. *Remote Sensing of Environment*, 8(2), 127-150. doi:[https://doi.org/10.1016/0034-4257\(79\)90013-0](https://doi.org/10.1016/0034-4257(79)90013-0)
- Turner, D. P., Cohen, W. B., Kennedy, R. E., Fassnacht, K. S., & Briggs, J. M. (1999). Relationships between leaf area index and Landsat TM spectral vegetation indices across three temperate zone sites. *Remote Sensing of Environment*, 70(1), 52-68. doi:Doi 10.1016/S0034-4257(99)00057-7
- Vaglio Laurin, G., Liesenberg, V., Chen, Q., Guerriero, L., Del Frate, F., Bartolini, A., Coomes, D., Wilebore, B., Lindsell, J., & Valentini, R. (2013). Optical and SAR sensor synergies for forest and land cover mapping in a tropical site in West Africa. *International Journal of Applied Earth Observation and Geoinformation*, 21, 7-16. doi:<https://doi.org/10.1016/j.jag.2012.08.002>
- Veloso, A., Mermoz, S., Bouvet, A., Le Toan, T., Planells, M., Dejoux, J.-F., & Ceschia, E. (2017). Understanding the temporal behavior of crops using S-1 and S-2-like data for agricultural applications. *Remote Sensing of Environment*, 199, 415-426. doi:<https://doi.org/10.1016/j.rse.2017.07.015>
- Villa, P., Stroppiana, D., Fontanelli, G., Azar, R., & Brivio, P. (2015). In-Season Mapping of Crop Type with Optical and X-Band SAR Data: A Classification Tree Approach Using Synoptic Seasonal Features. *Remote Sensing*, 7(10), 12859. doi:<https://doi.org/10.3390/rs71012859>
- Wang, Q., Adiku, S., Tenhunen, J., & Granier, A. (2005). On the relationship of NDVI with leaf area index in a deciduous forest site. *Remote Sensing of Environment*, 94(2), 244-255. doi:10.1016/j.rse.2004.10.006
- Wang, Q. M., Blackburn, G. A., Onojeghuo, A. O., Dash, J., Zhou, L. Q., Zhang, Y. H., & Atkinson, P. M. (2017). Fusion of Landsat 8 OLI and S-2 MSI Data. *Ieee Transactions on Geoscience and Remote Sensing*, 55(7), 3885-3899. doi:<https://doi.org/10.1109/Tgrs.2017.2683444>
- Waske, B., & Benediktsson, J. A. (2007). Fusion of Support Vector Machines for Classification of Multisensor Data. *Ieee Transactions on Geoscience and Remote Sensing*, 45(12), 3858-3866. doi:<https://doi.org/10.1109/TGRS.2007.898446>
- Waske, B., & van der Linden, S. (2008). Classifying Multilevel Imagery From SAR and Optical Sensors by Decision Fusion. *Ieee Transactions on Geoscience and Remote Sensing*, 46(5), 1457-1466. doi:<https://doi.org/10.1109/TGRS.2008.916089>
- Wei, M., & Sandwell, D. T. (2010). Decorrelation of L-Band and C-Band Interferometry Over Vegetated Areas in California. *Ieee Transactions on Geoscience and Remote Sensing*, 48(7), 2942-2952. doi:<https://doi.org/10.1109/TGRS.2010.2043442>
- Woodhouse, I. H. (2006). *Introduction to Microwave Remote Sensing*: CRC Press, Boca Raton, FL.

- Xu, H. (2006). Modification of normalised difference water index (NDWI) to enhance open water features in remotely sensed imagery. *International Journal of Remote Sensing*, 27(14), 3025-3033. doi:<https://doi.org/10.1080/01431160600589179>
- Xu, H. (2008). A new index for delineating built-up land features in satellite imagery. *International Journal of Remote Sensing*, 29(14), 4269-4276. doi:<https://doi.org/10.1080/01431160802039957>
- Xue, J., Leung, Y., & Fung, T. (2017). A Bayesian Data Fusion Approach to Spatio-Temporal Fusion of Remotely Sensed Images. *Remote Sensing*, 9(12). doi:<https://doi.org/10.3390/rs9121310>
- Yesou, H., Pottier, E., Mercier, G., Grizonnet, M., Haouet, S., Giros, A., Faivre, R., Huber, C., & Michel, J. (2016, 10-15 July 2016). *Synergy of S-1 and S-2 imagery for wetland monitoring information extraction from continuous flow of sentinel images applied to water bodies and vegetation mapping and monitoring*. Paper presented at the 2016 IEEE International Geoscience and Remote Sensing Symposium (IGARSS).
- Zha, Y., Gao, J., & Ni, S. (2003). Use of normalized difference built-up index in automatically mapping urban areas from TM imagery. *International Journal of Remote Sensing*, 24(3), 583-594. doi:<https://doi.org/10.1080/01431160304987>
- Zhang, J. (2010). Multi-source remote sensing data fusion: status and trends. *International Journal of Image and Data Fusion*, 1(1), 5-24. doi:<https://doi.org/10.1080/19479830903561035>
- Zheng, Y., Zhang, M., Zhang, X., Zeng, H. W., & Wu, B. F. (2016). Mapping Winter Wheat Biomass and Yield Using Time Series Data Blended from PROBA-V 100-and 300-m S1 Products. *Remote Sensing*, 8(10). doi:<https://doi.org/10.3390/rs8100824>
- Zhou, Y., Yang, G., Wang, S. X., Wang, L. T., Wang, F. T., & Liu, X. F. (2014). A new index for mapping built-up and bare land areas from Landsat-8 OLI data. *Remote Sensing Letters*, 5(10), 862-871. doi:<https://doi.org/10.1080/2150704x.2014.973996>
- Zhu, X., Chen, J., Gao, F., Chen, X., & Masek, J. G. (2010). An enhanced spatial and temporal adaptive reflectance fusion model for complex heterogeneous regions. *Remote Sensing of Environment*, 114(11), 2610-2623. doi:<https://doi.org/10.1016/j.rse.2010.05.032>
- Zhu, Z., Wang, S., & Woodcock, C. E. (2015). Improvement and expansion of the Fmask algorithm: cloud, cloud shadow, and snow detection for Landsats 4–7, 8, and Sentinel 2 images. *Remote Sensing of Environment*, 159, 269-277. doi:<https://doi.org/10.1016/j.rse.2014.12.014>